VNIVERSITAT DE VALÈNCIA

Doctorado en Nanociencia y Nanotecnología

PhD tesis:

Charge transport and recombination layers for perovskite solar cells

PhD candidate:

Jorge Pablo Ávila Gómez

Supervisors:

Dr. Hendrik Jan Bolink

Dr. Michele Sessolo

Tutor:

Dr. Hendrik Jan Bolink

JUNIO 2020

Dr. Hendrik Jan Bolink y **Dr. Michele Sessolo**, Investigador de la Universidad de Valencia en el Instituto de Ciencia Molecular (ICMol) e Investigador Postdoctoral del Instituto de Ciencia Molecular, respectivamente, certifican que la memoria presentada por el doctorando Jorge Pablo Ávila Gómez con el título “Charge transport and recombination layers for perovskite solar cells” corresponde a su Tesis Doctoral y ha sido realizada bajo su dirección, autorizando mediante este escrito la presentación de la misma.

En Valencia, a 5 de junio del 2020

Dr. Hendrik Jan Bolink	Dr. Michele Sessolo
(director y tutor)	(director)

Acknowledgments

I want to start expressing my deep gratitude to my supervisors, Henk Bolink and Michele Sessolo. For all the teaching and knowledge, support and advising that they have shared with me during all these years, it is priceless. Henk Bolink, I have always admired his assertiveness, both professionally and personally, managing this amazing group. I really appreciate the opportunity of had been part of the group. Y Michele Sessolo, a quien admiro como fuente de sabiduría e inspiración, quien me ha enseñado a valorar el sudor y a disfrutar de las cosas bien hechas.

Igualmente extiendo mis agradecimientos a todos los compañeros del instituto y del grupo de investigación. Thanks to all the people that were around in the early days and already left the group, Enrico, Toni, M. Cristina, Giulia, Benni, Vaheed, Wiria, and of course those who joined our group for some time. And especially David, who was a great coworker and friend during the first years. My mind overflows of great memories that I am sure will never this a pear! Un caluroso reconocimiento a Ángel, por el montón de buenos ratos juntos y las variadas e interesantes conversaciones que hemos tenido. Por ayudarme tanto en el lab como en la vida. Ante situaciones difíciles siempre me gusta preguntarme cómo lo solucionaría Ángel. Eres un crack. Dani, con quien ha sido un placer trabajar y sentir su apoyo en los vaivenes de la investigación. Ha sido y es un amigo brillante con quien he compartido buenos ratos no solo en fiestas sino también en excursiones, astronomía y buenas viciadas. Lidón porque es una pedazo de máquina, ayudando en el laboratorio y como la enciclopedia Larousse del grupo. Gracias por todo lo que me has enseñado y los buenos ratos dentro de la pecera y fuera de ella. Laura, a quien conozco desde mis primeros días en Valencia, y con quien he compartido Máster, Doctorado y un montón de buenos momentos. Gracias por tu positividad y buen rollo, siempre te recordaré como la terrateniente de la felicidad. Maria Grazia, que ha sido compañera de despacho, de conciertos y aventuras; sabes que te aprecio un montón a pesar de nuestros rifirrafes. Y a Azin, no puedo más que recordarle que el destino le aguarda con toneladas de chocolate. Se paciente, eres una persona virtuosa, lo conseguirás.

A Paco y Pablo, por aportar siempre su grano de genialidad, conversar con ellos siempre es oro. Extiendo mis agradecimientos a Jorge F., María, Paula, Alejandra, Paco E., Cristian por todo su trabajo esencial y ser capaces de batallar los mil y un molinos contra los que me desollaba continuamente. And thanks to all the newcomers (and no so new): Aroa, Ana, Chris, Kassio (my recent flatmate and amazing interior designer :D), Isidora, Paz, Yous, Lorenzo, Bas, Sang, Vicente, Beom, Xavi, Cihan, Miguel, Abhi, Nathan… They are great and make the working environment a pleasant experience.

No puedo olvidarme de la gente del máster y del instituto, Ramón, Javi C, Mario, Miguel, Jesús, Laura, Néstor, Eugenia, Samuel, Cristián, y demás cracks, sin olvidarme de mencionar a Javi L, compañero de piso y vicisitudes propias de la vida y el doctorado. Gracias por vuestra amistad, compañerismo, cafés interminables, risas, fiestas y veladas.

Mucho es lo que adeudo a Jairo, como mi mejor amigo y un hermano desde hace muchísimos años (bastantes más de diez según la postal de Padrelimón de la catedral de Gloucester). Alguien a quien he tenido siempre ahí, férreo y magnánimo, como una constante, es una persona generosa y un apoyo inmensurable. Sobrevolando Granada, redirijo un especial agradecimiento a “los dezertisados” que han leído y comentado el resumen en castellano. Y a todos ellos, porque han mantenido viva la llama de la amistad, a pesar de la distancia entre muchos de nosotros. Sentir su apoyo generoso y desprendido me ha dado fuerza y energía durante todos estos años.

Y por supuesto, a mi familia, por su apoyo y confianza en la distancia, y por cada beso y abrazo en los reencuentros. Debo a mis padres más que a nadie. Han sido pilares en los cuales he podido apoyarme en todo momento. Ellos me han cuidado y llenado de fuerza, cariño y alegría, y junto a mis hermanas, forman un hogar feliz y seguro, donde he podido encontrar la paz cuando más la he necesitado. Porque si he llegado a ser quien soy ha sido sin duda gracias a vosotros, así que os dedico con especial emoción este trabajo.

Contents

Chapter 1

Introduction

"Here there seemed to be a case of light actually producing an electromotive force."

– W. Adams and R. Day, 1876, the first report of the photovoltaic effect.[1]

A New Energy Paradigm

Modern society activities from agriculture, industry to services depend vastly on the energy supply. Since the Industrial Revolution, energy has become a crucial resource: a stable and continuous energy supply has allowed an unstoppable economic and industrial growth. Nevertheless, progress has only catapulted the energy consumption, so that today we face a society hungry for energy at an unstoppable pace with around 80% of the generated energy still coming from oil and coal. These fossil fuels, as abundant energy sources, involve several concerns about the future of energy. First, as non-renewable materials, fossil fuels are finite resources on Earth, and reserves will be depleted in the next decades at the current consumption rate.[2] Second, the large fuel consumption results in a large quantity of waste, in particular fine particles and gases, which cannot be assimilated by our ecosystem. The combustion of coal and hydrocarbons produces carbon dioxide, which is the main greenhouse gas that contributes to global warming. The expected rise of temperature by 2100 is on course for 3 to 5 °C, far from the global target of limiting the increase to 2 °C. The greatest challenge of our time is to change the energy paradigm toward renewable energy sources. One of the emerging renewable sources with enormous potential is solar energy. Solar power is virtually unlimited, and technologies to harvest it are being rapidly developed, making it one of the most important candidates to power human societies.

Among the different technologies to harvest sunlight, photovoltaics (PV) is one of the most promising due to its ability to directly converts photons into electrons. Solar cells can be roughly classified into three generations. The first-generation cells are made of crystalline and polycrystalline silicon. These technologies dominate the PV market with more than 80% of the global market share in terms of annual production.[3] The second generation of solar cells is characterized by the use of direct bandgap semiconductors such as amorphous silicon, CdTe and ClGS. These semiconductors are orders of magnitude more efficient harvesting sunlight than crystalline silicon. In consequence, these devices consist of thin layers, decreasing the material consumption, cost and weight and potentially leading to cheaper energy production. Despite the improved optical properties their presence in the global market still remains below 10%.

These two generations both require high temperature and complex fabrication processes.

An alternative, new generation of solar cells is being developed. It includes semiconductors that can be produced by simple solution or vacuum methods at moderate temperatures, promising to overcome the limitations of previous technologies and to achieve the goal of producing inexpensive and high efficiency solar cells. This third generation of solar cells, also known as emerging photovoltaics, comprised several thin film technologies still in the research or development phase. Emerging photovoltaics include CZTS solar cells, dye-sensitized solar cells, organic solar cells, quantum dot solar cells and perovskite solar cells. Among the different technologies, perovskite solar cells have received tremendous attention in academic and industrial fields as their efficiencies at the lab scale have recently reached 25% in a relatively short time. They have exceeded all other new generation and thin-film technologies, including CdTe and CIGS (except for GaAs), with efficiency only 1.5% below the silicon heterojunction cells.[4] Due to the low energetic, inexpensive and easy processing, together with their excellent optoelectronic properties, perovskite solar cells have the potential to transform the energy paradigm as we know it today.

Perovskite solar cells

A perovskite is any kind of compound sharing the crystal structure of calcium titanate ($CaTiO_3$), which can be simplified with the formula ABX_3, where A and B are cations and X is an anion (a halide in metal halide perovskites). The extended perovskite structure is composed of the cation B in octahedral coordination with the halide X in the vertexes (BX_6). The metal halide octahedra are arranged sharing the vertexes in an extended 3D structure. The cations A are located in the interstitial hole between eight octahedra. The crystal structure of a cubic perovskite is depicted in **Fig. 1**. The formation of a stable perovskite strongly depends on the ionic radii of the components. This constraint has been widely studied and led to the preparation of a wide variety of photoactive perovskite materials.[5–7] In perovskite semiconductors for solar cells, the larger cation A is usually an organic molecules, generally methylammonium ($CH_3NH_3^+$) or formamidinium ($NH_2CH{=}NH_2^+$), or the inorganic cation cesium (Cs^+). The anion X is a halide, generally iodine, although Br and Cl are also commonly used, usually in mixed halide compounds. Cation B has conventionally been Pb^{2+} as it leads to the best materials used in efficient solar cells. Sn^{2+} has been also used as B cation, although its tendency to oxidation introduces intrinsic instability in the perovskite. Nevertheless, mixed Sb-Pb perovskites have lately shown excellent performance and stability.[8]

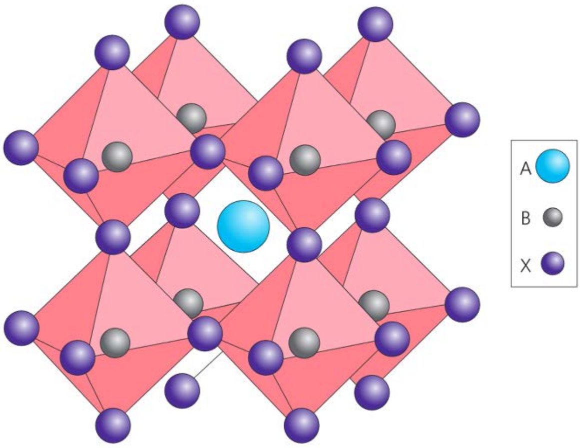

Fig. 1 Crystal structure of a cubic perovskite. In lead halide perovskites, the A cation is generally methylammonium ($CH_3NH_3^+$), formamidinium ($NH_2CH{=}NH_2^+$) or cesium (Cs^+). The anion X is a halide, while the most common B cations are Pb^{2+} or Sn^{2+}. Reproduction from ref. 9.

The material combinations determine both the optical and electronic properties (bandgap, mobility, diffusion lengths, etc.) of the final perovskite. The archetypal compound is methylammonium lead triiodide ($CH_3NH_3PbI_3$, commonly named MAPI), which exhibits unique electrical and optical properties.[10–14] The optical absorption coefficient ($\alpha > 10^5$ cm^{-1}) of $CH_3NH_3PbI_3$ is comparable to other direct bandgap inorganic semiconductors, as GaAs or CdTe.[15] The large absorption coefficient allows to efficiently harvest incident photons while keeping the absorber layer thickness low. The excitons produced by light absorption have a very weak binding energy, in the order of tens of meV, which is comparable to the thermal energy (kT) at room temperature.[16–18] That means that most of the optically generated charges are present in the form of free carriers. High carrier mobilities have been measured for electrons and holes, in the tens of $cm^2V^{-1}s^{-1}$,[19,20] which are much higher than typical mobilities of organic materials (10^{-4} - 1 $cm^2V^{-1}s^{-1}$).[21] All these properties result in very long carrier-diffusion lengths, which prevents free carriers to recombine once they have been separated. Compared to organic materials, $CH_3NH_3PbI_3$ has shown diffusion lengths in the µm range, depending on the synthetic method.[22–26] All these characteristics have converted perovskite in one of the most promising materials for next-generation photovoltaic technologies.

Vacuum deposition

The deposition method strongly influences the morphology of the perovskite film and hence its optoelectronic properties. The challenge is to control the morphology to produce highly uniform films that are pinhole-free and with high crystallinity. All processes of charge separation, transport and extraction strongly depend on the crystallinity of the film.[22] There are different methodologies to deposit the perovskite and the rest of the layers in perovskite solar cells, ranging from solution-based techniques such as spin coating and doctor blading to vacuum methods.

Vacuum deposition methods are widely used in the semiconductor industry on a large scale for optoelectronic applications. They are also increasingly applied in the preparation of perovskite films for optoelectronics.[27] Vacuum deposition methods offer several advantages in the deposition of perovskite thin films:

- **Inherent purity of sublimed materials.** The temperature control of the precursors during the evaporation allows to eliminate the impurities with different sublimation temperatures.
- **Control over the film thickness.** The layer thickness is monitored during the evaporation process using quartz crystal microbalances (QCMs). Nanometer precision can be reached which permits the fabrication of devices where the exact thickness is crucial.
- **Intrinsically additive.** In solution-based methods, the solvent used to process a film can dissolve the underlying layer. Hence, materials and solvents must be chosen accordingly. Evaporated layers do not require any solvents, facilitating the preparation of multilayer structures as tandem solar cells.

- **Dry processing.** The use of toxic solvents, generally employed for solution methods, is avoided. Moreover, the high boiling point solvents are hard to remove from the film.
- **Large area compatible.** Dimensions of the evaporated layers are only limited by the sublimation chamber size or geometry of the thermal source.
- **Wide substrates compatibility.** Compatible with temperature sensitive materials such as textile or plastic for lightweight flexible devices. It is compatible too with not flat surfaces as structured silicon for tandem applications.

The evaporation of perovskite films is carried out by the simultaneous thermal sublimation of the precursors, generally an organic salt (MAI) and the metal halide (PbI_2). Under stoichiometric conditions the precursors condense and react on a substrate placed above the thermal sources growing the $CH_3NH_3PbI_3$ film. As far back as 2013, the first example of this technique to prepare perovskite solar cells was reported, reaching an efficiency of 15%.[28] In that report, $PbCl_2$ and excess MAI were used as precursors, leading to a mixed perovskite ($CH_3NH_3PbI_{3-x}Cl_x$). Later in 2014, our group adapted the method to deposit pure iodide $CH_3NH_3PbI_3$ films.[29] Since these early works, the research towards sublimed perovskite devices has largely progressed, reaching efficiency of 20%.[30] Recently, several reports brought a better understanding of the processes that govern the vapor deposition of perovskites.[27,31–34] These findings might foster the development of vacuum processed devices to reach the state-of-the-art efficiency of solution-processed perovskite solar cells.

Device architectures

Perovskite solar cells can be divided into two major groups depending on the side through which the light enters first. When the light passes through the electron transport layer the architecture is denoted as **n-i-p**, in the opposite case the device is denoted as **p-i-n**. Generally, the light shines on the devices through the glass/TCO interface, hence this notation is strongly related to the fabrication sequence in which the layers are deposited (**Fig. 2**).

The **n-i-p** architecture is the most widely adopted for solution-processed perovskite solar cells. Originally, the first perovskite solar cells were prepared in this configuration using as ETL a dense TiO_2 film followed by a mesoporous TiO_2 layer. The perovskite is then infiltrated in the mesoporous structure. This configuration is derived from dye-sensitized solar cells, where the mesoporous scaffold enhances the photon absorption and charge collection, facilitating the electrons extraction and transport. It has been shown that perovskite solar cells can also operate in a planar configuration thanks to their ambipolar transport properties and the presence of free carriers.[23] Nevertheless, the highest efficiencies have been achieved using the mesoporous scaffold.[35] The common HTL used in n-i-p devices is 2,2′,7,7′-tetrakis(N,N-di-p-methoxyphenylamine)-9,9′-spirobifluorene (Spiro-OMeTAD), also adapted from dye-sensitized solar cells. Lately, alternative materials as poly(triarylamine) (PTAA) and Poly(3-hexylthiophene) (P3HT) have also been used in record efficiency devices.

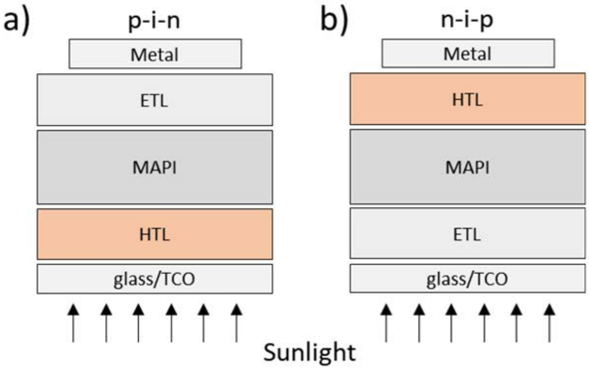

Fig. 2 Device architectures of perovskite solar cells. **a)** p-i-n, **b)** n-i-p structures.

Most **p-i-n** solar cells use a planar configuration, which resembles typical organic solar cells, hence benefiting from the knowledge in organic transport materials. The commonly used HTLs in the p-i-n structure are PEDOT:PSS, PTAA and NiOx, and ETLs are C_{60} and its derivatives.[36–40] This kind of structure is interesting as it usually avoids high thermal processes, being compatible with flexible and sensitive substrates. Also, it facilitates its implementation into perovskite/silicon tandems, as p-i-n is the dominant configuration in commercial silicon solar cells.

Our group has shown efficient fully evaporated **n-i-p** and **p-i-n** perovskite solar cells, using a planar configuration.[30] The devices present mirrored structures as the evaporation method allows for an arbitrary order of the deposition. The HTL used in the devices was (N4,N4,N4″,N4″-tetra([1,1′-biphenyl]-4-yl)-[1,1′:4′,1″-terphenyl]-4,4″-diamine) (TaTm) and the ETL C_{60}, with their respective dopants, 2,2′-(perfluoronaphthalene-2,6-diylidene)di-malononitrile (F_6-TCNNQ) as p-dopant and N1,N4-bis(tri-p-tolylphosphoranylidene)-benzene-1,4-diamine (PhIm) as n-dopant (**Fig. 3**). In this thesis we will follow the general structure of these fully evaporated devices, exploring alternative materials and architectures for efficient and stable perovskite solar cells.

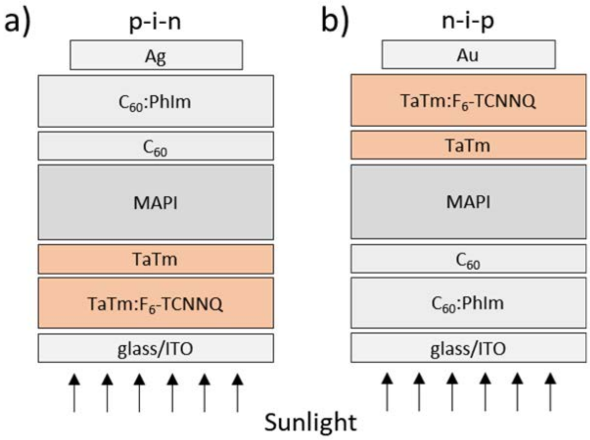

Fig. 3 Device architectures of fully evaporated perovskite solar cells. **a)** p-i-n, **b)** n-i-p structures.[30]

The maximum theoretical achievable efficiency of single junction solar cells is described by the Shockley–Queisser limit.[41] As efficiency of the solar cells approaches this boundary, several paths, as tandem solar cells, have been explored to overcome this limitation. A multijunction or tandem device consists of two or more sub-cells connected electrically. Each of them is able to absorb a different part of the electromagnetic spectrum, reducing thermalization losses and reaching higher efficiencies compared to single-junction cells. Tandems are classified as two- or four-terminal, depending on the number of electric contacts and their connection. The main difference is that in two-terminal devices, the sub-cells are monolithically stacked and electrically connected in series. These devices require a charge recombination layer or tunnel junction where the charge neutrality is achieved (**Fig. 4a**). On the other hand, in four-terminal devices the sub-cells can be mechanically stacked and are connected in parallel (**Fig. 4b**).

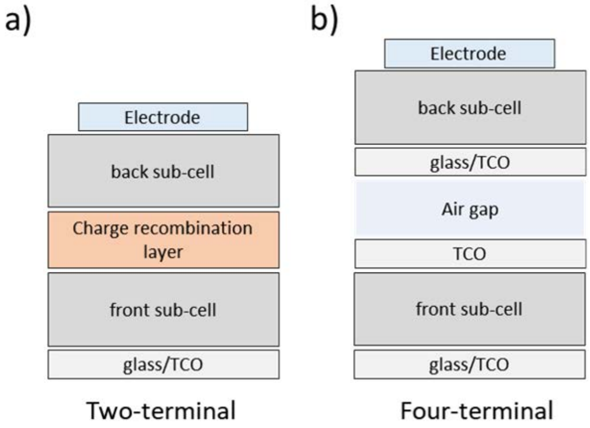

Fig. 4 Scheme of the most common multijunction configurations, **a)** two-terminal and **b)** four-terminal.

The simple film-processing and the tunable bandgap of perovskites make them an attractive candidate for tandem solar cells. The interest has been growing lately, with the demonstrations of several perovskite-based tandem devices. Perovskites have been combined with well-established technologies as silicon, copper indium gallium selenide (CIGS) or organic solar cells. Also, perovskite with different bandgap can be combined in tandem solar cells.[42] The state-of-the-art on perovskite tandems is discussed in **chapter 5**, where a fully vacuum deposited perovskite tandem solar cell is presented.

Theory of solar cell

The main element of a solar cell is the light-absorbing semiconductor (perovskite), the part that absorbs photons and converts them into charge carriers (electrons and holes). This conversion is possible thanks to the electronic band structure of semiconductors. The electronic energy levels in a semiconductor are generally divided into two bands: the valence band and the conduction band. The valence band contains the highest occupied electronic energy levels and is hence is responsible for the transport of holes (positive carriers). On the contrary, the conduction band contains the lowest unoccupied energy levels and is responsible for the transport of electrons (negative carriers). The energy difference between the valence band and the conduction band is known as the bandgap. If a photon entering the semiconductor has an energy equal or larger than the bandgap, it will be absorbed, exciting an electron from the valence band into the conduction band and leaving an unoccupied state in the valence band (a hole). Due to their opposite charge, the electron and hole can be coulombically bound in a state known as an exciton, which should be split into free carriers to generate an electrical current. The energy required to break the exciton (exciton binding energy) depends on the dielectric constant of the material. Importantly, perovskites present high dielectric constants, leading to low exciton binding energies.[18] This means that in perovskite solar cells, the thermal energy at room temperature is sufficient to form free electrons and holes immediately after illumination. These electrons and holes are selectively extracted by the hole and the electron transport materials and collected at the electrodes.

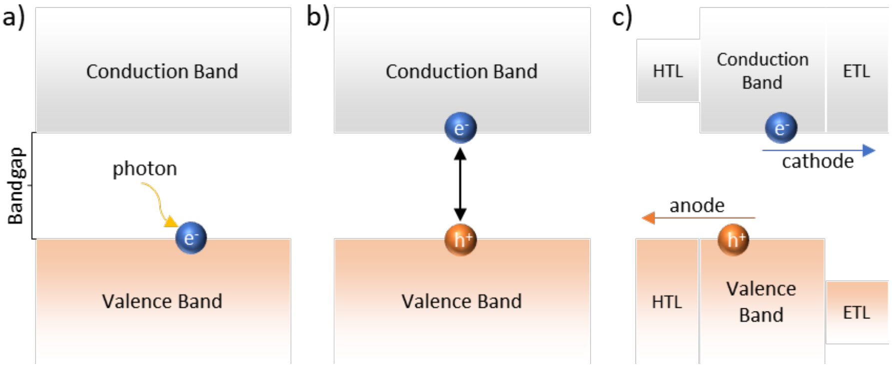

Fig. 5 Basic operation of a solar cell. **a)** Absorption of a photon by the semiconductor. **b)** Excitation of an electron to the conduction band, with a hole left in the valence band. **c)** Electron and hole are selectively transported to the electrodes.

The role of the transport materials is also very important for the device performance. In perovskite solar cells, the efficiency can be limited by recombination at the perovskite/transport layer interfaces and by resistive losses due to poor mobility of the transport materials. An efficient transport layer must fulfill several properties:

- **Energy level alignment with the perovskite.** Ensuring lossless transfer of one type of charge carrier while effectively blocking the opposite.[14,43]
- **High transparency.** To minimize the parasitic optical absorption.[44]
- **Good charge mobility.** To ensure a fast transport and minimize charge accumulation, preventing recombination of the carriers.[45]

The energy level alignment controls the charge injection/extractions at the perovskite/transport-layer junctions. Lowering the energy barrier at these interfaces is important to facilitate efficient charge injection/extraction avoiding recombination losses. There is a wide selection of transport materials with optimum HOMO and LUMO energy levels aligned with the perovskite bands. When these materials have also a wide bandgap, they usually accomplish two other properties, the blocking of the opposite carrier and high transparency. The main disadvantage is that in general, organic semiconductors have low charge mobility as transport is controlled by hopping. A common approach to improve the transport properties of an organic semiconductor is by doping. The dopant is capable of increasing the charge carrier density by partially reducing/oxidizing (n-/p-doping) the organic material. The conductivity can typically increase several orders of magnitude as a function of the dopant concentration, reducing the resistive losses.[46,47] In **chapters 2** and **3**, the doping of organic semiconductors will be studied on perovskite solar cells, together with alternative strategies to improve the charge extraction.

Aim of the thesis

The scope of this thesis is the study of vacuum deposited single junction and tandem perovskite solar cells and the optimization of charge transport layers, to maximize the efficiency and stability of the devices. To reach this target, methodologies to characterize the charge transport layers must be developed and the device stack needs to be optimized. The work has been structured in three sections:

- **Chapter 3**: The influence of doped charge transport layers on p–i–n perovskite solar cells.

- **Chapter 4**: Application of $(RuCp^{*}mes)_2$ as a sublimable n-dopant for n–i–p perovskite solar cells.

- **Chapter 5**: Fabrication of vacuum-deposited $CH_3NH_3PbI_3$ – $CH_3NH_3PbI_3$ tandem solar cells.

Chapter 2

Experimental and methodology

In the following chapter the preparation and characterization of the devices is introduced. A variety of device structures were prepared as n-i-p and p-i-n single junctions together with tandem perovskite solar cells. Thermal evaporation was the main technique used to prepare the devices and films.

Materials

Photolithographically patterned ITO coated glass substrates were purchased from Naranjo Substrates (www.naranjosubstrates.com). 2,2'-(Perfluoronaphthalene-2,6-diylidene) dimalononitrile (F_6-TCNNQ), *N*4,*N*4,*N*4'',*N*4''-tetra([1,1'-biphenyl]-4-yl)-[1,1':4',1''-terphenyl]-4,4''-diamine (TaTm) and N1,N4-bis(tri-ptolylphosphoranyli-dene) benzene-1,4-diamine (PhIm) were provided by Novaled GmbH. Fullerene (C_{60}) was purchased from Sigma Aldrich and 2,9-Dimethyl-4,7-diphenyl-1,10-phenanthroline (BCP) from Lumtec. PbI_2 was purchased from Tokyo Chemical Industry CO (TCI), and CH_3NH_3I (MAI) from Lumtec. The pentamethylcyclopentadienyl mesitylene ruthenium dimer $(RuCp^*mes)_2$ was synthesized by collaborators at Georgia Institute of Technology following previously published protocols.[48] TiO_2 nanoparticle suspensions in pure ethanol were provided by our collaborator Dr Hadipour from IMEC and deposited through a low temperature process, compatible with ITO substrates.[49,50]

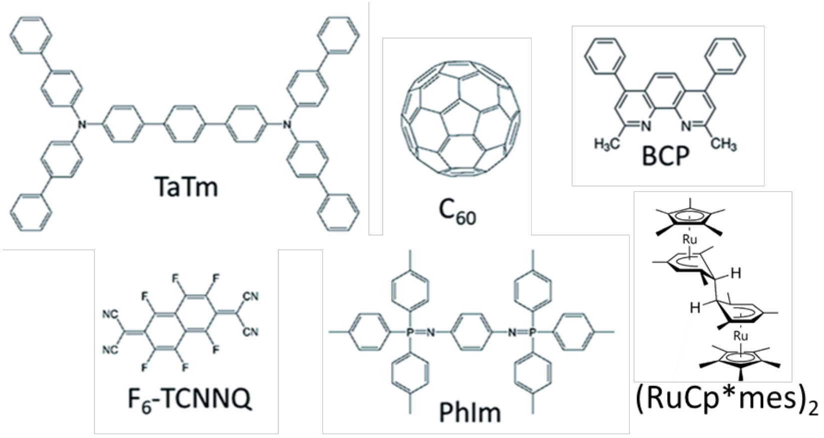

Fig. 6 Chemical structures of the organic semiconductors used as transport materials**.**

Fabrication of p-i-n perovskite solar cells

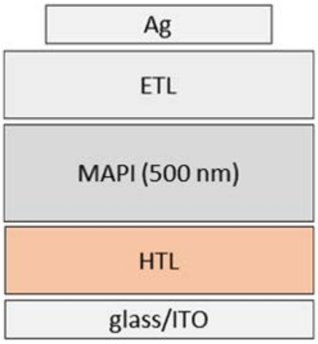

Fig. 7 p-i-n device structure.

The devices with a p-i-n structure used an architecture as follow: ITO/HTL/perovskite/ETL/Ag. The materials used to prepare the HTLs were F_6-TCNNQ and TaTm. The layers were prepared by thermal evaporation in high vacuum with a base pressure of $1 \cdot 10^{-6}$ mbar. Three different HTL structures were used in the devices, i) a doped layer approach consisting of 40 nm thick doped hole transport layer (TaTm:F_6-TCNNQ) capped with a 10 nm thick film of pure TaTm, ii) a 10 nm thick, pure TaTm film, or iii) a thin (2.5 nm) layer of pure F_6-TCNNQ deposited in between the ITO and a 10 nm thick TaTm film. Once completed the HTL deposition, the perovskite film was co-evaporated on top of the HTL, following the procedure described in the section **Methylammonium lead iodide film deposition**. The materials used in the ETL were PhIm, C_{60} and BCP. The electron transport layers were prepared by thermal evaporation and two different variations were used: i) a doped layer approach formed by a film of pure C_{60} (10 nm) capped with a 40 nm thick, doped electron transport layer (C_{60}:PhIm), or ii) a film of pure C_{60} (25 nm) followed by a thin layer (8 nm) of BCP. These materials were (co-)sublimed at temperatures ranging from 135-160 °C for the dopants to 250 °C for the pure charge transport molecules. In doped films, the deposition rate for TaTm and C_{60} was kept constant at 0.8 Å s^{-1} while varying the deposition rate of the dopants during co-deposition (depending on the desired doping concentration). Pure TaTm, F_6-TCNNQ, BCP and C_{60} layers were deposited at a rate of 0.5 Å s^{-1}. Afterwards the metal top contact (Ag, 100 nm thick) was deposited.

Fabrication of n-i-p perovskite solar cells

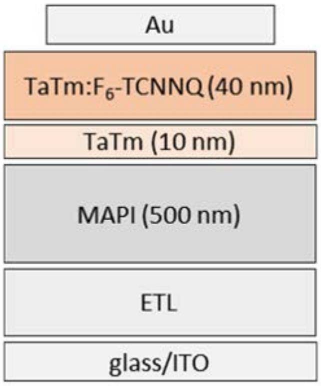

Fig. 8 n-i-p device structure.

The devices with a n-i-p structure used the following architecture: ITO/ETL/perovskite/HTL/Au. The materials used to prepare the ETLs were C_{60} and $(RuCp^{*}mes)_2$. The layers were prepared by thermal evaporation in vacuum with a base pressure of $1 \cdot 10^{-6}$ mbar. Two different ETL structures were used in the devices. In one case, a doped layer approach was used, consisting by a 20 nm nm thick doped electron transport layer (C_{60}:$(RuCp^{*}mes)_2$) capped with a 10 nm thick film of the pure C_{60}. Three different concentrations of $(RuCp^{*}mes)_2$ in the doped layers were investigated (12.5 wt%, 6.26 wt% and 2.5 wt%). The second ETL variation consisted of a thin (1 or 2.5 nm) layer of the molecule $(RuCp^{*}mes)_2$ deposited on top of the ITO and covered with 10 nm thick C_{60} film. As a reference, a device with a 10 nm thick C_{60} layer deposited directly on top of ITO was fabricated. Subsequently, the perovskite film was co-evaporated on top of the ETL, following the procedure described in the section **Methylammonium lead iodide film deposition**. The materials used as HTL were TaTm and F_6-TCNNQ. The HTLs were prepared by thermal evaporation of a pure TaTm (10 nm) film followed by a thicker layer (40 nm) of the p-doped material (TaTm:F_6-TCNNQ). Afterwards the metal top contact (Au, 100 nm thick) was deposited. These materials were co-sublimed at temperatures ranging from 135-160 °C for the dopants to 250 °C for the pure charge transport molecules. In doped films, the deposition rate for the TaTm and C_{60} was kept constant at 0.8 Å s^{-1} while varying the deposition rate of the dopants during co-deposition. Pure TaTm, C_{60} and $(RuCp^{*}mes)_2$ layers were deposited at a rate of 0.5 Å s^{-1}.

Fabrication of Tandem perovskite solar cells

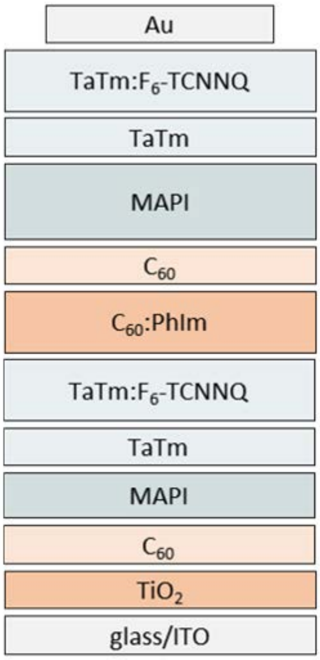

Fig. 9 tandem layout.

The tandem devices followed a n-i-p/n-i-p architecture: ITO/ETL/perovskite/HTL/ETL/perovskite/HTL/Au. On top of the ITO, the TiO_2 dispersion was deposited in air by spin-coating at 3000 rpm for 30 s and annealed at 100 °C for 30 min, leading to a 20-40 nm thick compact layer. The additional layers were prepared by thermal evaporation analogously to the n-i-p fabrication process. The tandem device presents two perovskite layers, one in each sub-cell. Between the perovskites, the charge recombination junction (CRJ) is deposited. The CRJ is constituted by 25 nm of the p-doped hole transport layer (TaTm:F$_6$-TCNNQ) and 25 nm of the n-doped electron transport layer (C$_{60}$:PhIm), deposited on top. The devices were completed with the top HTL, again 10 nm of TaTm followed by 40 nm of TaTm:F$_6$-TCNNQ. Afterwards the metal top contact (Au, 100 nm thick) was deposited.

Methylammonium lead iodide film deposition

The perovskite films were deposited in a vacuum chamber (**Fig. 10**) integrated in a nitrogen filled glovebox equipped with a turbomolecular pump (Pfeiffer TMH 261P, DN 100 ISO-K, 3P) coupled to a scroll pump. The vacuum chamber contains six temperature controlled evaporation sources (Creaphys) fitted with ceramic crucibles. The sources are directed upwards with an angle of approximately 90° with respect to the bottom of the chamber. The distance between the substrate holder and the evaporation sources is approximately 20 cm. Three quartz crystal microbalance (QCM) sensors are used, two monitoring the deposition rate of each thermal source (PbI_2, and CH_3NH_3I), and a third one close to the substrate holder monitoring the total deposition rate. The perovskite evaporations were carried out by co-deposition of the two precursors starting at a pressure of approximately 10^{-6} mbar. The use of clean QCM sensors for each perovskite deposition is important to avoid altered readings due to chemical reactions (perovskite formation) on the sensor. For a more accurate deposition, the actual density of PbI_2 (6.16 g cm^{-3}) is set in the equipment, while for CH_3NH_3I the density is assumed to be 1 g cm^{-3}. The Z-factor for both materials is set to 1. The calibration of the deposition rate for CH_3NH_3I was found to be difficult due to

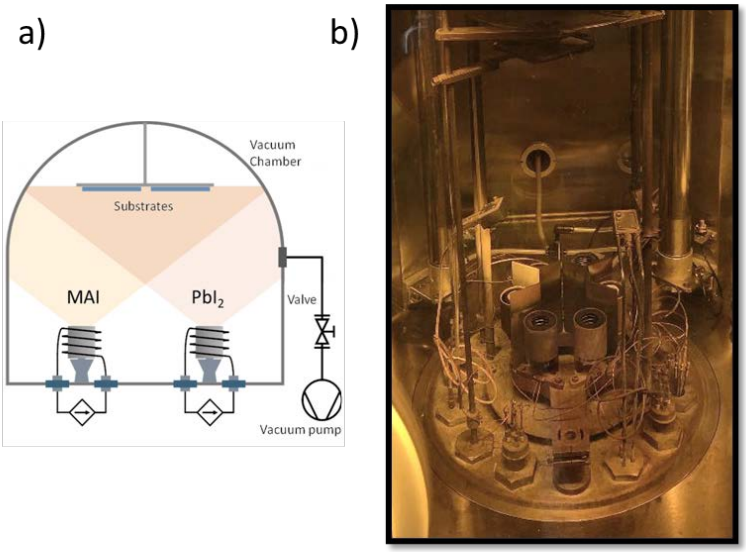

Fig. 10 a) Scheme and **b)** picture of the vacuum chamber used for the dual source vacuum deposition of $CH_3NH_3PbI_3$.

non-uniform layers and the soft nature of the material, which impedes accurate thickness measurements. Instead, the source temperature of CH_3NH_3I was kept constant at 75 °C and the CH_3NH_3I:PbI_2 ratio was controlled offline using X-ray diffraction and optical absorption by adjusting the PbI_2 deposition temperature to obtain a stoichiometric perovskite film. The optimum deposition temperatures were found to be 250 °C for PbI_2 and 70-90 °C for CH_3NH_3I. The target thickness of the perovskite films was set to 500 nm, unless stated otherwise.

Thin film characterization

The thickness of each layer was measured with a mechanical profilometer (Ambios XP-1) on control samples. This measurement allows to optimize the deposition conditions and in particular to calculate a tooling factor by comparing with the inferred thickness from the quartz crystal microbalance (QCM) sensors. These tooling factors allowed us to have a precise control on the thickness of the sublimed layers. Grazing incident X-ray diffraction (GIXRD) patterns were collected at room temperature on an Empyrean PANanalytical powder diffractometer using the Cu $K\alpha_1$ radiation. Typically, three consecutive measurements were collected and averaged into a single diffractogram. (**Fig. 11a**) Optical absorption spectra were collected using a fiber optics based Avantes Avaspec2048 Spectrometer (**Fig. 11b**). Scanning Electron Microscopy (SEM) images were collected on a Hitachi S-4800 microscope operating at an accelerating voltage of 2 kV over samples metallized with Platinum. (**Fig. 11c**)

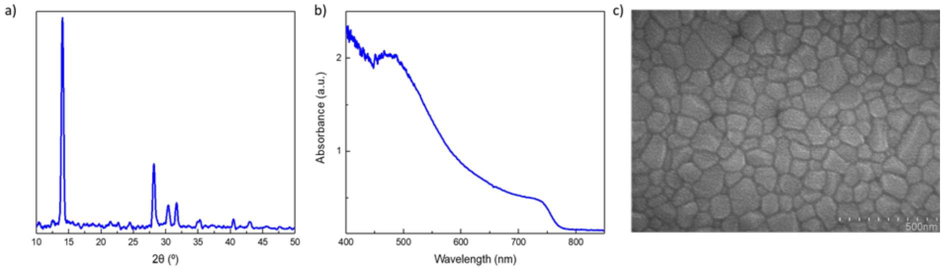

Fig. 11 **(a)** GIXRD pattern, **(b)** optical absorbance and **(c)** surface SEM picture of the vacuum deposited $CH_3NH_3PbI_3$ thin films used in solar cells.

Solar cell characterization

The External Quantum Efficiency (EQE) is the ratio of the number of charge carriers extracted from the solar cell divided by the number of photons of a given energy reaching the device (incident photons). The EQE may be given either as a function of wavelength or as energy. The external quantum efficiency (EQE) was estimated using the cell response at different wavelength (measured with a white halogen lamp in combination with band-pass filters). The solar spectrum mismatch is corrected using a calibrated Silicon reference cell (MiniSun simulator by ECN, the Netherlands).

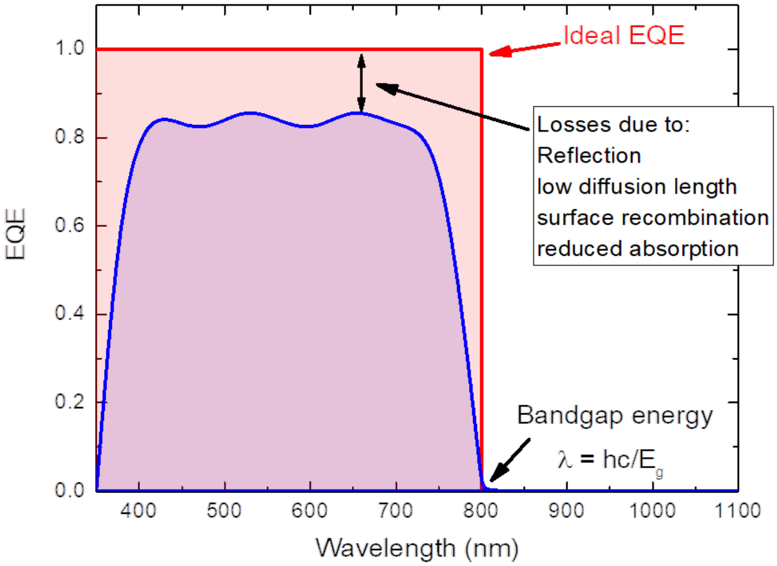

Fig. 12 Characteristic EQE of a typical $CH_3NH_3PbI_3$ perovskite solar cells. The cell's EQE integrated over the whole solar spectrum is equal to the amount of current that the cell will produce when exposed to sunlight.

The current density-voltage (*J-V*) characteristic curve of solar cells can be described with the ideal diode formalism when measured in the dark. In a semilog plot, there are some distinctive regions of the *J-V* curve which can be used to identify the diode working regime as well as different loss mechanisms. Several parameters can be extracted, such as the series resistance, the shunt resistance, the diode saturation current and the ideality factor, all influencing the performance of any photovoltaic device. We can distinguish three regions in the dark *J-V* curve (**Fig. 13**), each dominated by different effects: Region A accounts for the parasitical leakage current from where we can infer the shunt resistance. The Region B is dominated by the diffusion-current, typically described by the Shockley diode equation. From this equation we can calculate the ideality factor and study the charge recombination in the device. In Region C, the current is mainly regulated by drift, and limited by either charge injection or the formation of space charge. From this regime, we can obtain the series resistance.

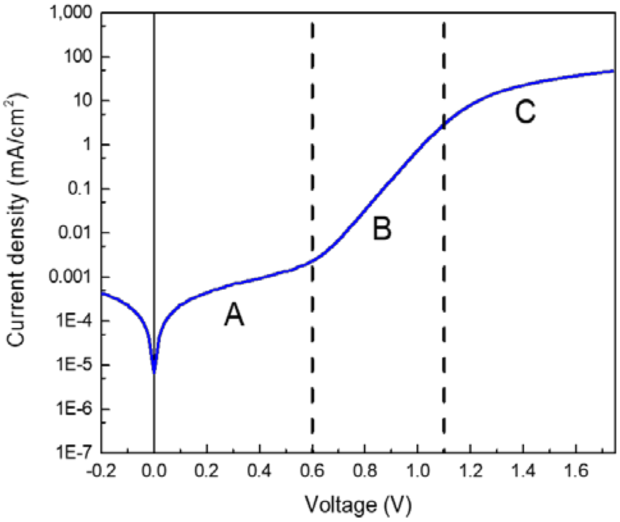

Fig. 13 Semilog plot of a characteristic dark *J-V* curve of a solar cell. The three characteristic regions, ohmic, diffusion and drift current, are highlighted.

The measurement of a solar cell efficiency requires a standardized test. These standardizations allow the comparison of devices manufactured at different companies and laboratories with different technologies.

The main standard conditions for solar cell testing are:[51]

- A lamp that shines with the standardized solar spectrum (AM1.5 G).
- Incident light power (P_{in}) of 100 mW cm^{-2} (one sun).
- Cell temperature of 25 °C.

- Four-wire measurement setup to remove the effect of lead resistance.

Shining light on a device generates a photocurrent in the cell in addition to the dark diode current, and the resulting *J-V* curve is ideally the superposition of both the dark and the photocurrent. **Fig. 14** shows the typical *J-V* curve for an illuminated solar cell, where the main figures of merit are highlighted.

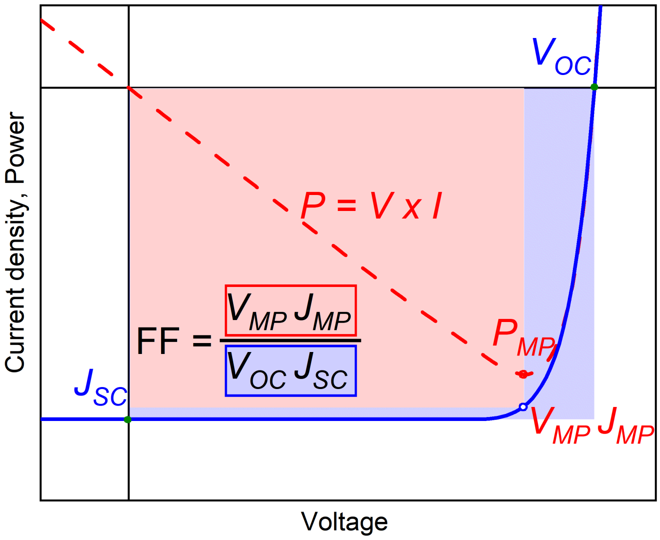

Fig. 14 Typical J-V curve of a solar cell, with highlighted the main parameters used in the characterization.

- **Short circuit current density (*J_{SC}*).** Current density when the voltage is zero, when the two electrodes of the cell are short-circuited. J_{SC} is the largest current which can be drawn from the solar cell.
- **Open circuit voltage (*V_{OC}*).** Voltage across the solar cell when the device is open circuited under illumination (current across the device is zero). This value indicates the maximum voltage attainable from the solar cell.
- **Power density (P).** Product of the voltage and the current density. The maximum value, maximum power point (P_{MP}), occurs where the product of the voltage and the current density are maximum ($V_{MP}J_{MP}$). Ideally it would be V_{OC}

and J_{SC}. Nevertheless, real cells exhibit $V_{MP} < V_{OC}$ and $J_{MP} < J_{SC}$, thus P_{MP} differs from ideality.

- **Fill factor (FF).** Ratio between P_{MP} and P_{ideal}. It indicates how far from ideality the power density of the cell is. It is defined as:

$$FF = \frac{V_{MP} \cdot J_{MP}}{V_{OC} \cdot J_{SC}}$$

Graphically, it can be understood as the "squareness" of the *J-V* curve as the ratio between the areas of the red and the blue rectangles in **Fig. 14**.

- **Power conversion efficiency (PCE).** The efficiency is the most commonly used parameter to compare the performance of one solar cell to another. Efficiency is defined as the percentage of the incident light power that is converted into electrical power:

$$\mathrm{PCE} = \frac{P_{MP}}{P_{in}} = \frac{\mathrm{FF} \cdot V_{OC} \cdot J_{SC}}{P_{in}}$$

The current density-voltage (*J-V*) characteristics were obtained using a Keithley 2400 source-measure unit under white light illumination, and the short circuit current density was corrected considering the device EQE. The electrical characterization was validated using a solar simulator by Abet Technologies (model 10500 with an AM1.5G xenon lamp as the light source). Before each measurement, the exact light intensity was determined using a calibrated Si reference diode equipped with an infrared cut-off filter (KG-3, Schott). The *J-V* curves were recorded between -0.2 and 1.2 V with 0.01 V steps, integrating the signal for 20 ms after a 10 ms delay. This corresponds to a speed of about 0.3 V s^{-1}. The layout used to test the solar cells has four equal areas (0.04 cm^2, defined as the overlap between the ITO and the top metal contact) and measured through a shadow mask with 0.01 cm^2 aperture.

Chapter 3

Influence of doped charge transport layers in p-i-n perovskite solar cells

In this chapter we study the influence of doped and intrinsic transport layers on the performance and stability of thin film perovskite solar cells in a p-i-n configuration. A generic solar cell structure using intrinsic charge extraction layers was developed. This novel device layout leads to efficiencies of 18%, and the operational stability was improved 5 times compared to analogous devices employing doped transport layers.

Reference:

Jorge Ávila, Lidón Gil-Escrig, Pablo P. Boix, Michele Sessolo, Steve Albrecht* and Henk J. Bolink*; *Influence of doped charge transport layers on efficient perovskite solar cells.* **Sustainable Energy Fuels***,* 2018, **2**, 2429-2434. DOI: 10.1039/C8SE00218E

Introduction

In the majority of the reported perovskite solar cells, the absorber layer is sandwiched in between charge selective transport layers.[52] These layers have to ensure rectification, achieved by introducing asymmetric extraction/injection of electrons and holes at the two contacts and resulting in a diode behavior. The generated carriers are displaced from dark equilibrium in the absorber, the charge selective transport layers have to selectively transport and inject charge carriers to the electrodes in which the carriers are at the equilibrium Fermi level.[53] High carrier mobility, long diffusion length and long carrier lifetime can prevent carrier loss during extraction and transport. Hence, their conductivity is frequently enhanced by “doping” them with additives that lead to excess free charges in the material.[54] The benefit of using doped layers is a reduced series resistance and the formation of ohmic contacts to the external electrodes, which enhances the solar cell fill factor. Alnuaimi et al showed that the FF increased from 22% to 80% when the mobility changes from 10^{-6} to 10^{-4} $cm^2 V^{-1} s^{-1}$, together with an increase in J_{SC} from 10 to 20 mA cm^{-2}.[55]

One drawback of the use of doped charge transport layers is their possible negative effect on the device lifetime.[56] The most widely employed hole transport material (HTM) in solution-processed perovskite solar cells is Spiro-OMeTAD, which can lead to state-of-the-art power efficiency.[57–59] Nevertheless, the use of hygroscopic dopants in Spiro-OMeTAD, which trigger degradation of the perovskite film motivates the study of alternative HTMs.[56,60] In solution-processed perovskite solar cells, the semiconducting polymer PTAA[61–64] and P3HT[35] have been used as dopant-free HTM, leading to the latest record efficiencies with improved lifetimes. However, batch-to-batch molecular weight variation of these organic polymers can hinder reproducibility, altering thermal, morphological, and optoelectronic properties.[65] As an alternative, low molecular weight compounds (commonly named as “small molecules”) are versatile with respect to property tuning and demonstrate high batch-to-batch consistency in synthesis, purification and device fabrication. Moreover, small molecules can be processed in thin film by vacuum methods.[66]

The above description applies to solar cells with perovskite layers that are processed from solution, as they are the majority within the field. Much less information is available for solar cells employing perovskite films prepared using dry vacuum processes. Polymer cannot be vacuum processed, hence there are a limited number of examples using sublimed small molecules in perovskite solar cells.[30,67–69] It has been demonstrated that the use of doped small organic molecule layers leads to excellent performances in vacuum deposited perovskite solar cells.[30,47,70,71] In these devices, however, it is essential to prevent direct contact between the perovskite absorber and the doped layers, which would otherwise result in substantial charge recombination. For this reason, a thin film of the intrinsic organic charge transport molecule is usually inserted in between the doped charge transport layer and the perovskite film.[30,70,72] Similar effects are known from research on organic light-emitting diodes and photovoltaic devices, were such intrinsic layers prevent the quenching of excitons.[54] Recently, highly efficient, vacuum deposited (except for the TiO_2 ETL) n-i-p perovskite solar cells without doped transport layers have been reported.[68] The devices presented a high V_{OC} (1.08 V) and FF > 80 %, suggesting an excellent rectification with low carrier recombination losses. However, the operational lifetime was not investigated on those devices. Besides the possible reduced stability associated with the use of doped layers, another drawback is that doping generally leads to parasitic absorption. This is the case, for example, when molecules containing arylamine moieties (which are common building blocks for HTMs) are partially oxidized by the dopants. The radical cation of arylamines has a characteristic optical absorption band in the visible region of the spectrum, in the 500–600 nm range.[73] This parasitic absorption is especially detrimental in p–i–n solar cells, where the sunlight has to pass through the doped hole transport layer prior to reaching the perovskite absorber, reducing the maximum achievable photocurrent the cells can produce. It is therefore of interest to develop p–i–n perovskite solar cells that do not require doped hole transport layers yet do provide efficient charge extraction to the transparent front electrode.

At the same time, it is also relevant to eliminate the doped ETL placed on top of the perovskite film, as this may improve the device stabilities. An alternative to doped layers is the use of thin MoO_3 films acting as the hole injection layers, however, the stability of this contact has not been fully investigated so far.[68,74] In this chapter, the small molecule F_6-TCNNQ is investigated as a candidate to be used as hole injection layer. F_6-TCNNQ is a non-hygroscopic and vacuum-processable molecule, thus being a very attractive candidate for fully vacuum deposited and stable solar cells. Here, we study and compare vacuum-deposited p-i-n solar cells with doped and undoped transport layers, analyzing both their performance and operational stability.

Methodology

The electron and hole selective organic charge transport layers as well as the perovskite films were prepared by vacuum sublimation, as detailed in the **Experimental and methodology** chapter. The chemical structures of the transport materials used to fabricate the devices are presented in **Fig. 15**. We selected TaTm as the HTM due to its very controllable sublimation and tendency to form completely amorphous films. The fullerene C_{60} was selected as the electron transport molecule as it is also easy to sublime and has proven to be an efficient electron acceptor in perovskite solar cells.[40] Doping of the HTL was achieved by co-evaporating the molecule F_6-TCNNQ and TaTm with an F_6-TCNNQ concentration of 11 wt.%. Similarly, the C_{60} layer was doped by co-evaporating the molecule PhIm at a concentration of 30 wt.%.

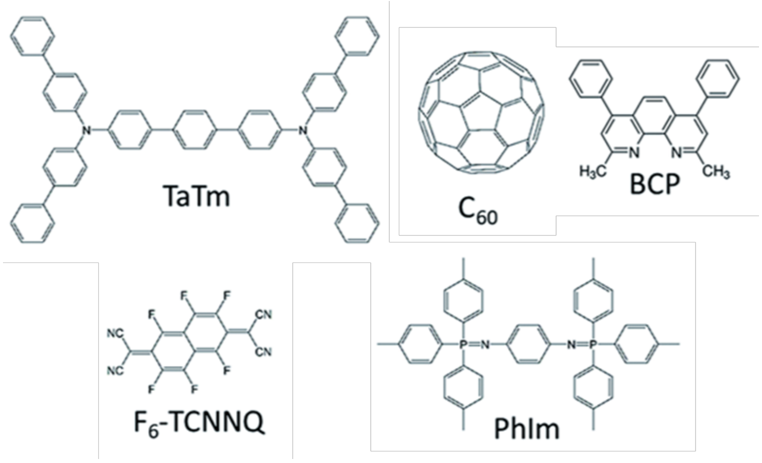

Fig. 15 Chemical structures of the organic semiconductors used as transport materials**.**

Five different types of devices were prepared and evaluated, as depicted in **Fig. 16**, named from A to E. The reference is device A, in which both a doped HTL and a doped ETL were used. In device B the doped HTL was removed and the TaTm layer is in direct contact with the ITO front electrode. Device C mimics the structure of device B, but with a thin layer of F_6-TCNNQ deposited between the ITO and the TaTm. In device D and E, the configuration on the p-contact was the same as for device A and C, while the doped C_{60} layer is substituted by a thin film of BCP. This type of ETL (C_{60}/BCP/Ag) has already been used in organic photovoltaics[75] and later adopted to perovskite solar cells.[76] The thickness of each layer is specified in **Fig. 16**. The different device configurations were prepared in a single perovskite deposition run to ensure that the perovskite layer is identical for all these devices. For each configuration, at least two different substrates each containing 4 cells were evaluated. For the best performing device configurations, extra solar cells were fabricated separately to ensure sufficient statistics.

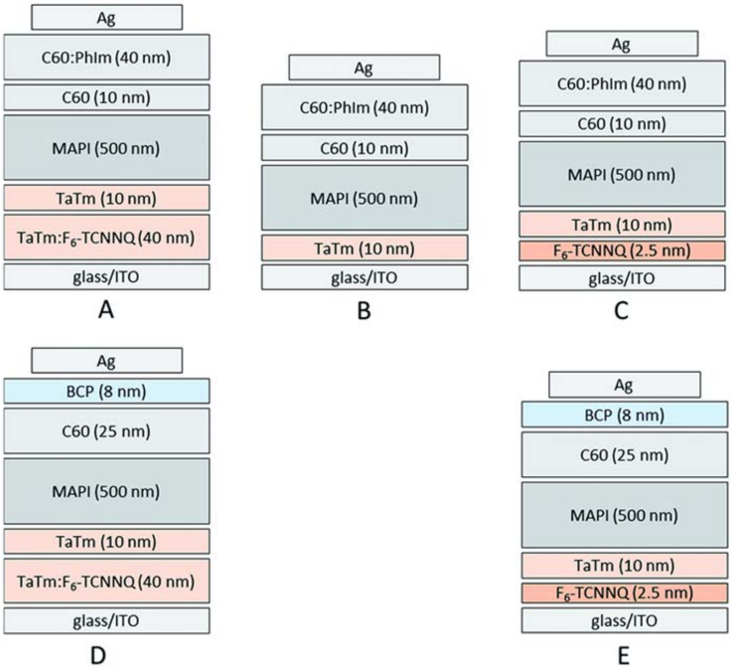

Fig. 16 Layout of the device configurations used for this study. Each one shows a different combination of doped and intrinsic transport layers.

The stability of the solar cells was investigated by continuous exposure to white LED light (spectrum in **Fig. 17a**). The light intensity was adjusted to ensure that the J_{SC} generated by the cells were the same as when they were illuminated by AM 1.5 with 1 sun intensity. The temperature of the cells during this test reached approximately 40 °C in the first 10 minutes and remained constant afterward. The cells were continuously illuminated under short circuit conditions without encapsulation inside a nitrogen filled glovebox. At fixed time intervals, *J-V* scans were collected to deduce the evolution of the characteristic parameters of the cells. This type of measurement allows to determine which parameter is causing the power efficiency decay allowing to postulate possible degradation mechanisms. Some examples of the *J-V* scans for device A at different times of operation under constant illumination are depicted in **Fig. 17b**.

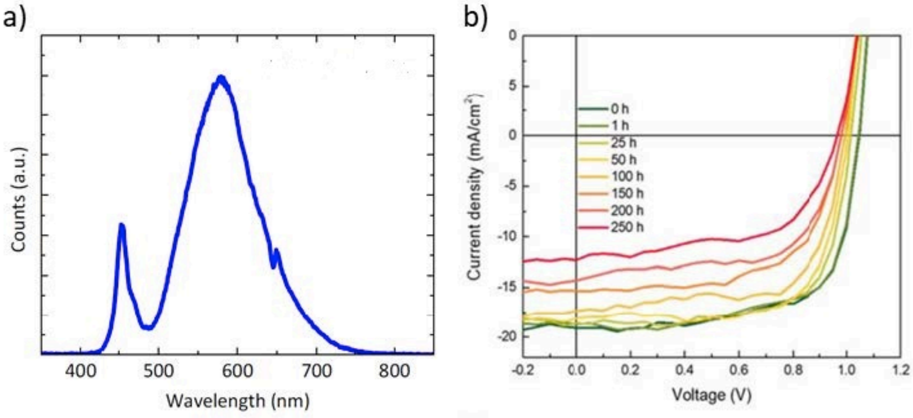

Fig. 17 (a) Optical emission spectrum of the white LED used to illuminate the solar cells during lifetime measurements. **(b)** *J-V* curves measured at various times under continuous illumination for device A.

Results and discussion

The five different device configurations were characterized with AM 1.5G simulated sun illumination. The *J-V* curves under illumination for the reference device A and devices B and C are depicted in **Fig. 18a**. The reference device A performs accordingly to previous reports,[30] reaching a power efficiency of 16.2% with a J_{SC} of 20.7 mA cm^{-2}, a V_{OC} of 1.08 V and a FF of 72%. In device B, when the doped HTL is removed, the *J-V* curve shows a low fill factor with a pronounced S-shape, indicating hindered charge extraction/injection. The origin of this effect is the non-optimal ITO/TaTm interface, as the only difference between devices A and B is the removal of the doped HTL at the ITO contact. The energy offset of 0.6 eV between the work function of ITO

(4.8 eV) and the HOMO of TaTm (5.4 eV), translates into an energy barrier that challenges the extraction and injection of charges.[46] The latter is confirmed by the *J-V* curves measured in the dark (**Fig. 18b**), where the overall current density for device B is much lower than for device A. To overcome the energy barrier, a thin layer (2.5 nm) of F_6-TCNNQ was deposited on top of the ITO prior to the deposition of the TaTm (device C). As can be seen from **Fig. 18a**, the *J-V* curve of this type of device shows good rectification, with a FF as high as 79%. Additionally, the dark *J-V* curve for device C shows a rise in current density similar to device A. These characteristics indicate that the extraction barrier has been essentially removed. Commonly, this effect is explained as a large vacuum level shift due to the interface dipole generated at the electrode interface by a charge injection layer, in this case the F_6-TCNNQ layer. The large vacuum level shift can effectively alleviate the energy difference between he HOMO level of the TaTm and the Fermi level of the electrode, decreasing the barrier.[46] Similarly, high work function transition metal oxide such as MoO_x, RuO_x, VO_x, and organic molecule with large electron affinity (HAT-CN) have been used as hole injection layers in OLEDs[77–79] and solar cells[80,81]. It is interesting to note that removing the highly conductive doped HTL leads to lower leakage currents compared to device A (**Fig. 18b**).

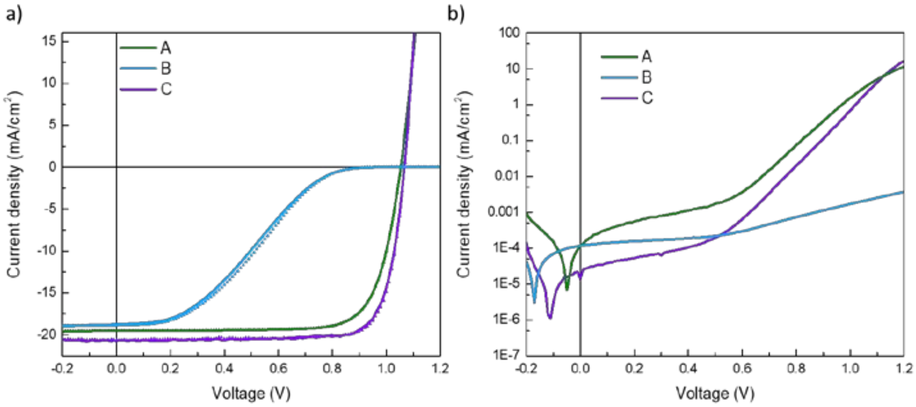

Fig. 18 (a) Representative *J-V* characteristics measured under simulated AM 1.5G illumination in forward (dotted line) and reverse (straight line) scan direction for devices A, B and C. **(b)** Current density versus voltage characteristics for devices A, B and C in the dark.

Importantly, the J_{SC} of the device C is significantly increased. This effect can be understood when comparing the EQE spectra of the different devices (**Fig. 19a**), where once can observe that device C has an enhanced spectral response in the blue-green region of the solar spectrum. The spectral response in this region is strongly influenced by the parasitic absorption of typical doped transport materials, as mentioned before. In **Fig. 19b** the absorption of the two types of HTL employed in devices A and C are depicted. These layers were prepared on glass substrates resembling the stack used in the solar cells. Indeed, there is a substantial decrease in the absorption spectrum for the double-layer HTL of device C when compared to that of the reference device A. The reduction in the visible part of the spectrum is primarily due to the absence of the absorption band around 500 nm (due to doping). Even though it is likely that at the interface between F_6-TCNNQ and TaTm a small fraction of TaTm molecules are oxidized, this does not lead to a significant optical absorption of the HTL. This reduction in the parasitic absorption leads to more light reaching the perovskite, which therefore explains the increase in J_{SC} for this configuration. Moreover, the double-layer type HTL used in device C shows excellent transmittance up to 1300 nm, which makes it a valuable option for use in tandem applications with low bandgap absorbers such as silicon.

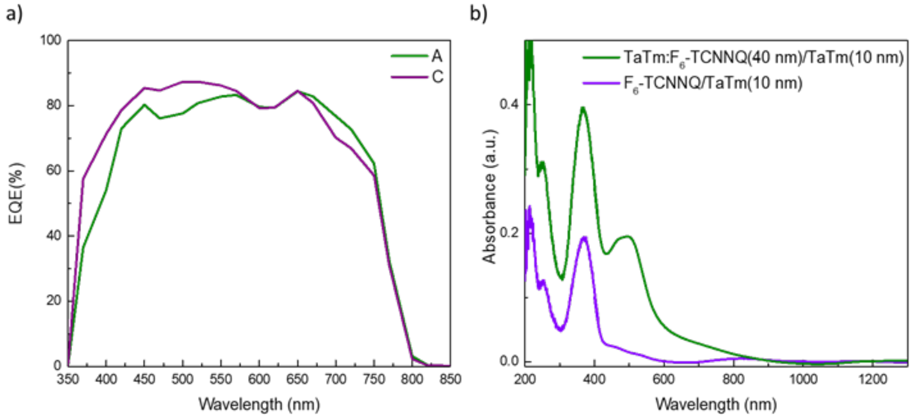

Fig. 19 (a) External quantum efficiency (EQE) spectra for devices type A and C **(b)** Absorbance spectra of the hole transport layers for devices A and C.

Devices D and E have J_{SC} and V_{OC} which are similar to those of devices A and C, respectively. (**Fig. 20** and **Table 1**) The similar current densities are expected as the front contacts are unvaried and the effect of the top charge transport layer on the optical absorption is small. The latter effect is due to the use of a thick perovskite film which absorbs virtually all the sunlight in the first pass. Interestingly, the bilayer C_{60}/BCP ETL leads to diodes with high rectification, comparable to the much more conductive C_{60}/C_{60}:PhIm layer, as evidenced by the high FF obtained.

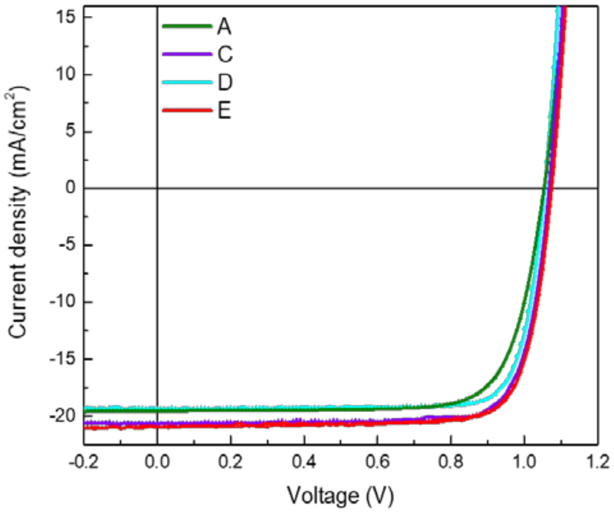

Fig. 20 *J-V* characteristics measured under simulated AM 1.5G-illumination in forward (dotted line) and reverse (straight line) scan direction for devices A, C, D and E.

Table 1 *J–V* parameters of the best devices for each configuration, measured under standard AM 1.5G illumination. Due to the very small hysteresis, no difference among the forward and reverse scans can be seen**.**

	PCE (%)	**J_{SC} (mA cm^{-2})**	**V_{OC} (mV)**	**FF (%)**
A	16.2	20.8	1076	72.5
B	5.4	18.8	1032	27.9
C	17.9	21.3	1056	79.4
D	16.9	19.6	1052	81.7
E	18.2	21.3	1059	80.4

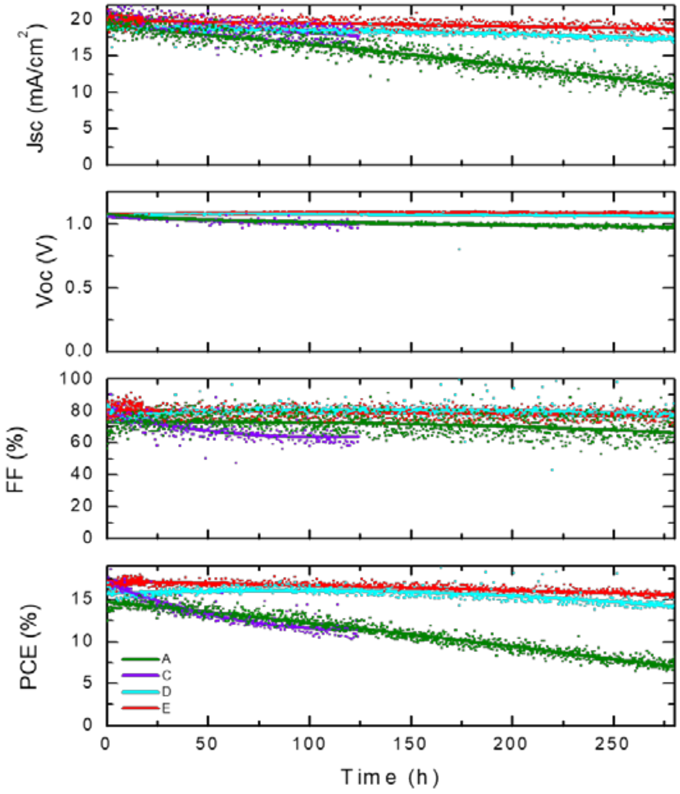

Fig. 21 *J-V* characteristic parameters versus time measured under continuous LED illumination in inert atmosphere. Devices are maintained at short circuit conditions and each hour a *J-V* scan is performed.

The evolution of the performance parameters over time is depicted in **Fig. 21**. We can distinguish two types of behavior for the different devices. Devices D and E, both having the C_{60}/BCP/Ag top contact, are stable over more than 280 hours under continuous illumination, with only a relative decrease of ~10% in the PCE. This reduction is mainly due to a drop in J_{SC}. Interestingly, the V_{OC} increases slightly over the first 100 hours, which we postulate is due to the passivation of trap states within the perovskite film under illumination, as previously reported.[82] A very different behavior is observed for devices A and C that employ the C_{60}/C_{60}:PhIm top contact. These devices are less stable, as observed by a reduction in the PCE to 80% of the initial value after approximately 100 hours of operation. The decay in these cases appears to be driven by all parameters and especially by the J_{SC} and the FF, which drop faster than in devices with intrinsic ETLs. These results indicate that the deterioration of these cells is related to an increase in the series resistance, which is likely to relate with the de-doping of the ETL, as this layer is protected only by a sublimed (not-pinhole free) metal electrode. De-doping would lead to an extraction barrier at the metal interface, decreasing the FF and current density in agreement with our observations.

Chapter 4

$(RuCp^*mes)_2$ as a sublimable n-dopant for n–i–p perovskite solar cells

In this chapter we investigate the use of pentamethylcyclopentadienyl mesitylene ruthenium dimer, $(RuCp^*mes)_2$*, as a dopant for* C_{60} *in fully vacuum-deposited n–i–p perovskite solar cells. The* $(RuCp^*mes)_2$ *was either co-evaporated with the fullerene or deposited as a pure thin film on top of the transparent electrode prior to the deposition of the fullerene. Both the co-evaporated blends and the bilayers are efficient electron transport layers, leading to solar cells with efficiencies up to 18%.*

Reference:

Jorge Ávila, Maria-Grazia La-Placa, Elena Longhi, Michele Sessolo*, Stephen Barlow, Seth R. Marder and Henk J. Bolink; *Ruthenium pentamethylcyclopentadienyl mesitylene dimer: a sublimable n-dopant and electron buffer layer for efficient n–i–p perovskite solar cells*. **J. Mater. Chem. A**, 2019, **7**, 25796-25801.

DOI: 10.1039/C9TA09838K

Introduction

The most efficient perovskite solar cells reported so far have in common the use of TiO_2 as the electron transport material (ETM).[35,83] These devices are built in an n-i-p architecture using a mesoporous TiO_2 layer on top of the transparent conductive oxide, generally FTO. Other electron transport materials that have been studied so far in perovskite solar cells are either n-type metal oxide (SnO_2,[84,85] ZnO[86] among others) or organic semiconductors.[87,88] Compared to their inorganic counterparts, organic electron transport materials have some advantages, such as optoelectronic properties that are easily tailored by chemical modification, simple and low-temperature processing and batch-to-batch reproducibility.[89] Among these materials, PCBM and C_{60} have been widely used as ETMs in perovskite solar cells, due to their favorable high electron affinity, and their ability to reduce the density of trap states by passivating the surface of the perovskite layer.[90] These properties lead to a highly reduced non-radiative recombination and hysteresis while maintaining a high fill factor.[91–93] In particular, the denser solid state packing of C_{60} facilitates the intermolecular charge transport that leads to higher electron mobility compared to chemically modified fullerenes. Moreover, C_{60} has relatively low manufacturing costs and can be processed in thin films by vacuum sublimation. Given all these properties, C_{60} is widely adopted as ETM in highly efficient perovskite solar cells.[30,94,95]

In order to guarantee an efficient charge extraction from the ETL to the TCO, the alignment between the LUMO of the ETL and the work function of the electrode is crucial. The large energy difference between the electron affinity of C_{60} and the work function of ITO results in a Schottky barrier height of about 0.8 eV, which leads to a non-ohmic interface, limiting the charge extraction. A common approach to reduce the energy mismatch between a semiconductor and an electrode, and thus reduce ohmic losses, is to increase the charge-carrier density in the organic semiconductor through doping. As a consequence, the Fermi level in the doped semiconductor will shift towards the filled states, reducing the height and width of the barrier and favoring charge transfer.[54] Interfacial contact of the doped C_{60} with the perovskite would increase the non-radiative recombination. This loss can be prevented by depositing an intrinsic C_{60} layer between the perovskite and the n-doped C_{60}. To prevent intermixing of the doped and intrinsic layers, sequential vacuum sublimation is the most suitable deposition method.[96]

Several dopants have been employed to n-dope fullerene in perovskite solar cells, increasing the efficiency as compared to devices using intrinsic C_{60} as ETL. The hydride donor 1,3-dimethyl-2(4-(diphenylamino)phenyl)-2,3-dihydro-1H-benzoimidazole has been used for the bulk doping of solution-processed C_{60} ETL films.[97] Sequential solution deposition of C_{60} and poly(allylamine) followed by annealing, leads to the formation of N–C_{60} covalent bonds and n-doping.[98] However, some of these dopants can lead to the formation of undesirable side products, some presents air instability, while others can only be processed from solution.[99–101] An example of a vacuum processed n-dopant is the molecule PhIm. Using the organic molecule PhIm to dope C_{60} our group showed highly efficient fully evaporated n-i-p and p-i-n devices.[30] Other compounds suitable for this purpose are dimers formed by 19-electron organometallic sandwich compounds (as well as those formed by some organic radicals)[102], which combine strong reducing ability, selective reactivity (forming solely the corresponding monomeric cations upon doping), and moderate air stability, while being processable both from solution and in vacuum. In view of these favorable properties, they have been used to n-dope a wide variety of semiconductors, including fullerenes.[102–105] Of most relevance to the present work, a thin layer of one such organometallic dimer – pentamethylrhodocene dimer, $(RhCp^*Cp)_2$ – has been vacuum deposited between FTO and vacuum-deposited C_{60}, pinning the Fermi level to the LUMO of the C_{60}.[106] In this chapter, we describe the use of a similar organometallic compound – pentamethylcyclopentadienyl mesitylene ruthenium dimer,[107] $(RuCp^*mes)_2$ – to dope C_{60} in fully vacuum deposited n–i–p perovskite solar cells.

Methodology

The chemical structures of the organic semiconductors used to fabricate the devices are presented in **Fig. 22**. The dimer $(RuCp^*mes)_2$ was synthesized by collaborators at Georgia Institute of Technology following previously published protocols.[48] To evaluate the reactivity among the dopant $(RuCp^*mes)_2$ and the fullerene C_{60} we followed two approaches. In one, both materials were co-sublimed at the same time leading to a homogeneous C_{60}:(RuCp*mes)$_2$ layer with a thickness of 20 nm. In the other approach we deposited a bilayer formed by a thin film of (RuCp*mes)$_2$ covered by C_{60} (10 nm). In this case the contact and hence the eventual reaction between the materials presumably occurs mainly at the interface between them.

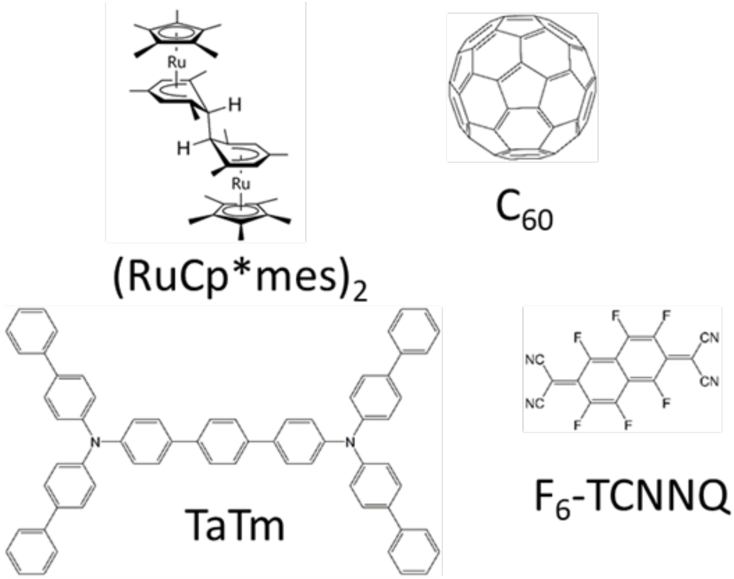

Fig. 22 Chemical structures of the organic semiconductors used in the preparation of perovskite solar cells. C_{60} is the electron transport material while (RuCp*mes)$_2$ is used as the n-dopant. TaTm is the hole transport material and F_6-TCNNQ is the p-dopant.

The chosen device architecture was an n-i-p configuration where the ETL is directly deposited on top of the glass/ITO front contact. The layout of the devices is as follows: ITO/ETL/C_{60}/MAPI/TaTm/TaTm:F_6-TCNNQ/Au. The thickness of each layer is specified in **Fig. 23**. Two different batches of devices were prepared. In the first, the ETL is the co-evaporated C_{60}:(RuCp*mes)$_2$ layer. Three dopant concentrations were studied: 2.5 wt%, 6.25 wt% and 12.5 wt% (**Fig. 23a**). In the other batch we studied the effect of a pure layer of (RuCp*mes)$_2$ deposited in between the ITO electrode and the C_{60}. The thickness of (RuCp*mes)$_2$ is either 1 nm or 2.5 nm (**Fig. 23b**). Additional devices without any interlayer were prepared as a reference. Here, the C_{60} is in direct contact with the ITO. All the layers were prepared by vacuum sublimation following the protocols described in the **Experimental and methodology** chapter. The different device configurations were prepared in a single perovskite sublimation run to ensure that the perovskite layer is identical for all these devices.

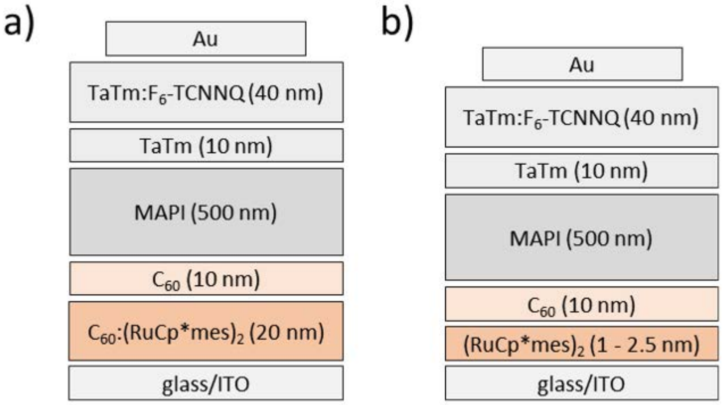

Fig. 23 Schematics of the vacuum-processed perovskite solar cells. In **(a)** the ETL is a co-evaporated C_{60}:$(RuCp^*mes)_2$ film with a dopant concentration of 2.5 wt%, 6.25 wt% or 12.5 wt%. In **(b)** the ETL is a $(RuCp^*mes)_2$ layer with a thickness of 1 nm or 2.5 nm.

Results and discussion

Initially, we prepared a batch of devices with the co-sublimed C_{60}:$(RuCp^*mes)_2$ film. In **Fig. 24a** the current density vs. voltage curves for the solar cell using the three different dopant concentrations (2.5 wt%, 6.25 wt% and 12.5 wt%) are shown. The device using C_{60} with 12.5 wt% dopant concentration as the ETL shows excellent carrier extraction (FF of approximately 79%) and a V_{OC} of 1.07 V. Together with the J_{SC} of 19.2 mA cm^{-2}, it leads to a power conversion efficiencies of 16.1% (Statistics in **Table 2**). The device with a lower concentration of dopant (6.25 wt%) presents excellent rectification without significant changes in the FF (80%) or the V_{OC} (1.07 V). Nevertheless, the J_{SC} is increased to 20.1 mA cm^{-2} enhancing the PCE of the cell to 17.1%. In the EQE spectra (**Fig. 24b**), the main feature is a decrease in charge generation around 450 nm when the concentration of dopant is reduced or, in other words, when the relative amount of C_{60} increases. We can correlate the loss in charge generation in the 400–500 nm range with the parasitic absorption of C_{60} in this spectral region (transmittance spectrum of doped C_{60} in **Fig. 24b**). Overall, the EQE spectrum for the device with a dopant concentration

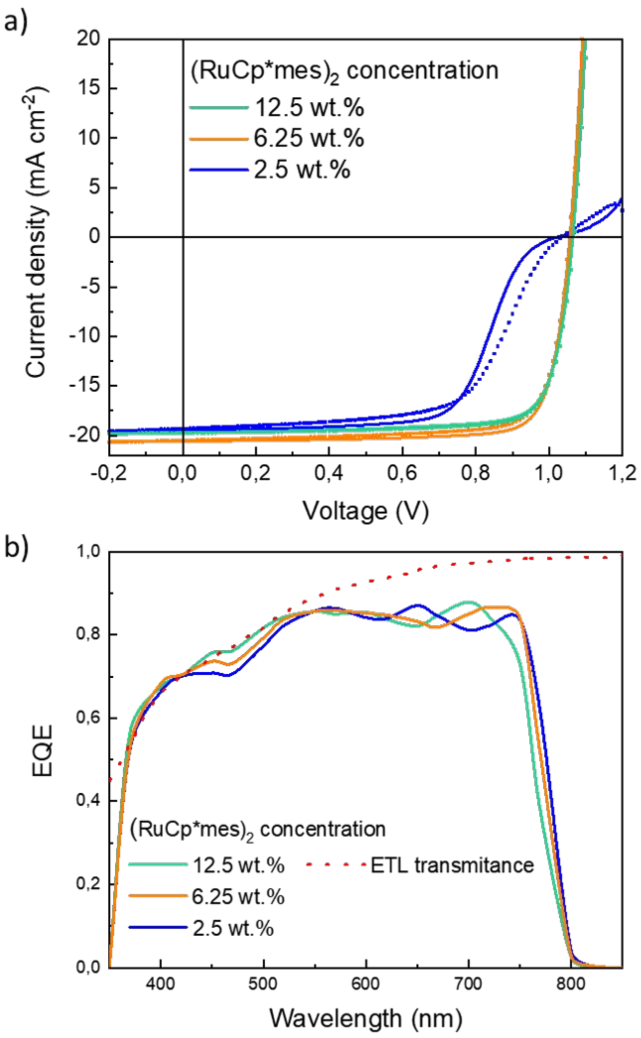

Fig. 24 (a) Representative *J-V* curves measured under simulated 1 sun illumination in forward (straight line) and reverse (dotted line) scan directions and **(b)** EQE spectra for a series of devices with different dopant concentration in the ETL. The dotted red line corresponds to the transmittance spectrum of the C_{60}:(RuCp*mes)$_2$ ETL with a dopant concentration of 12.5 wt%.

of 6.25 wt% leads to the highest integrated current density, in line with the best performance among the device series. Decreasing further the dopant concentration to 2.5 wt%, caused a pronounced s-shape (FF = 58%), indicative of inefficient charge collection at the front contact. The low FF together with the reduced V_{OC} indicates that the C_{60}:$(RuCp^*mes)_2$ layer at this dopant concentration is no longer able to effectively reduce the interface energy barrier, increasing the recombination losses. The *J–V* curve shows also hysteresis between the forward and reverse scans, indicating charge accumulation at the non-ohmic ITO/ETL interface (**Fig. 24a**).

In order to rationalize the interaction of $(RuCp^*mes)_2$ with C_{60} and the poor transport properties at low dopant concentration, we measured the conductivity of the layers used as ETL. For pure thin films of C_{60} and $(RuCp^*mes)_2$, the conductivity is of the order of 10^{-8} S cm^{-1}, as expected for intrinsic and highly pure organic semiconductors. The conductivities of the different dopant concentrations in the C_{60}:$(RuCp^*mes)_2$ ETLs are presented in **Fig. 25.** The conductivity decreases from about 0.5 S cm^{-1} for a dopant concentration of 12.5 wt% to about 0.05–0.1 S cm^{-1} for the lowest concentration of 2.5 wt%, which correlates with the observed trend in the FF. In comparison with a previous report,[30] the conductivity of the ETL with a dopant concentration of 2.5 wt% should be sufficiently high to guarantee efficient charge transport. However, the low performance observed here indicates that at 2.5 wt% dopant concentration there is an inefficient charge collection through the interface between the ITO and C_{60}, leading to low FF and poorly working devices.

Table 2 Statistical distribution of *J-V* parameters of devices with different dopant concentrations measured under standard AM1.5G illumination.

ETL	Dopant concentration	PCE (%)	J_{sc} (mA cm^{-2})	V_{oc} (V)	FF (%)
C_{60}:$(RuCp^*mes)_2$	12.5 wt%	16.1 ± 0.5	19.2 ± 0.4	1.07 ± 0.01	79 ± 1
	6.25 wt%	17.1 ± 0.4	20.1 ± 0.5	1.07 ± 0.02	80 ± 1
	2.5 %wt%	11.3 ± 1.3	19.4 ± 0.6	1.00 ± 0.04	58 ± 5

Table 3 *J–V* parameters of the best devices for each configuration measured under simulated solar illumination.

ETL	Dopant concentration	PCE (%)	V_{OC} (V)	J_{SC} (mA cm^{-2})	FF (%)
C_{60}:(RuCp*mes)$_2$ (20 nm)	12.5 wt.%	16.9	1.07	19.8	80
	6.25 wt.%	17.7	1.06	20.6	81
	2.5 wt.%	12.5	1.02	19.5	63
Without ETL	—	2.6	0.82	13.6	23
(RuCp*mes)$_2$ (1 nm)	—	17.1	1.09	20.1	78
(RuCp*mes)$_2$ (2.5 nm)	—	3.1	0.96	13.5	24

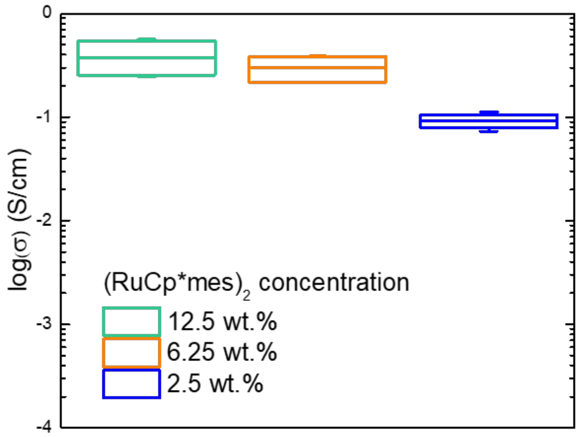

Fig. 25 Electrical conductivity of the electron transport layers used in each device varying the dopant concentration in C_{60}.

We then studied a second batch of devices with a pure layer of (RuCp*mes)$_2$ deposited in between the ITO and the C_{60}. The architecture was the same n–i–p configuration as described previously in **Fig. 23b**. An additional device without the (RuCp*mes)$_2$ interlayer was prepared as a reference. In this additional device the C_{60} is directly in contact with ITO. The representative *J–V* curves for this device series are represented in **Fig. 26a**. The reference solar cells with the bare ITO/C_{60} interface shows a poor rectification, with very low FF (23%) and a low V_{OC} (0.82 V). This is caused by the presence of an energy barrier that results in non-ohmic charge extraction, reducing the

FF and causing non-radiative recombination losses limiting the maximum achievable V_{OC}. Interestingly, when a very thin layer of $(RuCp^*mes)_2$ (1 nm) is introduced between the ITO electrode and C_{60}, the device performance is recovered, with good rectification (FF = 78%) and V_{OC} as high as 1.09 V. Taking into account the photocurrent density (J_{SC} = 20.1 mA cm^{-2}), we obtained a PCE exceeding 17%. This performance is similar to the one of the record cells with n-doped C_{60}, but with an enhanced V_{OC} (30 mV, record device performances are represented in **Table 3** and **Fig. 26a**). This increase in V_{OC} indicates that avoiding the use of doped layers can mitigate non-radiative recombination losses. We can conclude that the $(RuCp^*mes)_2$ can efficiently dope C_{60} not only in homogeneous mixtures of the two materials, but even when the materials are in contact only at the interface. This is in agreement with the strong reducing character of $(RuCp^*mes)_2$, which is easily capable of n-doping a large variety of organic semiconductors.[103,108,109] Nevertheless, if the thickness of the $(RuCp^*mes)_2$ layer is slightly increased to 2.5 nm, the device shows a poor charge extraction, similarly to the device with bare C_{60} as ETL. This behavior suggests a very low electron mobility in the pure $(RuCp^*mes)_2$, which is essentially blocking the carrier collection when too thick. This is somewhat different to what was previously observed for a similar dopant ($(RhCp^*Cp)_2$), where devices with a nominal interlayer thickness of 10 nm resulted in large V_{OC} and FF.[106] We believe that the differences may originate from different diffusivity of the two organometallic dopants into the C_{60}, as well as from the lower work function of FTO used in the previous work, which would favor electron extraction. In **Fig. 26b** we can observe similar EQE spectra for the devices using the two types of ETL architectures, the co-evaporated C_{60}:$(RuCp^*mes)_2$ and the bilayer $(RuCp^*mes)_2/C_{60}$, with EQE values of about 0.8 over the whole spectral range. Nevertheless, the device with doped C_{60} exhibits a slightly lower EQE in the blue region of the spectrum. This difference correlates with the ETL thickness as the devices with doped C_{60} have a total ETL thickness of 30 nm. This results in a larger parasitic absorption compared with that of the bilayer structure, where a C_{60} film with a thickness of only 10 nm was used.

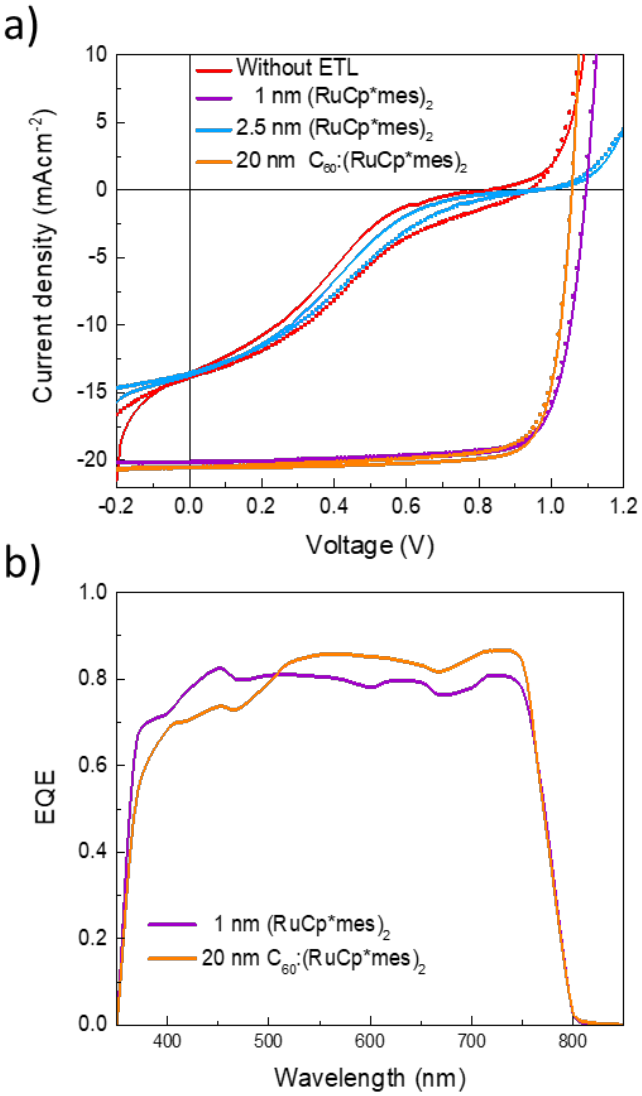

Fig. 26 (a) Representative *J–V* characteristics measured under simulated solar illumination in forward (straight line) and reverse (dotted line) scan direction for devices employing different ETL. **(b)** External quantum efficiency (EQE) spectra for the devices with $(RuCp^*mes)_2$ and C_{60}:$(RuCp^*mes)_2$ as the ETL.

Chapter 5

High voltage vacuum-deposited tandem solar cells

In this chapter we explore an optically optimized double junction $CH_3NH_3PbI_3$*-*$CH_3NH_3PbI_3$ *tandem solar cell. The stack design was calculated by optical modeling and fabricated through vacuum techniques. The tandem shows excellent characteristics with efficiencies larger than 18%, higher than the individual sub-cells, and* V_{OC} *of 2.3 V, among the highest obtained for any perovskite-based solar cell.*

Reference:

Jorge Ávila, Cristina Momblona, Pablo Boix, Michele Sessolo, Miguel Anaya, Gabriel Lozano, Koen Vandewal, Hernán Míguez* and Henk J. Bolink*; *High voltage vacuum-deposited* $CH_3NH_3PbI_3$*–*$CH_3NH_3PbI_3$ *tandem solar cells.* **Energy Environ. Sci.**, 2018, **11**, 3292-3297. DOI: 10.1039/C8EE01936C

Introduction

Record power conversion efficiencies of perovskite solar cells are approaching the thermodynamic limit established by the Shockley-Queisser theory, which sets the maximum power conversion efficiencies (PCE) achievable for single junction cells depending on the bandgap energy (E_g) of the absorbing material.[41] The use of multi-junctions or tandem solar cells is a successful strategy to overcome the PCE limit of single junction photovoltaic technologies.[4] The working principle of tandem solar cells is based on the combination of two or more light absorbers that allow harvesting a broad region of the solar spectrum reducing the thermalization losses intrinsic to a single junction device.[42]

Based on the electric connection among sub-cells, tandems are classified as two- or four-terminal. A four-terminal tandem solar cell is made of two independent cells that are externally connected, as a convenience, in series or parallel. In a two-terminal device, the sub-cells are monolithically and electrically stacked, requiring a recombination layer or a tunnel junction to achieve ohmic current flow and Fermi level pinning. In this kind of device, the sub-cells are connected in series and the current through the different sub-cells is ideally the same, while their voltages are summed. Among the different architectures, two-terminal tandem solar cells are industrially attractive due to easier management of the generated power and the reduced cost since a lower amount of transparent conductive materials is required. As a result, devices with lower current density but improved voltage can be demonstrated, maintaining high the efficiency. The benefit is also a reduced loss related to series resistance at the contacts, enabling larger area solar cells.[110] In addition, the intrinsic high voltage in such systems is interesting per se for other applications such as photovoltaic-driven electrochemical cells, including direct power conversion from solar to chemical fuels as hydrogen production from water splitting (required voltages higher than 1.4-1.9V)[111] and carbon dioxide reduction to carbon monoxide or hydrocarbons.[112]

A special case of two-terminal tandem, widely studied in organic photovoltaics, is the homo-tandem where the same absorber is used in both sub-cells. The combination of the same absorber for each junction is employed to compensate for the absorption of materials with either low optical density or moderate charge carrier transport properties. The distance that charges must travel is reduced as the absorber in each sub-cell is thinner than in single junction devices, facilitating an efficient light harvesting.[113–118] Also, as opposite charge carriers generated in the front and back cell recombine in the charge recombination layer junction in between the two cells, the generated current is reduced by a factor of two, this allows for the use of less conductive TCOs.

Perovskites are excellent candidates for tandem devices due to their tunable optoelectronic properties and simple processing.[119] Perovskite-silicon solar cells are reaching outstanding performances. The two-terminal tandem architecture has reached a PCE of 29.15%, already higher than single junction Silicon and GaAs solar cells, and 27.1% for four-terminal configuration.[4,120] Also, the combination with CIGS has led to tandem cells with a PCE of 23.26%.[121] Nevertheless, the tuneability of the perovskite bandgap has allowed the fabrication of perovskite–perovskite tandems, reaching PCE of 24.8%,[122–124] and the first trials of all-perovskite triple-junction tandems, that can potentially reach PCEs higher than 30%.[125,126] In general, reports use different perovskites for each sub-cell, with an optimized combination of band-gaps according to the detailed balance model.[127] The efficiency of the monolithic all-perovskite tandem solar cells is mainly limited by the large V_{OC} deficit in the wide-bandgap perovskite and the optical loss caused by the tunnel recombination junction. Where typically a 1.77 eV bandgap perovskite is used and barely reaches a V_{OC} of 1.2 V, meaning losses around 300 mV compared to the theoretical maximum V_{OC} of 1.5 V.[42,119]

Therefore, it is of interest to examine the potential of double junction solar cells using the same $CH_3NH_3PbI_3$ absorber in both sub-cells. Nevertheless, perovskite tandems using the same absorber in both sub-cells have not been optimized so far.[128] It is necessary to develop optical modeling accounting for the light absorption and electric field distribution in the different layers comprising the device, as previously demonstrated for single junction perovskite solar cells.[129,130] The complex nature of the multilayered tandem device requires a technique capable of accurately reproducing the layer thicknesses extracted from the optical modeling. In this regard, vacuum processing offers a deposition control over the film thickness at the nanometer scale, both for the perovskite and the transport layers.[131–133] The deposition is carried out at room temperature and complex layer structures can be sublimed to secure low ohmic losses and high transparency.[30] Although this configuration will not benefit from reduced thermalization losses, it still has the previously mentioned advantage of high voltage and reduced current density. Furthermore, charge recombination layers developed for homo-tandems can be directly applied to hetero-tandems.

Methodology

Through optical modeling the light absorption in each sub-cell was optimized to avoid current mismatch. Initially, the optical constants of the different materials employed in the devices were determined for individual thin films. With these optical constants, we used a model that optimizes the thickness of each layer in the devices to minimize the current mismatch between the sub-cells, resulting in an optimum light harvesting. **Table 4** summarizes the results of the modeling, indicating the optimal thickness for each layer. Small deviations between the calculated optimum values and the experimental ones are due to the need of maintaining the thickness of the intrinsic charge transport layers as low as possible, to compensate for their low charge mobility. Based on this design, $CH_3NH_3PbI_3$-$CH_3NH_3PbI_3$ tandem solar cells with the layout depicted in **Fig. 27** were prepared. Reference single junction devices were also prepared to mimic the structure of each of the sub-cells. Specifically, the structure of the front sub-cell was ITO/TiO_2/C_{60}/$CH_3NH_3PbI_3$/TaTm/TaTm:F_6-TCNNQ/Au while that of the back sub-cell was ITO/C_{60}:PhIm/C_{60}/$CH_3NH_3PbI_3$/TaTm/TaTm:F_6-TCNNQ/Au (**Fig. 27**). The devices were prepared following the protocols described in the **Experimental and methodology** chapter.

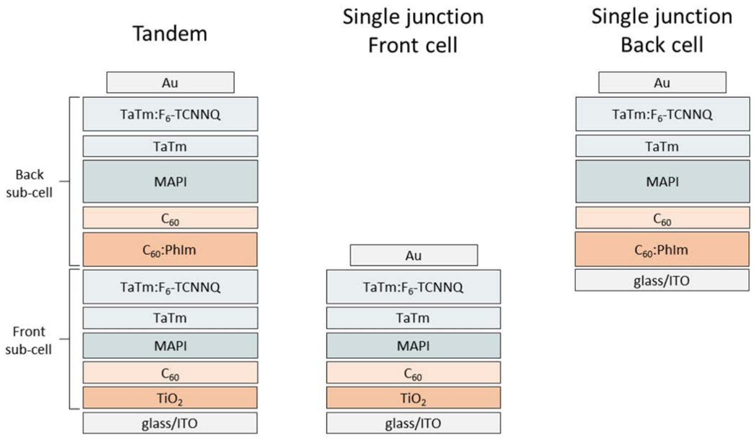

Fig. 27 Scheme of the device structures studied in this work. The single junction devices mimic the layout of each sub-cell in the tandem.

Table 4. Optimized thickness of each layer in the best performing devices.

Layer	Sim. thickness (nm)	Exp. thickness (nm)
Air	Semi-infinite	
Glass	1.1×10^6	1.1×10^6
ITO	140	140
TiO_2	25	30
C_{60}	10	10
Front perovs	95	90
TaTm	40	10
Doped TaTm	35	25
Doped C_{60}	38	25
C_{60}	10	10
Back perovs	420	400
TaTm	26	10
Doped TaTm	29	40
Gold	100	100

Results and discussion

The materials and structures selected for the sub-cells in the tandem derive from previous works, where high performance was achieved (PCE > 18%).[30,71] These combinations of materials and device layouts guarantee an appropriate band alignment and charge transport within the charge selective contacts and the perovskite film. The front sub-cell employs a solution processed TiO_2 electron selective layer on top of the transparent conductive oxide. (**Fig. 27**) This configuration was selected as it produces one of the highest V_{OC} among $CH_3NH_3PbI_3$ solar cells for single junction devices (1.17 V).[71] The back sub-cell uses instead the structure C_{60}:PhIm/C_{60} as the electron transport layer.[30] This ETL is fully-evaporated, enabling a straightforward deposition on top of the front sub-cell. The charge carrier recombination layer is constituted by the combination of the doped TaTm:F_6-TCNNQ and the C_{60}:PhIm layers. The connection of both doped materials guarantees a suitable ohmic contact, with high electrical conductivity and low optical absorption.[134]

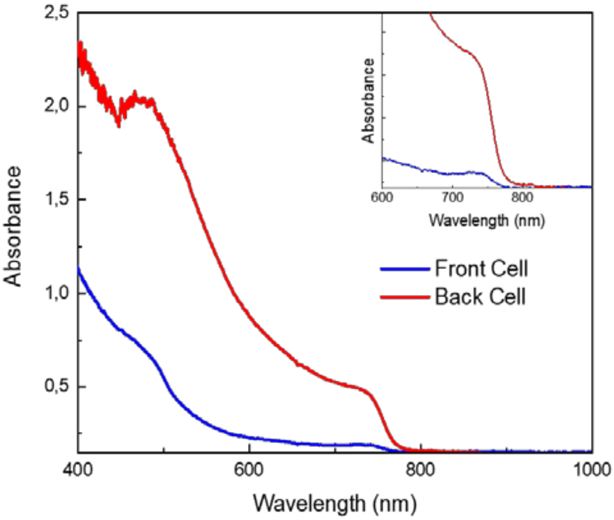

Fig. 28 Perovskite absorbance spectra of front cell and back cell. The inset is a magnification of the absorption onset.

The perovskite thickness of each sub-cell is considerably dissimilar, 95 nm versus 420 nm (**Table 4**). As both perovskites are absorbing in the same spectral region, a thin front perovskite is needed to allow enough light to be transmitted and reach the back sub-cell. Light penetration in the device depends strongly on the incident wavelength. Calculation indicates that most of the high-energy photons are absorbed within the first few nanometers of the front perovskite layer. If this layer is thin enough, the low-energy photons can be transmitted and absorbed in the back perovskite (**Fig.**

28). As estimated from the simulation, the front sub-cell would generate 10.35 mA cm^{-2} while the back sub-cell 10.21 mA cm^{-2}, leading to a rather small current mismatch (0.14 mA cm^{-2}). On the other side, the simulated thicknesses reveal the importance of keeping below 40 nm the thickness of the transport layers, to minimize the impact of parasitic absorption. This is of special importance for the organic layers that are on the front side of the tandem. Small deviations between the calculated optimal values and the experimental ones were meant to minimize the thickness of the intrinsic charge transport layer to compensate for their low charge mobility. Some small experimental deviations (plus or minus 25 nm) were observed for the perovskite thickness. **Table 4** shows the average experimental values.

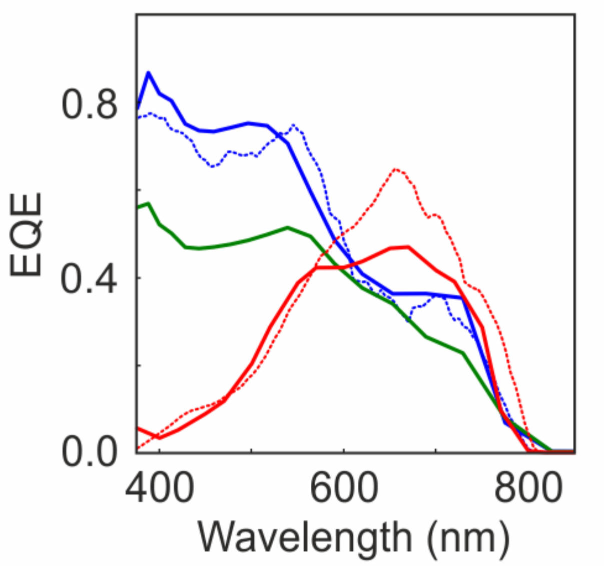

Fig. 29 Spectral dependence of the experimental (solid line) and calculated (dashed line) external quantum efficiency (EQE) associated to the front (blue line) and back (red line) sub-cells. The green line shows the measured EQE for the complete tandem device.

The calculated and experimental EQE are displayed in **Fig. 29**. The calculation was performed assuming all the harvested light is converted into photocurrent. Using the single junction devices (**Fig. 27**), the representative EQE of each sub-cell was measured. The model reproduces properly well the optical features presented in both individual front and back cells. There are clear spectral differences in the carrier generation of each sub-cell. We noticeably observe that the front sub-cell generates carrier mainly in the blue region of the solar spectral, while the back sub-cell reaches its carrier generation maximum at 700 nm. This result illustrates that we were able to distinct high-energy photons from low-energy photons using absorbers with the same bandgap. Nonetheless, in the tandem device there is a homogeneous carrier generation over the complete spectral range.

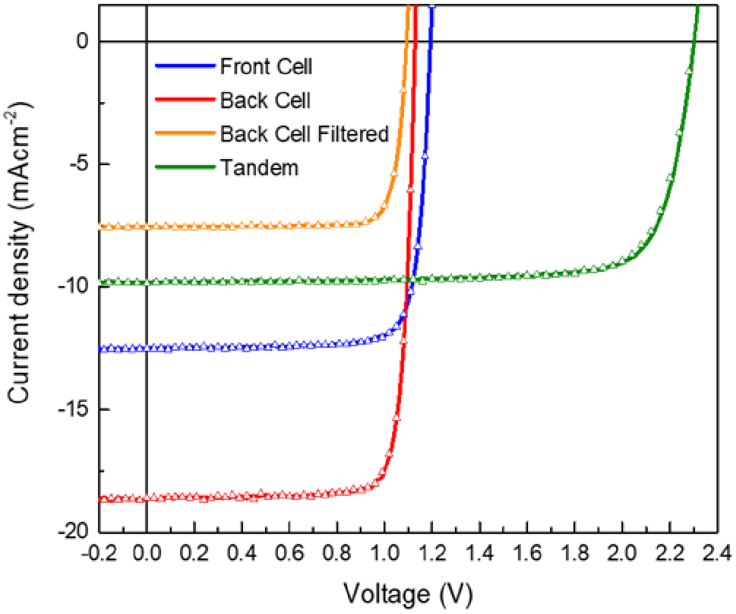

Fig. 30 *J*-*V* characteristics under 1 sun illumination for the single junction cell with the thin perovskite layer (mimicking the front cell in the tandem configuration) as the blue curve, the single junction cell with the 400 nm perovskite layer (red curve), that cell but illuminated through a filter consisting of glass/$CH_3NH_3PbI_3$ film with a thickness of 90 nm (mimicking the back sub-cell in the tandem configuration), orange curve and the 2T tandem cell (green curve). Symbols indicate the reverse scans, from open to short circuit.

The current versus voltage (*J*-*V*) curves of the tandem and the single junction reference cells are depicted in **Fig. 30**. Both single junction reference cells show high performance. The high fill factor (>80%) is indicative of an optimum charge transport and low extraction barrier at the contacts, in agreement with previous reports using the same transport materials.[30,71] Noticeably, the front cell achieves a V_{OC} of 1.19 V, indicating a reduced non-radiative losses, due to a minimized bulk recombination consequence of the thin perovskite layer. This value is very close to the theoretical limit of approximately 1.3 V assuming a bandgap energy of 1.6 eV.[135,136] The front and back cells present short circuit currents (J_{SC}) of 12.5 and 18.7 mA cm^{-2}, respectively. These values are expected considering that the perovskite layers are thinner as compared to a typical single junction device. The front cell with a current density of 12.5 mA cm^{-2} exceeds the predicted 10.35 mA cm^{-2} for the tandem. We relate this surplus to back reflections on the metal electrode. We believe that in the case of the tandem the extra light would be absorbed by the back sub-cell. On the other hand, the back cell presents a higher current than the calculated for the back sub-cell in the tandem (18.7 versus 10.21 mA cm^{-2}). To mimic the conditions of the sub-cell in the tandem configuration, the current density was measured under filtered illumination. The filter consisted of a glass/$CH_3NH_3PbI_3$ sample with the same perovskite thickness used in the front cell (Orange line in **Fig. 30**). As a consequence, the J_{SC} is reduced approximately by half, decreasing to 7.52 mA cm^{-2}. The V_{OC} is still high (1.09 V) and the FF is slightly increased due to the smaller influence of the series resistance when the current density is reduced. **Table 5** reviews the solar cells characteristics. The *J-V* curve of the tandem device is shown in **Fig. 30** too. The curves present a FF near 80% and almost unnoticeable differences between the forward and reverse scans, which emphasize the quality of the charge recombination layer. The measured V_{OC} reached 2305 mV, very close to the sum of the photovoltages of the reference cells (only 15 mV lower). The J_{SC} of the tandem is slightly higher than the measured for the reference back cell, 9.84 versus 7.52 mA cm^{-2}. It was expected that the back cell, producing 7.52 mA cm^{-2}, would limit the current density in the tandem as the cells are in series in the monolithic configuration. We relate the mismatch between the filtered back cell and the tandem back sub-cell to optical losses in the sample employed as a filter (a 20% loss in transmittance was measured due to the glass substrate). In the tandem configuration such optical losses are avoided and the J_{SC} is close to the calculated value (10.16 mA cm^{-2}). As a result, the tandem achieves a power conversion efficiency of 18.02%, that exceeds the efficiencies of both single junction devices.

Table 5 *J*-*V* parameters of the reference cells and tandem devices measured under standard AM1.5G illumination.

	V_{OC} (V)	J_{SC} (mA cm^{-2})	FF (%)	PCE (%)
Reference Front Cell	1.19	12.53	81.54	12.16
Reference Back Cell	1.13	18.66	83.31	17.55
Ref Back Cell filtered	1.09	7.52	83.83	6.88
Tandem	2.30	9.84	79.58	18.02

We also evaluated the shelf life of the tandems. We measured the devices several days after the fabrication and they showed similar performances without the appearance of hysteresis or a significant drop in any parameter. In **Fig. 31a** we show a device measured up to 17 days after its fabrication. The efficiency dropped only from 16.72% to 16.55%, as the FF decreased by about 2%. Nevertheless, the V_{OC} and J_{SC} slightly increased, helping to maintain the initial efficiency. In **Fig. 31b** we present a tandem device with a larger active area (0.36 cm^2) compared with the standard in our laboratory (0.04 cm^2). The device presents similar characteristics as the tandem prepared on small areas, reaching an efficiency of 17.2%. This area is still far from that eligible for certification (around 1 cm^2).[137] However, the FF was found to be still high (79%) when the area is increased 9 times, indicating that the homo-junction cells presented here are promising candidates for large area applications.

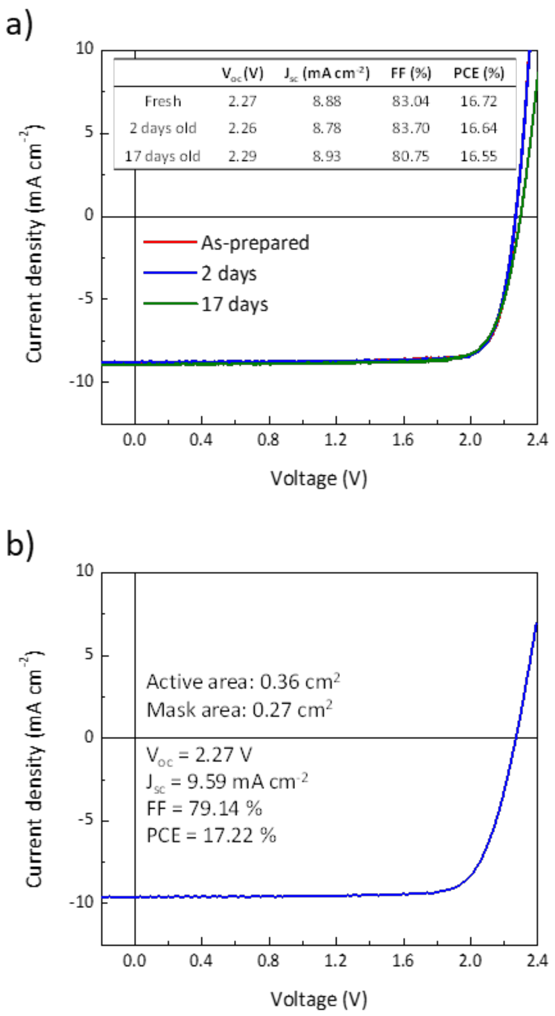

Fig. 31 *J-V* characteristics under 100 mW cm^{-2} illumination for homojunction tandem solar cells. **a)** Shelf life stability measurement. The device was kept in nitrogen between measurements. **b)** Large areas measurement. The active area was 0.36 cm^2 and the shadow mask area 0.27 cm^2.

Chapter 6

Conclusions

The work included in this thesis has been structured in three sections. After the discussion of the results for each chapter, the main conclusions are highlighted below.

In chapter 3, the performance and stability of planar p–i–n perovskite solar cells, with and without doped charge transport layers, were investigated. On the p-type contact, the replacement of the doped charge transport layer with alternative intrinsic materials was shown to be beneficial for the device performance. In particular, we identified an energy barrier for charge injection/extraction at the ITO-TaTm interface. Nevertheless, the insertion of a very thin layer of the pure p-type molecular dopant in between the ITO and the HTL, was found to eliminate the energy barrier, leading at the same time to a reduction of the parasitic absorption. This results in an enhancement of the spectral response in the blue part of the solar spectrum and hence to an increase in the current density. On the other hand, the improvement in the solar cell stability emanated from the removal of the doped electron transport layers on top of the perovskite. The bilayer C_{60}/BCP ETL led to diodes with high rectification comparable to the much more conductive C_{60}/C_{60}:PhIm contact, as evidenced by the high FF obtained. Overall, we showed the potential of interfacial doping to prepare stable and transparent charge transport layers, and to fabricate very efficient and stable solar cells. The strategies identified here can be extrapolated to a wider range of transport materials and applied to different perovskite single junction and tandem solar cells.

In chapter 4, we have demonstrated the possibility of using $(RuCp^*mes)_2$ as an n-dopant for C_{60} in vacuum-deposited n-i-p perovskite solar cells. Two different approaches were used to combine C_{60} and $(RuCp^*mes)_2$ as electron transport layers. The co-evaporated C_{60}:$(RuCp^*mes)_2$ formed homogeneous film between the ITO and the intrinsic fullerene, establishing ohmic contact between them. Optimization of the dopant concentration allowed the fabrication of solar cells with power conversion efficiency approaching 18%. In the bilayer approach ($(RuCp^*mes)_2/C_{60}$) the thickness of the $(RuCp^*mes)_2$ was found to be critical to obtain well working devices. Only when the dopant layer was as thin as 1 nm, we observed efficient charge extraction with power conversion efficiency exceeding 17%. We noted a higher V_{OC} for solar cells using the bilayer $(RuCp^*mes)_2/C_{60}$ ETL, which is a consequence of the diminished charge recombination as compared to doped, highly conductive layers. The developed ETLs can also be applied in p-i-n solar cells and as part of the charge recombination layer in monolithic tandem devices.

In chapter 5, we have demonstrated $CH_3NH_3PbI_3$–$CH_3NH_3PbI_3$ homo-tandem solar cells prepared by vacuum deposition. An optical model was used to calculate the ideal configuration of the tandem device, determining accurately the thickness of each layer. This was verified by the minor difference between the measured current density of the tandem and the one calculated by the model. The use of molecular charge recombination layer led to low voltage losses and allowed to obtain very high open circuit voltage (2.3 V) in the tandem solar cells. Globally, the efficiency reached similar values to that single junction devices (>18%), yet with a reduced current density and enhanced voltage. These results validate the use of vapor processed for the development of complex perovskite device architectures, such as multijunction solar cells.

Chapter 7

Resumen en castellano

Introducción

Un nuevo paradigma energético

La energía es crucial para la actividad de las sociedades modernas y para el desarrollo socioeconómico de las futuras generaciones. En la actualidad, dependemos en gran medida de las fuentes de energía fósiles, con alrededor del 80% de la energía producida proveniente del petróleo y el carbón. La combustión de estos materiales a gran escala genera una inmensa cantidad de residuos que son imposibles de asimilar por nuestro ecosistema al ritmo de generación actual. Entre ellos destaca el dióxido de carbono como principal responsable del calentamiento global. En consecuencia, el mayor desafío de nuestro tiempo es cambiar el paradigma energético hacia fuentes de energía renovables, entre las cuales destaca la energía solar. Este tipo de energía es prácticamente ilimitada y las tecnologías para aprovecharla se están desarrollando rápidamente, lo que la convierte en uno de los candidatos más importantes para la producción de energía renovable.

Entre las diferentes tecnologías para aprovechar la luz solar, la fotovoltaica (PV) es una de las más prometedoras debido a su capacidad de convertir directamente fotones en electrones. Las células solares se pueden clasificar en tres generaciones. Las células de primera generación están fabricadas con silicio cristalino y policristalino. Estas tecnologías dominan el mercado fotovoltaico, con más del 80% de la cuota de mercado global en términos de producción anual.[3] La segunda generación de células solares se caracteriza por el uso de semiconductores de "bandgap" directo como silicio amorfo, CdTe y CIGS. Estos semiconductores son varios órdenes de magnitud más eficientes absorbiendo la luz solar que el silicio cristalino, disminuyendo así el espesor de material necesario para fabricar las células solares. Sin embargo, a pesar de las propiedades ópticas mejoradas, su presencia en el mercado mundial sigue siendo inferior al 10%. Estas dos generaciones suelen tener en común procesos de fabricación complejos y de altas temperaturas.

Por otro lado, se está desarrollando una nueva generación de células solares que comprenden varias tecnologías de película delgada aún en fase de investigación o desarrollo. La energía fotovoltaica emergente incluye células solares CZTS, células solares sensibilizadas por colorantes, células solares orgánicas, células solares de puntos cuánticos y células solares de perovskita. Entre las diferentes tecnologías, las células solares de perovskita han recibido una gran atención debido a las altas eficiencias alcanzadas a escala de laboratorio en un tiempo relativamente corto, con eficiencias que alcanzan el 25%.[4] Debido a su fácil procesabilidad junto con sus excelentes propiedades optoelectrónicas, las células solares de perovskita tienen el potencial de transformar el paradigma energético tal y como lo conocemos hoy en día.

Perovskitas

Una perovskita es cualquier compuesto que comparta la estructura cristalina del titanato de calcio ($CaTiO_3$), que se puede simplificar con la fórmula ABX_3, donde A y B son cationes y X es un anión. La estructura de la perovskita está formada por el catión B en coordinación octaédrica con el haluro X en los vértices (BX_6). Los octaedros de halogenuros metálicos se distribuyen compartiendo los vértices en una estructura 3D extendida, donde los cationes A ocupan la cavidad intersticial entre ocho octaedros. La estructura cristalina de una perovskita cúbica se representa en la **Fig. 1**. En los semiconductores de perovskita empleados en células solares, el catión A suele ser una molécula orgánica, generalmente metilamonio ($CH_3NH_3^+$) o formamidinio ($NH_2CH{=}NH_2^+$), o el catión inorgánico cesio (Cs^+). El anión X es un haluro, generalmente yodo, mientras que el catión B ha sido tradicionalmente Pb^{2+}, dando lugar a los principales materiales para células solares eficientes. Sn^{2+} también se ha utilizado como catión B, aunque su fácil oxidación conlleva problemas de estabilidad que ha limitado su uso en células solares. Sin embargo, las perovskitas mixtas de Sb-Pb han demostrado recientemente un alto rendimiento energético y estabilidad mejorada.[8] La estructura de perovskita arquetípica es el triyoduro de plomo y metilamonio ($CH_3NH_3PbI_3$, comúnmente denominado MAPI), que exhibe propiedades eléctricas y ópticas favorables para la fotovoltaica:

- Alto coeficiente de absorción.[15]
- Baja energía de enlace de los excitones.[16–18]
- Alta movilidad de electrones y huecos.[19,20]
- Gran longitud de difusión de cargas.[22–26]

Todas estas características han convertido a este tipo de perovskitas en uno de los materiales más prometedores entre las tecnologías fotovoltaicas de nueva generación.

Deposición al vacío

Existen diferentes metodologías para depositar las perovskitas en capa delgada, que van desde técnicas basadas en disoluciones, como el "spin-coating", a métodos de deposición de alto vacío. Los métodos de deposición de alto vacío ofrecen una serie de ventajas en la preparación de películas delgadas de perovskita:

- Alta pureza de los materiales sublimados.
- Control sobre el grosor de la capa.
- Proceso intrínsecamente aditivo.
- Procesamiento en seco.
- Compatible con área grande.
- Compatibilidad con sustratos sensibles o superficies no planas.

La evaporación de las capas de perovskita se lleva a cabo mediante la sublimación térmica simultánea de los precursores, generalmente una sal orgánica ($CH_3NH_3I_3$) y un haluro metálico (PbI_2). En condiciones estequiométricas, los precursores, colocados en fuentes térmicas, se subliman y condensan en un sustrato sobre el que crece la película de $CH_3NH_3PbI_3$.

La investigación sobre dispositivos sublimados de perovskita ha progresado enormemente en los últimos años, alcanzando eficiencias del 20%.[30] Recientemente, numerosos estudios están conduciendo hacia una mejor comprensión de los procesos que rigen la deposición térmica de perovskitas.[27,31–34] Estos hallazgos fomentan el desarrollo de dispositivos procesados al vacío con el potencial de alcanzar las eficiencias récords de las células solares de perovskita procesadas en solución.

Arquitecturas de dispositivo

Las células solares de perovskita se pueden clasificar principalmente en dos grupos, en función de la parte del dispositivo expuesta a la luz solar. Cuando la luz penetra en el dispositivo a través de la capa de transporte de electrones, la arquitectura se denomina n-i-p, en el caso contrario, el dispositivo se denota como p-i-n. Generalmente, la luz incide en los dispositivos a través de la interfaz de vidrio/TCO, por lo tanto, esta notación está habitualmente relacionada con la secuencia de fabricación en la que se depositan las capas (**Fig. 2**).

La arquitectura n-i-p es la utilizada mayoritariamente para las células solares de perovskita procesadas por disolución. La ETL consiste generalmente en una capa compacta de TiO_2 seguida de una capa mesoporosa del mismo material. Por otro lado, la HTL más comúnmente utilizado en estos dispositivos es Spiro-OMeTAD. Recientemente, algunas alternativas como PTAA y P3HT también se han empezado a utilizar como HTL, alcanzando eficiencias récords.

La mayoría de las células solares p-i-n usan una configuración plana. Las HTL más utilizados en la estructura p-i-n son PEDOT:PSS, PTAA y NiO_x; entre las ETL, los más comunes son el fulereno C_{60} y sus derivados.[36–40]

Nuestro grupo ha desarrollado células solares de perovskita tanto n-i-p como p-i-n completamente evaporadas, utilizando una configuración plana.[30] Los dispositivos presentan estructuras simétricas gracias a que la evaporación permite depositar las capas en orden arbitrario. La HTL utilizada en los dispositivos es generalmente TaTm y la ETL C_{60}, con sus respectivos dopantes, F_6-TCNNQ como dopante p y PhIm como dopante de tipo n (**Fig. 3**).

Los dispositivos tándems están constituidos por dos o más subcélulas conectadas eléctricamente. Cada una de las subcélulas es capaz de absorber una parte diferente del espectro electromagnético, reduciendo las pérdidas por termalización y pudiendo alcanzar eficiencias más altas en comparación con las células de unión simple (**Fig. 4**). El interés en la perovskita para su uso en dispositivos tándems está en continuo aumento, existiendo ya numerosos ejemplos de dispositivos tándem basados en perovskita con altas eficiencias de conversión energética.

Fundamentos de las células solares

El elemento principal de una célula solar es el semiconductor (la perovskita) encargado de absorber la luz solar, transformando los fotones en portadores de carga (electrones y huecos). Esta conversión es posible gracias a la estructura de banda electrónica de los semiconductores. Por un lado, la banda de valencia es responsable del transporte de los huecos (cargas positivas). Por el otro, la banda de conducción es responsable del transporte de los electrones (cargas negativas). La diferencia de energía entre la banda de valencia y la banda de conducción se conoce como “bandgap”.

Debido a su carga opuesta, el electrón y el hueco pueden interaccionar culómbicamente en un estado enlazado conocido como excitón. La energía requerida para romper el excitón depende de la constante dieléctrica del material, que en el caso de las perovskitas es alta, lo que conduce a bajas energías de enlace del excitón.[18]

Los electrones y huecos se deben extraer selectivamente por los materiales de transporte de cargas, recolectándose en los electrodos. La alineación de los niveles de energía entre los diferentes materiales controla la inyección/extracción de carga. Reducir la barrera de energía en estas interfaces es crucial para logar una inyección/extracción de carga eficiente y sin pérdidas de recombinación. Un enfoque habitual para mejorar las propiedades de transporte de los semiconductores es el dopaje. La conductividad puede aumentar varios órdenes de magnitud en función de la concentración de dopante, reduciendo las pérdidas por resistividad.[46,47]

Objetivos de la tesis

El objeto de esta tesis es el estudio de células solares de perovskita depositadas al vacío, tanto de unión simple como tándem, y la optimización de las capas de transporte de carga para maximizar el rendimiento y la estabilidad de los dispositivos. El trabajo se ha estructurado en tres secciones:

- Capítulo 3: Influencia de las capas de transporte dopadas en células solares de perovskita de tipo p-i-n.
- Capítulo 4: Aplicación de $(RuCp^*mes)_2$ como un dopante tipo-n sublimable para células solares de perovskita n-i-p.
- Capítulo 5: Fabricación de células solares tándems $CH_3NH_3PbI_3$-$CH_3NH_3PbI_3$ depositadas en alto vacío.

Metodología experimental

Materiales

La preparación y la caracterización de las células solares de perovskita se llevó a cabo en sala limpia de clase 10000. Todos los materiales empleados en este trabajo están disponibles comercialmente y se han empleado sin previa purificación.

Fabricación de las células solares

Todas las capas que forman los dispositivos están depositadas al vacío a no ser que se indique lo contrario. Los dispositivos estudiados en esta tesis utilizaron las siguientes arquitecturas:

- **p-i-n** Con una estructura por capas: ITO/HTL/perovskita/ETL/Ag. (**Fig. 7**) Usando como HTL F_6-TCNNQ y TaTm, y como ETL C_{60}, PhIm o BCP.
- **n-i-p** Con una estructura por capas: ITO/ETL/perovskita/HTL/Au. (**Fig. 8**) En esta arquitectura la capa de HTL es siempre: TaTm/TaTm:F_6-TCNNQ, mientras que la ETL está formado por diferentes combinaciones de C_{60} y $(RuCp^*mes)_2$.
- **Tándem** Con la siguiente estructura (**Fig. 9**) : ITO/TiO_2/C_{60}/$CH_3NH_3PbI_3$/TaTm/ TaTm:F_6-TCNNQ/C_{60}:PhIm/C_{60}/$CH_3NH_3PbI_3$/TaTm/TaTm:F_6-TCNNQ/Au.

Deposición a vacío de la capa de perovskita ($CH_3NH_3PbI_3$)

La deposición de las capas de perovskita se llevó a cabo en una cámara de alto vacío integrada en una caja de guantes de atmósfera inerte (**Fig. 10**). Los materiales utilizados para preparar la perovskita $CH_3NH_3PbI_3$ fueron CH_3NH_3I y PbI_2, que se colocan en crisoles dentro del sistema donde se calientan de manera controlada. Los sustratos se sitúan a 20 cm de las fuentes, separados por un obturador que controla el inicio y fin de la deposición. La velocidad a la que se depositan los materiales se controla mediante tres sensores (microbalanzas de cuarzo). Para la deposición, el CH_3NH_3I se mantiene a temperatura constante de 75 °C mientras se aumenta lentamente la temperatura de PbI_2 hasta alcanzar la estequiometría deseada, aproximadamente a una temperatura de 250 °C. El espesor de las capas de perovskita es de 500 nm a menos que se indique lo contrario.

Caracterización de capa fina

Las principales medidas realizadas para caracterizar las capas son:

- Perfilometría mecánica para la medición del grosor de las capas.
- Difracción de rayos-X con incidencia rasante (GIXRD).
- Espectroscopia de absorción.
- Microscopía electrónica de barrido (SEM).

Caracterización de células solares

Los principales parámetros que se utilizan para caracterizar las células solares aparecen descritos a continuación (**Fig. 14**):

- Densidad de corriente de cortocircuito (J_{SC}, mA cm^{-2}, representa la corriente generada a 0 V).
- Voltaje de circuito abierto (V_{OC}, V, es el máximo voltaje generado por una célula solar cuando la densidad de corriente es igual a 0).
- Factor de forma o "fill factor" (FF, %, se define como la relación entre el punto de máxima potencia dividido entre el producto de V_{OC} y J_{SC}. Gráficamente representa la "cuadratura" de la curva de densidad de corriente frente al voltaje).
- Eficiencia de conversión de potencia (PCE, % expresada por el cociente del punto de máxima potencia de la célula y la potencia irradiada sobre el dispositivo).
- Eficiencia cuántica externa (EQE, %, representa el número de electrones extraídos mediante los contactos dividido por el número de fotones incidentes sobre el dispositivo).

Influencia de las capas de transporte dopadas en células solares de perovskita de tipo p-i-n

Introducción

En la mayoría de las células solares de perovskita, la capa fotoactiva se intercala entre capas de transporte selectivo de cargas.[52] Estas capas garantizan la rectificación mediante la extracción/inyección asimétrica de electrones y huecos, dando como resultado un comportamiento de tipo diodo. Alta movilidad, larga longitud de difusión y largo tiempo de vida medio de las cargas son factores importantes que disminuyen las pérdidas por recombinación durante la extracción y el transporte. Para evitar este tipo de perdidas, es común que la conductividad de los materiales de transporte se mejore mediante dopaje, el cual genera un exceso de cargas libres.[54] El uso de capas dopadas tiene como beneficios la reducción de la resistencia en serie y la formación de contactos óhmicos con los electrodos externos, lo que mejora el FF de las células solares. Un inconveniente relacionado con el uso de capas dopadas es que el dopaje generalmente induce la aparición de absorción óptica parasítica. Este es el caso, por ejemplo, de las moléculas que contienen sustituyentes de arilamina (un grupo funcional común para HTM) cuando son parcialmente oxidadas por los dopantes. El catión radical de las arilaminas tiene una banda de absorción óptica característica en la región visible del espectro, en el rango de 500–600 nm.[73] Esta absorción parasítica es especialmente perjudicial en las células solares de tipo p-i-n, donde la luz solar pasa a través de la capa de transporte de huecos antes de alcanzar la perovskita, lo que reduce la máxima fotocorriente alcanzable. Por lo tanto, es importante desarrollar células solares de perovskita tipo p-i-n que no requieran capas de transporte de huecos dopadas y que a su vez proporcionen una extracción de cargas eficiente. Al mismo tiempo, también es de interés la eliminación de la ETL dopada colocada encima de la capa de perovskita, ya que los materiales dopados son muy reactivos y pueden disminuir la estabilidad del dispositivo.

En este capítulo, la molécula F_6-TCNNQ se ha investigado como candidata para ser utilizada como capa de inyección de huecos. F_6-TCNNQ es una molécula no higroscópica y sublimable, siendo así un candidato ideal para fabricar células solares estables y depositadas completamente al vacío. Aquí estudiamos y comparamos las células solares tipo p-i-n depositadas al vacío con capas de transporte dopadas y sin dopar, analizando tanto su rendimiento como su estabilidad bajo condiciones de operación.

Metodología

Las estructuras químicas de los materiales de transporte utilizados para fabricar los dispositivos se presentan en la **Fig. 15**. Se Seleccionó TaTm como HTM por su fácil procesabilidad en vacío y su tendencia a formar capas completamente amorfas. El fullereno C_{60} se seleccionó como la molécula de transporte de electrones, ya que también es fácil de sublimar y es un aceptor de electrones eficiente para las perovskitas.[40] El dopaje de la HTL se realizó mediante la evaporación simultánea de las moléculas F_6-TCNNQ y TaTm con una concentración de F_6-TCNNQ de 11% en peso. De manera similar, la capa de C_{60} se dopó por evaporación simultánea con la molécula de PhIm a una concentración de 30% en peso.

Se prepararon y evaluaron cinco tipos diferentes de dispositivos, mostrados en la **Fig. 16**, nombrados de la A a la E. La referencia es el dispositivo A, en el que se usaron tanto HTL y ETL, ambas dopadas. En el dispositivo B, se eliminó la HTL dopada para que la capa de TaTm estuviese en contacto directo con el electrodo de ITO. El dispositivo C imita la estructura del dispositivo B, pero con una capa delgada de F_6-TCNNQ depositada entre el ITO y el TaTm. En los dispositivos D y E, la configuración del contacto de tipo p fue la misma que en los dispositivos A y C, mientras que la capa dopada de C_{60} se sustituyó por una película delgada de BCP. Este tipo de ETL (C_{60}/BCP/Ag) ha sido ampliamente utilizado en células solares orgánicas,[75] y posteriormente se ha adoptado en las células solares de perovskita.[76] El espesor de cada capa se especifica en la **Fig. 16**.

La estabilidad de las células solares se investigó mediante exposición continua a luz LED blanca (espectro en la **Fig. 17a**). La intensidad de la luz se ajustó hasta alcanzar el valor de J_{SC} obtenido bajo iluminación AM 1.5G. La temperatura de las células durante la prueba alcanzó aproximadamente los 40 °C en los primeros 10 minutos, manteniéndose constante durante el resto del experimento. Las células se mantuvieron en condiciones de cortocircuito sin encapsulación dentro de una caja de guantes con atmósfera de nitrógeno. A intervalos de tiempo fijos, se medían curvas *J-V* de las cuales pueden extraerse la evolución de los parámetros característicos de las células solares. Este tipo de medición permite determinar qué parámetro está encabezando la degradación de la eficiencia energética, lo que permite postular posibles mecanismos de degradación.

Resultados

Las cinco configuraciones de los diferentes dispositivos se caracterizaron bajo iluminación solar simulando el espectro AM 1.5G. Las curvas *J-V* para el dispositivo de referencia A y para los dispositivos B y C se representan en la **Fig. 18a**. El dispositivo de referencia A funciona de acuerdo con las publicaciones anteriores,[30] alcanzando una eficiencia del 16.2% con una J_{SC} de 20.7 mA cm^{-2}, un V_{OC} de 1.08 V y un FF del 72%. En el dispositivo B, cuando se elimina la HTL dopada, la curva *J-V* presenta un FF muy bajo con una pronunciada resistencia en serie, lo cual nos indica que la extracción/inyección de cargas está obstaculizada. El origen de este efecto debe proceder de la interfaz ITO/TaTm, ya que es la única variación entre los dispositivos A y B. La diferencia energética de 0.6 eV entre la función de trabajo del ITO (4.8 eV) y el HOMO del TaTm (5.4 eV), se traduce en una barrera de energía que limita la extracción e inyección de cargas.[46] Para reducir dicha barrera, se depositó una capa delgada (2.5 nm) de F_6-TCNNQ encima del ITO antes de la deposición de la capa de TaTm (dispositivo C). Como se puede ver en la **Fig. 18a**, la curva *J-V* de este nuevo dispositivo muestra una buena rectificación, con un FF que alcanza el 79%. Además, la curva *J-V* en oscuridad para el dispositivo C muestra una densidad de corriente similar a la del dispositivo A. Esto demuestra que la barrera de extracción se ha eliminado. Conjuntamente, la J_{SC} en el dispositivo C aumenta significativamente respecto a la referencia. El origen de este efecto puede entenderse al comparar los espectros EQE de los diferentes dispositivos (**Fig. 19a**), donde se observa que el dispositivo C tiene una respuesta espectral mayor en la región azul-verde del espectro electromagnético. La respuesta espectral en esta región está influenciada fuertemente por la absorción parasítica de los materiales de transporte dopados típicos, como se mencionó anteriormente. En la **Fig. 19b** se representa la absorción de los dos tipos de HTL empleadas en los dispositivos A y C. Se observa una disminución sustancial en el espectro de absorción para la HTL del dispositivo C en comparación con la del dispositivo de referencia A. La reducción en la parte visible del espectro se debe principalmente a la ausencia de la banda de absorción alrededor de 500 nm (banda debida al dopaje). Aunque es probable que en la interfaz entre el F_6-TCNNQ y el TaTm una pequeña fracción de las moléculas de TaTm se oxiden, esto no conduce a una absorbancia significativa. Esta reducción en la absorción parasítica hace que llegue más luz a la perovskita, lo que explica el aumento de la J_{SC} para esta configuración.

Los dispositivos D y E tienen J_{SC} y V_{OC} similares a los de los dispositivos A y C, respectivamente (**Fig. 20** y **Tabla 1**). Las densidades de corriente parecidas son esperables, ya que los contactos frontales no varían y el efecto de la capa de transporte de cargas superior sobre la absorción óptica es pequeño. Es notable destacar que la ETL C_{60}/BCP produce diodos con una alta rectificación, comparables a los fabricados con la capa C_{60}/C_{60}:PhIm, mucho más conductora, ambos con un alto FF.

La evolución de los parámetros fotovoltaicos a lo largo del tiempo se representa en la **Fig. 21**. Podemos distinguir dos tipos de comportamiento para los diferentes dispositivos. Los dispositivos D y E, ambos con el contacto superior C_{60}/BCP/Ag, son estables durante más de 280 horas bajo iluminación, con tan solo una disminución relativa del ± 10% en el PCE. Esta reducción se debe principalmente a una caída en la J_{SC}. En contraste, el V_{OC} aumenta ligeramente durante las primeras 100 horas, un efecto que puede estar relacionado con la pasivación de las trampas electrónicas en la capa de perovskita por efecto de la iluminación, como se ha reportado anteriormente.[82] Por otro lado, los dispositivos A y C muestran un comportamiento muy diferente, al emplear como contacto superior C_{60}/C_{60}:PhIm. Estos dispositivos son menos estables, observándose una reducción hasta el 80% del valor inicial del PCE después de aproximadamente 100 horas de funcionamiento. La degradación en estos dispositivos afecta a todos los parámetros y especialmente a la J_{SC} y el FF, que disminuyen más rápido que en los dispositivos con ETL intrínsecas (D y E). Estos resultados indican que el deterioro de estas células solares está relacionado con un aumento de la resistencia en serie, probablemente debido a la degradación de la capa ETL dopada, ya que esta solo está protegida por el electrodo metálicos. La degradación del material dopado introduciría una barrera de extracción en la interfaz con el metal, causando una disminución en el FF y en la densidad de corriente de acuerdo con nuestras observaciones.

(RuCp*mes)$_2$ como un dopante sublimable de tipo-n para células solares de perovskita con arquitectura n–i–p

Introducción

Las células solares de perovskita más eficientes reportadas hasta el momento tienen en común el uso de TiO_2 como material de transporte de electrones (ETM).[35,83] Estos dispositivos presentan una arquitectura de tipo n-i-p usando como ETM una capa de TiO_2 mesoporoso depositado sobre el óxido conductor transparente, generalmente FTO. Entre los materiales de transporte de electrones que se han estudiado en las células solares de perovskita destacan otros óxidos metálicos (SnO_2[84,85], ZnO[86] entre otros) y los semiconductores orgánicos.[87,88] En comparación con sus homólogos inorgánicos, los materiales de transporte de electrones orgánicos presentan algunas ventajas, como una fácil modelación de las propiedades optoelectrónicas mediante modificación química, deposición en capa delgada, procesamiento simple y a baja temperatura, y una buena reproducibilidad entre lotes.[89] Entre estos materiales, PCBM y C_{60} se han utilizado ampliamente como ETM en células solares de perovskita. En particular, el empaquetamiento en estado sólido del C_{60} presenta una alta densidad lo que facilita el transporte de cargas, aumentando la movilidad de electrones en comparación con los fullerenos modificados químicamente. Además, el C_{60} es un material relativamente barato y puede procesarse en capa fina por sublimación al vacío. Dadas estas propiedades, C_{60} es ampliamente adoptado como ETM en células solares de perovskita con alta eficiencia.[30,94,95]

El uso de dopantes de tipo-n para el fullereno en las células solares de perovskita generalmente aumenta la eficiencia en comparación con los dispositivos que usan C_{60} intrínseco como ETL.[30,97–101] Un tipo de compuesto usado para este propósito consiste en dímeros organometálicos tipo-sándwich de 19 electrones (así como aquellos formados por radicales orgánicos),[102] los cuales combinan una fuerte capacidad reductora, una reactividad limpia (formando únicamente los cationes monoméricos que producen el dopaje) y una estabilidad moderada al aire, mientras que son procesables tanto desde disolución como en vacío. En vista de estas excelentes propiedades, se han utilizado para dopar una gran variedad de semiconductores, incluidos los fullerenos.[102–105] En este capítulo, describimos el uso de un compuesto organometálico de este tipo, el pentamethylcyclopentadienyl mesitylene ruthenium dimer $(RuCp^*mes)_2$,[107] para dopar C_{60} en células solares de perovskita de tipo n-i-p depositadas en vacío.

Metodología

Las estructuras químicas de los semiconductores orgánicos utilizados para la fabricación de los dispositivos se presentan en la **Fig. 22**. El dímero $(RuCp^*mes)_2$ fue sintetizado por colaboradores del Instituto de Tecnología de Georgia siguiendo protocolos publicados anteriormente.[48] Para evaluar la reactividad entre el dopante $(RuCp^*mes)_2$ y el C_{60} se siguieron dos enfoques diferentes. En uno, ambos materiales se sublimaron simultáneamente dando lugar a una capa homogénea de C_{60}:$(RuCp^*mes)_2$ con un espesor de 20 nm. En el otro enfoque, se depositó una bicapa formada por una película de $(RuCp^*mes)_2$ cubierta por C_{60} (10 nm). En este caso, el contacto y, por lo tanto, la reacción entre los materiales se produce principalmente en la interfaz entre ellos. La arquitectura de los dispositivos es una configuración de tipo n-i-p donde el ETL se deposita directamente sobre el electrodo frontal de vidrio/ITO. La estructura de los dispositivos es la siguiente: ITO/ETL/C_{60}/MAPI/TaTm/TaTm:F_6-TCNNQ/Au. El grosor de cada capa se especifica en la **Fig. 23**.

Resultados

En la **Fig. 24a** se presentan las curvas de densidad de corriente frente a voltaje de las células solares usando tres concentraciones de dopante deferentes para la capa de C_{60}:(RuCp*mes)$_2$ (2.5%, 6.25% y 12.5% en peso). El dispositivo que usa C_{60} con una concentración de dopante de 12.5% demuestra una excelente extracción de los electrones (el FF es de aproximadamente 79%) y un V_{OC} de 1.07 V. Teniendo en cuenta la J_{SC} de 19.2 mA cm^{-2}, los dispositivos presentan una eficiencia del 16.1% (estadística en la **Tabla 2**). Bajando la concentración de dopante a 6.25%, el dispositivo continúa mostrando una buena rectificación sin cambios significativos en el FF (80%) o el V_{OC} (1.07 V). Sin embargo, la J_{SC} aumenta ligeramente a 20.1 mA cm^{-2}, mejorando la PCE de la celda a 17.1%. Disminuir la concentración de dopante a 2.5% en peso causa la aparición de una pronunciada resistencia en serie en la curva. El bajo FF (FF = 58%) junto con un reducido V_{OC} nos indican que la capa C_{60}:(RuCp*mes)$_2$ a esta concentración de dopante no es capaz de reducir de manera efectiva la barrera de energía en la interfaz, produciéndose pérdidas por recombinación.

Se fabricó y analizó un segundo lote de dispositivos con una capa pura de (RuCp*mes)$_2$ depositada entre el ITO y el C_{60}. Como referencia se preparó un dispositivo adicional sin la capa intermedia de (RuCp*mes)$_2$, donde el C_{60} está directamente en contacto con ITO. Las curvas *J*–*V* pertenecientes a esta serie de dispositivos aparecen en la **Fig. 26a**. Las células solares de referencia con la interfaz ITO/C_{60} exhiben una mala rectificación, con bajos FF (23%) y V_{OC} (0.82 V). Cuando se introduce una capa fina de (RuCp*mes)$_2$ (1 nm) entre el electrodo de ITO y el C_{60}, se recupera el rendimiento óptimo del dispositivo, de nuevo con una buena rectificación (FF = 78%) y V_{OC} de 1.09 V. Teniendo en cuenta la densidad de corriente (J_{SC} = 20.1 mA cm^{-2}), se obtuvieron rendimientos sobre el 17%. Este rendimiento es similar al de las células solares usando C_{60} dopado, pero con una pequeña mejora en el V_{OC} (30 mV, los rendimiento de los dispositivos aparecen en la **Tabla 3** y la **Fig. 26a**). Este aumento en el V_{OC} nos indica que al evitar el uso de capas dopadas se reducen las pérdidas por recombinación no-radiativa. Sin embargo, si el grosor de la capa de $(RuCp^*mes)_2$ se incrementa ligeramente hasta los 2.5 nm, el dispositivo presenta una ineficiente extracción de cargas, de manera similar al dispositivo con solo C_{60} como ETL. Este comportamiento se debe a la baja movilidad de cargas del $(RuCp^*mes)_2$, que esencialmente bloquea la extracción de los electrones cuando es demasiado gruesa.

En la **Fig. 26b** podemos observar que los espectros EQE son muy similares para los dos tipos de dispositivos estudiados, con C_{60}:$(RuCp^*mes)_2$ y con la bicapa $(RuCp^*mes)_2/C_{60}$, con valores para el EQE de aproximadamente 0.8 en todo el rango espectral. Sin embargo, el dispositivo con C_{60} dopado exhibe una EQE ligeramente más baja en la región azul del espectro. Esta diferencia está relacionada con el grosor de la ETL, que en estos dispositivos es de 30 nm en total. Esto da como resultado una absorción parasítica mayor en comparación con la de la estructura en bicapa, donde se la capa de C_{60} tiene un espesor de tan solo 10 nm.

Células solares de perovskita tándems depositadas por sublimación

Introducción

El principio de funcionamiento de las células solares tipo tándem se basa en la combinación de dos o más absorbedores de luz que permiten recolectar fotones en una región amplia del espectro solar, reduciendo las pérdidas de termalización intrínsecas de los dispositivos de unión simple.[42] Según el tipo de conexión eléctrica entre las subceldas, se clasifican en tándems de dos terminales o de cuatro terminales. Una celda solar tándem de cuatro terminales está constituido por dos celdas independientes que están conectadas externamente en paralelo. En un dispositivo de dos terminales, las subceldas están fabricadas y conectadas monolíticamente una encima de la otra, lo que requiere una capa de recombinación o una unión de túnel para lograr un flujo de corriente óhmica. En este tipo de dispositivo, las subceldas están conectadas en serie y la corriente es idealmente la misma, mientras que sus voltajes se suman. Como resultado, se pueden desarrollar dispositivos con una menor densidad de corriente, pero con un voltaje más alto, alcanzando altas eficiencia. Además, la menor densidad de corriente conlleva menos pérdidas relacionadas con la resistencia en serie en los contactos, lo que permite fabricar células solares de mayor superficie.[110] Asimismo, el alto voltaje intrínseco de estos sistemas es interesante *per se* para aplicaciones en fotocatálisis, como la producción de hidrógeno mediante electrólisis del agua,[111] y la producción de hidrocarburos por reducción de dióxido de carbono.[112]

Las perovskitas son excelentes candidatos para dispositivos en tándem debido a sus favorables propiedades optoelectrónicas y su fácil procesamiento.[119] La capacidad de ajustar el "bandgap" (separación de energía entre la banda de conducción y valencia) de las perovskitas ha permitido la fabricación de tándems de perovskita-perovskita con eficiencias de 24.8%.[122–124] La eficiencia de las células solares en tándem de perovskita está principalmente limitada por un déficit en el V_{OC} de la perovskita de "bandgap" ancho y las pérdidas ópticas causadas por la unión de recombinación.[42,119]

Es también interesante examinar el potencial de células solares tándem utilizando el mismo semiconductor, en nuestro caso $CH_3NH_3PbI_3$, en ambas subceldas. Por ello, es necesario desarrollar un modelo óptico que tenga en cuenta la absorción de la luz y la distribución del campo eléctrico en las diferentes capas.[129,130] Las técnicas de procesado en vacío ofrecen un control de deposición a nivel nanométrico, tanto para la perovskita como para las capas de transporte.[131–133] La deposición se realiza a temperatura ambiente y se pueden preparar arquitecturas complejas minimizando la resistencia en serie y manteniendo una alta transparencia.[30] Aunque el uso del mismo absorbedor en ambas subceldas no reduce las pérdidas por termalización, conserva las ventajas mencionadas anteriormente de alto voltaje y baja densidad de corriente. Además, las capas de recombinación de carga desarrolladas se pueden aplicar directamente a otros tipos de células tándems.

Metodología

La absorción de luz en cada subcelda se optimizó mediante un modelo óptico. El modelo hace uso de las constantes ópticas de los diferentes materiales empleados en los dispositivos y optimiza el grosor de cada capa para minimizar todo lo posible la diferencia de absorción entre las subceldas. La **Tabla 4** resume los resultados del modelo, indicando el grosor óptimo para cada capa. Las pequeñas desviaciones entre los valores óptimos calculados y los valores experimentales se deben a la necesidad de mantener el grosor de las capas intrínsecas de transporte de cargas lo más bajo posible, para compensar su baja movilidad de cargas. Basándonos en este diseño, se prepararon células solares tándem $CH_3NH_3PbI_3$-$CH_3NH_3PbI_3$ con la estructura representada en la **Fig. 27**. Se prepararon también dispositivos de unión simple como referencias, imitando la estructura de cada una de las subceldas. Específicamente, la estructura de la subcelda frontal es ITO/TiO_2/C_{60}/$CH_3NH_3PbI_3$/TaTm/TaTm:F_6-TCNNQ/Au, mientras que la de la subcelda posterior es ITO/C_{60}:PhIm/C_{60}/ $CH_3NH_3PbI_3$/TaTm/TaTm:F_6-TCNNQ/Au (**Fig. 27**).

Resultados

Los materiales y estructuras usadas en las subceldas del tándem derivan de trabajos anteriores con los que se logró una alta eficiencia (PCE> 18%).[30,71] La subcelda frontal emplea como capa selectiva de electrones una capa de TiO_2 procesada por disolución. (**Fig. 27**) Esta configuración se seleccionó porque produce uno de los V_{OC} más altos entre las células solares de $CH_3NH_3PbI_3$ (1.17 V).[71] La subcelda trasera utiliza en su lugar C_{60}:PhIm/C_{60} como capa de transporte de electrones.[30] Esta ETL se prepara por evaporación, lo que permite su deposición directa sobre la subcelda frontal. La capa de recombinación de cargas está constituida por las capas dopadas TaTm:F_6-TCNNQ y C_{60}:PhIm. La conexión de ambos materiales dopados garantiza un contacto óhmico adecuado, con alta conductividad eléctrica y baja absorción óptica.[134] El grosor de la perovskita varía en cada subcelda, siendo de 95 nm para la subcelda frontal y de 420 nm para la trasera (**Tabla 4**). Como ambas perovskitas absorben en la misma región espectral, se necesita una capa delgada de perovskita en la subcelda frontal para permitir que suficiente luz se transmita a la subcelda trasera (**Fig. 28**). Los resultados de la simulación indicaron que la subcelda frontal generaría 10,35 mA cm^{-2} mientras que la subcelda trasera 10,21 mA cm^{-2}, con una diferencia entre las corrientes de tan solo 0,14 mA cm^{-2}.

En las gráficas de EQE (**Fig. 29**) se aprecian diferencias espectrales en la generación de cargas en cada subcelda. Se observa que la subcelda frontal genera corriente principalmente en la región azul del espectro, mientras que la subcelda trasera alcanza el máximo de generación de cargas a 700 nm. En consecuencia, en el dispositivo tándem hay una generación de cargas homogénea en todo el rango espectral.

Las curvas de corriente versus voltaje (*J-V*) del tándem y las celdas de referencia de unión simple se representan en la **Fig. 30**. Ambas celdas de referencia muestran un alto rendimiento. El FF mayor que 80% nos indica que el transporte de cargas es bueno y la barrera de extracción en los contactos es baja o nula, en concordancia con los trabajos anteriores.[30,71] Notablemente, la celda frontal alcanza un V_{OC} de 1.19 V, indicando unas pérdidas no radiactivas muy reducidas, posiblemente relacionado con que al ser la capa de perovskita particularmente fina la recombinación en su interior se ve minimizada. Las densidades de corrientes de cortocircuito (J_{SC}) de las celdas frontal y trasera son de 12.5 y 18.7 mA cm^{-2} respectivamente. La celda frontal con una densidad de corriente de 12.5 mA cm^{-2} excede los 10.35 mA cm^{-2} calculados por el modelo para el tándem. Este exceso de corriente se debe a la reflexión por parte del electrodo metálico, sin embargo, en el caso del tándem la subcelda posterior absorbería la luz adicional y no se reflejaría. Por otro lado, la celda trasera también presenta una corriente más alta que la calculada (18.7 versus 10.21 mA cm^{-2}). Para imitar las condiciones de la subcelda en la configuración en tándem, la densidad de corriente se midió bajo iluminación filtrada. El filtro consistió en una muestra de vidrio/$CH_3NH_3PbI_3$ con el mismo grosor de perovskita utilizado en la celda frontal (línea naranja en la **Fig. 30**). Como consecuencia, la J_{SC} se reduce aproximadamente a la mitad, llegando a 7.52 mA cm^{-2}. La **Tabla 5** revisa las características de las células solares.

La curva *J-V* del dispositivo en tándem (**Fig. 30**) presenta un FF cercano al 80% con diferencias prácticamente nulas entre los barridos directo e inverso, lo que remarca la calidad de la capa de recombinación de carga. El V_{OC} alcanzó 2305 mV, aproximadamente la suma de los fotovoltaje de las celdas de referencia (solo 15 mV más bajo). El J_{SC} del tándem es ligeramente más alto que el medido para la celda posterior de referencia, llegando a 9.84 mA cm^{-2}, este valor se sitúa muy cerca del valor calculado por el modelo (10.16 mA cm^{-2}). Como resultado, el tándem logra una eficiencia de conversión de energía de 18.02%, excediendo la eficiencia de los dispositivos de unión simple.

También se estudió la vida útil de los tándems. Los dispositivos fueron medidos periódicamente transcurridos varios días después de la fabricación, y siguieron mostraron rendimientos similares sin la aparición de histéresis o un descenso significativo en los parámetros característicos. En la **Fig. 31a** aparece un dispositivo medido hasta 17 días después de su fabricación. La eficiencia se redujo solo del 16,72% al 16,55%.

Por otro lado, en la **Fig. 31b** presentamos un dispositivo tándem con un área activa de 0,36 cm^2, significativamente más grande que el estándar en nuestro laboratorio (0,04 cm^2). El dispositivo presenta características similares al tándem preparado en áreas pequeñas, alcanzando una eficiencia del 17.2%. Esta área aún está lejos de ser elegible para la certificación (1 cm^2),[137] sin embargo, un FF de 79% en una celda cuya área se ha multiplicado por 9, es un resultado muy prometedor para este tipo de tándems, permitiendo su futura aplicación en superficie grande.

Conclusiones

El trabajo de esta tesis ha sido estructurado en tres secciones. Después de la exposición y evaluación de los resultados obtenidos en cada capítulo, las conclusiones principales se describen a continuación.

En el capítulo 3, se estudió el rendimiento y la estabilidad de células solares tipo p–i–n de perovskita con y sin capa de transporte de cargas dopada. En el contacto p, el reemplazo de las capas de transporte de carga dopadas por alternativas no dopadas mejoró el rendimiento del dispositivo. En primer lugar, se identificó una barrera Schottky de inyección/extracción de carga en la interfaz ITO-TaTm. Mediante la inserción de una capa muy fina de la molécula de dopante tipo p entre el ITO y la HTL se consiguió aliviar dicha barrera. Esta estrategia da como resultado una reducción importante de la absorción parasítica. Esto conduce a una mejora de la respuesta espectral en la parte azul del espectro electromagnético y, por lo tanto, a un aumento en la densidad de corriente. La mejora en la estabilidad de la célula solar procede de la eliminación de las capas de transporte de electrones dopadas sobre la perovskita. Los dispositivos con la bicapa C_{60}/BCP presentaron rectificaciones comparables a los dispositivos que usaban la capa de PhIm:C_{60}/C_{60}, incluso siendo esta última mucho más conductora. Se ha demostrado el potencial del dopaje interfacial para preparar capas de transporte de cargas estables y transparentes, y para fabricar células solares muy eficientes y estables. Las estrategias identificadas aquí se pueden extrapolar a una gama más amplia de materiales de transporte y su aplicabilidad a diferentes células solares de perovskita y multiunión.

En el capítulo 4, hemos demostrado el uso de $(RuCp^*mes)_2$ como dopante tipo n para C_{60} en células solares de perovskita depositadas por sublimación. Se investigaron dos vías diferentes para dopar el C_{60} con $(RuCp^*mes)_2$, con el objetivo de usarlos como capas de transporte de electrones. El C_{60} evaporado simultáneamente con el dopante $(RuCp^*mes)_2$ forma películas homogéneas entre el ITO y el fullereno intrínseco, estableciendo contacto óhmico entre ellos. La optimización de la concentración de dopante permitió la fabricación de células solares con una eficiencia de conversión de energía cercana al 18%. En el caso de la bicapa $(RuCp^*mes)_2/C_{60}$, el grosor del $(RuCp^*mes)_2$ fue un parámetro crítico para obtener un dispositivo funcional. Solo cuando la capa de dopante era del orden de 1 nm, observamos una extracción de cargas óptima con eficiencias superiores al 17%. En general, se observó que las células solares que usan la bicapa $(RuCp^*mes)_2/C_{60}$ presentan V_{OC} más alto, como consecuencia de una recombinación no-radiativa menor en comparación con las células solares que usan las capas dopadas. Las ETL desarrolladas en este capítulo tienen el potencial de poder usarse también en células solares tipo p-i-n y en capas de recombinación de carga en tándems.

En el capítulo 5, hemos mostrado células solares tipo tándem que utilizan como absorbedor la misma perovskita ($CH_3NH_3PbI_3$– $CH_3NH_3PbI_3$), preparadas por deposición en vacío. Se utilizó un modelo óptico para calcular la configuración ideal del tándem, determinando con precisión nanométrica el grosor de cada capa. Las pequeñas diferencias entre la densidad de corriente del tándem y la calculada por el modelo, legitiman el uso de los parámetros obtenidas por el modelo teórico. El uso de la capa de recombinación de cargas basado en moléculas orgánicas se traduce en pérdidas de voltaje muy bajas, dando lugar a voltajes de circuito abierto relativamente altos. Las eficiencias de los dispositivos tándems alcanzaron valores similares a los dispositivos de unión simple (> 18%), pero con una densidad de corriente reducida y un voltaje de circuito abierto muy alto (2,3 V). Estos resultados validan el uso de procesos de sublimación para el desarrollo de arquitecturas complejas para dispositivos de perovskita como los tándems.

Bibliography

1. Adams, W. G. & Day, R. E. V. The action of light on selenium. *Proc. R. Soc. London* **25**, 113–117 (1877).
2. Shafiee, S. & Topal, E. When will fossil fuel reserves be diminished? *Energy Policy* **37**, 181–189 (2009).
3. Fraunhofer, I. S. E. Photovoltaics Report. https://www.webcitation.org/6SFRTUaBS?url=http://www.ise.fraunhofer.de/en/downloads-englisch/pdf-files-englisch/photovoltaics-report-slides.pdf (2016).
4. NREL. Best Research-Cell Efficiencies. *National Renewable Energy Laboratory* https://www.nrel.gov/pv/assets/images/efficiency-chart.png.
5. Li, C. *et al.* Formability of {\it ABX}${\sb 3}$ ({\it X} = F, Cl, Br, I) halide perovskites. *Acta Crystallogr. Sect. B* **64**, 702–707 (2008).
6. Filip, M. R., Eperon, G. E., Snaith, H. J. & Giustino, F. Steric engineering of metal-halide perovskites with tunable optical band gaps. *Nat. Commun.* **5**, 5757 (2014).
7. Kieslich, G., Sun, S. & Cheetham, A. K. Solid-state principles applied to organic–inorganic perovskites: new tricks for an old dog. *Chem. Sci.* **5**, 4712–4715 (2014).
8. Wang, C., Song, Z., Li, C., Zhao, D. & Yan, Y. Low-Bandgap Mixed Tin-Lead Perovskites and Their Applications in All-Perovskite Tandem Solar Cells. *Adv. Funct. Mater.* **29**, 1808801 (2019).
9. Green, M. A., Ho-Baillie, A. & Snaith, H. J. The emergence of perovskite solar cells. *Nat. Photonics* **8**, 506–514 (2014).
10. Yin, W.-J., Shi, T. & Yan, Y. Unique Properties of Halide Perovskites as Possible Origins of the Superior Solar Cell Performance. *Adv. Mater.* **26**, 4653–4658 (2014).
11. Yin, W.-J., Shi, T. & Yan, Y. Unusual defect physics in CH3NH3PbI3 perovskite solar cell absorber. *Appl. Phys. Lett.* **104**, 63903 (2014).
12. Sun, S. *et al.* The origin of high efficiency in low-temperature solution-processable bilayer organometal halide hybrid solar cells. *Energy Environ. Sci.* **7**,

399–407 (2014).

13. Aharon, S., Gamliel, S., Cohen, B. El & Etgar, L. Depletion region effect of highly efficient hole conductor free CH3NH3PbI3 perovskite solar cells. *Phys. Chem. Chem. Phys.* **16**, 10512–10518 (2014).
14. Schulz, P. *et al.* Interface energetics in organo-metal halide perovskite-based photovoltaic cells. *Energy Environ. Sci.* **7**, 1377–1381 (2014).
15. De Wolf, S. *et al.* Organometallic Halide Perovskites: Sharp Optical Absorption Edge and Its Relation to Photovoltaic Performance. *J. Phys. Chem. Lett.* **5**, 1035–1039 (2014).
16. Ponseca, C. S. *et al.* Organometal Halide Perovskite Solar Cell Materials Rationalized: Ultrafast Charge Generation, High and Microsecond-Long Balanced Mobilities, and Slow Recombination. *J. Am. Chem. Soc.* **136**, 5189–5192 (2014).
17. Lin, Q. *et al.* Electro-optics of perovskite solar cells. *Nat. Photonics* **9**, 106–112 (2015).
18. D'Innocenzo, V. *et al.* Excitons versus free charges in organo-lead tri-halide perovskites. *Nat. Commun.* **5**, 3586 (2014).
19. Stoumpos, C. C., Malliakas, C. D. & Kanatzidis, M. G. Semiconducting Tin and Lead Iodide Perovskites with Organic Cations: Phase Transitions, High Mobilities, and Near-Infrared Photoluminescent Properties. *Inorg. Chem.* **52**, 9019–9038 (2013).
20. Herz, L. M. Charge-Carrier Mobilities in Metal Halide Perovskites: Fundamental Mechanisms and Limits. *ACS Energy Lett.* **2**, 1539–1548 (2017).
21. Coropceanu, V. *et al.* Charge Transport in Organic Semiconductors. *Chem. Rev.* **107**, 926–952 (2007).
22. Xing, G. *et al.* Long-Range Balanced Electron- and Hole-Transport Lengths in Organic-Inorganic CH3NH3PbI3. *Science (80-.).* **342**, 344–347 (2013).
23. Stranks, S. D. *et al.* Electron-Hole Diffusion Lengths Exceeding 1 Micrometer in an Organometal Trihalide Perovskite Absorber. *Science (80-.).* **342**, 341–344 (2013).
24. Gonzalez-Pedro, V. *et al.* General Working Principles of CH3NH3PbX3 Perovskite Solar Cells. *Nano Lett.* **14**, 888–893 (2014).

25. Dong, Q. *et al.* Electron-hole diffusion lengths > 175 µm in solution-grown CH3NH3PbI3 single crystals. *Science (80-.).* **347**, 967–970 (2015).

26. Shi, D. *et al.* Low trap-state density and long carrier diffusion in organolead trihalide perovskite single crystals. *Science (80-.).* **347**, 519–522 (2015).

27. Ávila, J., Momblona, C., Boix, P. P., Sessolo, M. & Bolink, H. J. Vapor-Deposited Perovskites: The Route to High-Performance Solar Cell Production? *Joule* **1**, 431–442 (2017).

28. Liu, M., Johnston, M. B. & Snaith, H. J. Efficient planar heterojunction perovskite solar cells by vapour deposition. *Nature* **501**, 395–398 (2013).

29. Malinkiewicz, O. *et al.* Perovskite solar cells employing organic charge-transport layers. *Nat. Photonics* **8**, 128–132 (2014).

30. Momblona, C. *et al.* Efficient vacuum deposited p-i-n and n-i-p perovskite solar cells employing doped charge transport layers. *Energy Environ. Sci.* **9**, 3456–3463 (2016).

31. Palazon, F. *et al.* Room-Temperature Cubic Phase Crystallization and High Stability of Vacuum-Deposited Methylammonium Lead Triiodide Thin Films for High-Efficiency Solar Cells. *Adv. Mater.* **31**, 1902692 (2019).

32. Lohmann, K. B. *et al.* Control over Crystal Size in Vapor Deposited Metal-Halide Perovskite Films. *ACS Energy Lett.* **5**, 710–717 (2020).

33. Borchert, J. *et al.* Impurity Tracking Enables Enhanced Control and Reproducibility of Hybrid Perovskite Vapor Deposition. *ACS Appl. Mater. Interfaces* **11**, 28851–28857 (2019).

34. Parrott, E. S. *et al.* Growth modes and quantum confinement in ultrathin vapour-deposited MAPbI3 films. *Nanoscale* **11**, 14276–14284 (2019).

35. Jung, E. H. *et al.* Efficient, stable and scalable perovskite solar cells using poly(3-hexylthiophene). *Nature* **567**, 511–515 (2019).

36. Li, H. *et al.* Carbon Quantum Dots/TiOx Electron Transport Layer Boosts Efficiency of Planar Heterojunction Perovskite Solar Cells to 19%. *Nano Lett.* **17**, 2328–2335 (2017).

37. Nie, W. *et al.* High-efficiency solution-processed perovskite solar cells with millimeter-scale grains. *Science (80-.).* **347**, 522–525 (2015).

38. You, J. *et al.* Improved air stability of perovskite solar cells via solution-processed

metal oxide transport layers. *Nat. Nanotechnol.* **11**, 75–81 (2016).

39. Park, J. H. *et al.* Efficient CH3NH3PbI3 Perovskite Solar Cells Employing Nanostructured p-Type NiO Electrode Formed by a Pulsed Laser Deposition. *Adv. Mater.* **27**, 4013–4019 (2015).

40. Liang, P.-W., Chueh, C.-C., Williams, S. T. & Jen, A. K.-Y. Roles of Fullerene-Based Interlayers in Enhancing the Performance of Organometal Perovskite Thin-Film Solar Cells. *Adv. Energy Mater.* **5**, 1402321 (2015).

41. Shockley, W. & Queisser, H. J. Detailed Balance Limit of Efficiency of p-n Junction Solar Cells. *J. Appl. Phys.* **32**, 510–519 (1961).

42. Anaya, M., Lozano, G., Calvo, M. E. & Míguez, H. ABX3 Perovskites for Tandem Solar Cells. *Joule* **1**, 769–793 (2017).

43. Stolterfoht, M. *et al.* Visualization and suppression of interfacial recombination for high-efficiency large-area pin perovskite solar cells. *Nat. Energy* **3**, 847–854 (2018).

44. Marinova, N. *et al.* Light Harvesting and Charge Recombination in CH3NH3PbI3 Perovskite Solar Cells Studied by Hole Transport Layer Thickness Variation. *ACS Nano* **9**, 4200–4209 (2015).

45. Stolterfoht, M. *et al.* Approaching the fill factor Shockley–Queisser limit in stable{,} dopant-free triple cation perovskite solar cells. *Energy Environ. Sci.* **10**, 1530–1539 (2017).

46. Lee, J.-H. & Kim, J.-J. Interfacial Doping for Efficient Charge Injection in Organic Semiconductors. in *Physics of Organic Semiconductors* 91–118 (John Wiley & Sons, Ltd, 2013). doi:10.1002/9783527654949.ch4.

47. Schloemer, T. H., Christians, J. A., Luther, J. M. & Sellinger, A. Doping strategies for small molecule organic hole-transport materials: impacts on perovskite solar cell performance and stability. *Chem. Sci.* **10**, 1904–1935 (2019).

48. Un, H.-I. *et al.* Understanding the Effects of Molecular Dopant on n-Type Organic Thermoelectric Properties. *Adv. Energy Mater.* **9**, 1900817 (2019).

49. Niederberger, M. Nonaqueous Sol–Gel Routes to Metal Oxide Nanoparticles. *Acc. Chem. Res.* **40**, 793–800 (2007).

50. Hadipour, A. WO2017108710 - DOPED TITANATE. (2017).

51. Gueymard, C. A., Myers, D. & Emery, K. Proposed reference irradiance spectra

for solar energy systems testing. *Sol. Energy* **73**, 443–467 (2002).

52. Zuo, C. *et al.* Advances in Perovskite Solar Cells. *Adv. Sci.* **3**, 1500324 (2016).
53. Honsberg, C. B., Bremner, S. P. & Corkish, R. Design trade-offs and rules for multiple energy level solar cells. *Phys. E Low-dimensional Syst. Nanostructures* **14**, 136–141 (2002).
54. Walzer, K., Maennig, B., Pfeiffer, M. & Leo, K. Highly Efficient Organic Devices Based on Electrically Doped Transport Layers. *Chem. Rev.* **107**, 1233–1271 (2007).
55. Alnuaimi, A., Almansouri, I. & Nayfeh, A. Effect of Mobility and Band Structure of Hole Transport Layer in Planar Heterojunction Perovskite Solar Cells Using 2D TCAD Simulation. *J. Comput. Electron.* **15**, 1110–1118 (2016).
56. Habisreutinger, S. N., McMeekin, D. P., Snaith, H. J. & Nicholas, R. J. Research Update: Strategies for improving the stability of perovskite solar cells. *APL Mater.* **4**, 91503 (2016).
57. Bi, D. *et al.* Polymer-templated nucleation and crystal growth of perovskite films for solar cells with efficiency greater than 21%. *Nat. Energy* **1**, 16142 (2016).
58. Burschka, J. *et al.* Sequential deposition as a route to high-performance perovskite-sensitized solar cells. *Nature* **499**, 316–9 (2013).
59. Green, M. A. *et al.* Solar cell efficiency tables (Version 53). *Prog. Photovoltaics Res. Appl.* **27**, 3–12 (2019).
60. Rong, Y., Liu, L., Mei, A., Li, X. & Han, H. Beyond Efficiency: the Challenge of Stability in Mesoscopic Perovskite Solar Cells. *Adv. Energy Mater.* **5**, 1501066 (2015).
61. Yang, W. S. *et al.* Iodide management in formamidinium-lead-halide{\textendash}based perovskite layers for efficient solar cells. *Science (80-.).* **356**, 1376–1379 (2017).
62. Jeon, N. J. *et al.* Compositional engineering of perovskite materials for high-performance solar cells. *Nature* **517**, 476–480 (2015).
63. Yang, W. S. *et al.* High-performance photovoltaic perovskite layers fabricated through intramolecular exchange. *Science (80-.).* **348**, 1234–1237 (2015).
64. Jeon, N. J. *et al.* Solvent engineering for high-performance inorganic–organic hybrid perovskite solar cells. *Nat. Mater.* **13**, 897–903 (2014).

65. Ko, Y., Kim, Y., Lee, C., Kim, Y. & Jun, Y. Investigation of Hole-Transporting Poly(triarylamine) on Aggregation and Charge Transport for Hysteresisless Scalable Planar Perovskite Solar Cells. *ACS Appl. Mater. Interfaces* **10**, 11633–11641 (2018).
66. Dongxue, L. & Liu, Y. Recent progress of dopant-free organic hole-transporting materials in perovskite solar cells. *J. Semicond.* **38**, 011005 (2017).
67. Jung, M.-C., Raga, S. R., Ono, L. K. & Qi, Y. Substantial improvement of perovskite solar cells stability by pinhole-free hole transport layer with doping engineering. *Sci. Rep.* **5**, 9863 (2015).
68. Pérez-del-Rey, D. *et al.* Molecular Passivation of MoO3: Band Alignment and Protection of Charge Transport Layers in Vacuum-Deposited Perovskite Solar Cells. *Chem. Mater.* **31**, 6945–6949 (2019).
69. Pham, H. D. *et al.* Organic interfacial materials for perovskite-based optoelectronic devices. *Energy Environ. Sci.* **12**, 1177–1209 (2019).
70. Gil-Escrig, L. *et al.* Vacuum Deposited Triple-Cation Mixed-Halide Perovskite Solar Cells. *Adv. Energy Mater.* **8**, 1703506 (2018).
71. Pérez-Del-Rey, D., Boix, P. P., Sessolo, M., Hadipour, A. & Bolink, H. J. Interfacial Modification for High-Efficiency Vapor-Phase-Deposited Perovskite Solar Cells Based on a Metal Oxide Buffer Layer. *J. Phys. Chem. Lett.* **9**, 1041–1046 (2018).
72. Correa-Baena, J.-P. *et al.* Identifying and suppressing interfacial recombination to achieve high open-circuit voltage in perovskite solar cells. *Energy Environ. Sci.* **10**, 1207–1212 (2017).
73. Dapperheld, S., Steckhan, E., Brinkhaus, K.-H. G. & Esch, T. Organic Electron Transfer Systems, II Substituted Triarylamine Cation-Radical Redox Systems – Synthesis, Electrochemical and Spectroscopic Properties, Hammet Behavior, and Suitability as Redox Catalysts. *Chem. Ber.* **124**, 2557–2567 (1991).
74. Dänekamp, B. *et al.* Influence of hole transport material ionization energy on the performance of perovskite solar cells. *J. Mater. Chem. C* **7**, 523–527 (2019).
75. Peumans, P., Bulović, V. & Forrest, S. R. Efficient photon harvesting at high optical intensities in ultrathin organic double-heterostructure photovoltaic diodes. *Appl. Phys. Lett.* **76**, 2650–2652 (2000).
76. Xiao, Z. *et al.* Efficient{,} high yield perovskite photovoltaic devices grown by

interdiffusion of solution-processed precursor stacking layers. *Energy Environ. Sci.* **7**, 2619–2623 (2014).

77. Tokito, S., Noda, K. & Taga, Y. Metal oxides as a hole-injecting layer for an organic electroluminescent device. *J. Phys. D. Appl. Phys.* **29**, 2750–2753 (1996).
78. Liao, L. S., Slusarek, W. K., Hatwar, T. K., Ricks, M. L. & Comfort, D. L. Tandem Organic Light-Emitting Diode using Hexaazatriphenylene Hexacarbonitrile in the Intermediate Connector. *Adv. Mater.* **20**, 324–329 (2008).
79. Wang, X. *et al.* Highly efficient charge generation and electron injection of m-MTDATA/m-MTDATA:HAT-CN/HAT-CN organic heterojunction on ITO cathode for high efficiency inverted white organic light-emitting diodes. *J. Appl. Phys.* **122**, (2017).
80. Ma, Y. *et al.* Improved Hole-Transporting Property via HAT-CN for Perovskite Solar Cells without Lithium Salts. *ACS Appl. Mater. Interfaces* **7**, 6406–6411 (2015).
81. Qin, P. *et al.* Transition metal oxides as hole-transporting materials in organic semiconductor and hybrid perovskite based solar cells. *Sci. China Chem.* **60**, 472–489 (2017).
82. Brenes, R. *et al.* Metal Halide Perovskite Polycrystalline Films Exhibiting Properties of Single Crystals. *Joule* **1**, 155–167 (2017).
83. Yang, W. S. *et al.* Iodide management in formamidinium-lead-halide-based perovskite layers for efficient solar cells. *Science (80-.).* **356**, 1376–1379 (2017).
84. Jiang, Q. *et al.* Enhanced electron extraction using SnO2 for high-efficiency planar-structure HC(NH2)2PbI3-based perovskite solar cells. *Nat. Energy* **2**, 16177 (2016).
85. Etgar, L. *et al.* Mesoscopic CH3NH3PbI3/TiO2 Heterojunction Solar Cells. *J. Am. Chem. Soc.* **134**, 17396–17399 (2012).
86. Liu, D. & Kelly, T. L. Perovskite solar cells with a planar heterojunction structure prepared using room-temperature solution processing techniques. *Nat. Photonics* **8**, 133–138 (2014).
87. Zhao, D., Zhu, Z., Kuo, M. Y., Chueh, C. C. & Jen, A. K. Y. Hexaazatrinaphthylene Derivatives: Efficient Electron-Transporting Materials with Tunable Energy Levels for Inverted Perovskite Solar Cells. *Angew. Chemie - Int. Ed.* **55**, 8999–

9003 (2016).

88. Zhu, Z. *et al.* A Low-Temperature, Solution-Processable Organic Electron-Transporting Layer Based on Planar Coronene for High-performance Conventional Perovskite Solar Cells. *Adv. Mater.* **28**, 10786–10793 (2016).
89. Zhang, H. *et al.* New generation perovskite solar cells with solution-processed amino-substituted perylene diimide derivative as electron-transport layer. *J. Mater. Chem. A* **4**, 8724–8733 (2016).
90. Shao, Y., Xiao, Z., Bi, C., Yuan, Y. & Huang, J. Origin and elimination of photocurrent hysteresis by fullerene passivation in CH3NH3PbI3 planar heterojunction solar cells. *Nat. Commun.* **5**, 1–7 (2014).
91. Wojciechowski, K. *et al.* Cross-Linkable Fullerene Derivatives for Solution-Processed n-i-p Perovskite Solar Cells. *ACS Energy Lett.* **1**, 648–653 (2016).
92. McMeekin, D. P. *et al.* Crystallization Kinetics and Morphology Control of Formamidinium–Cesium Mixed-Cation Lead Mixed-Halide Perovskite via Tunability of the Colloidal Precursor Solution. *Adv. Mater.* **29**, (2017).
93. Patel, J. B. *et al.* Influence of Interface Morphology on Hysteresis in Vapor-Deposited Perovskite Solar Cells. *Adv. Electron. Mater.* **3**, 1–6 (2017).
94. Eze, V. O., Seike, Y. & Mori, T. Efficient planar perovskite solar cells using solution-processed amorphous WOx/fullerene C60as an electron extraction layers. *Org. Electron. physics, Mater. Appl.* **46**, 253–262 (2017).
95. Liu, D. *et al.* Impact of Ultrathin C60on Perovskite Photovoltaic Devices. *ACS Nano* **12**, 876–883 (2018).
96. Schwarze, M. *et al.* Molecular parameters responsible for thermally activated transport in doped organic semiconductors. *Nat. Mater.* (2019) doi:10.1038/s41563-018-0277-0.
97. Wang, Z. *et al.* Efficient and Air-Stable Mixed-Cation Lead Mixed-Halide Perovskite Solar Cells with n-Doped Organic Electron Extraction Layers. *Adv. Mater.* **29**, 1604186 (2017).
98. Song, S. *et al.* Surface modified fullerene electron transport layers for stable and reproducible flexible perovskite solar cells. *Nano Energy* **49**, 324–332 (2018).
99. Schwarze, M. *et al.* Analyzing the n-Doping Mechanism of an Air-Stable Small-Molecule Precursor. *ACS Appl. Mater. Interfaces* **10**, 1340–1346 (2018).

100. Naab, B. D. *et al.* Mechanistic Study on the Solution-Phase n-Doping of 1,3-Dimethyl-2-aryl-2,3-dihydro-1H-benzoimidazole Derivatives. *J. Am. Chem. Soc.* **135**, 15018–15025 (2013).

101. Weber, C. D., Bradley, C. & Lonergan, M. C. Solution phase n-doping of C60 and PCBM using tetrabutylammonium fluoride. *J. Mater. Chem. A* **2**, 303–307 (2014).

102. Naab, B. D. *et al.* Effective Solution- and Vacuum-Processed n-Doping by Dimers of Benzimidazoline Radicals. *Adv. Mater.* **26**, 4268–4272 (2014).

103. Guo, S. *et al.* n-Doping of Organic Electronic Materials using Air-Stable Organometallics. *Adv. Mater.* **24**, 699–703 (2012).

104. Olthof, S. *et al.* Ultralow Doping in Organic Semiconductors: Evidence of Trap Filling. *Phys. Rev. Lett.* **109**, 176601 (2012).

105. Smith, P. J. & Mann, C. K. Electrochemical dealkylation of aliphatic amines. *J. Org. Chem.* **34**, 1821–1826 (1969).

106. Pulvirenti, F. *et al.* Modification of the fluorinated tin oxide/electron-transporting material interface by a strong reductant and its effect on perovskite solar cell efficiency. *Mol. Syst. Des. Eng.* **3**, 741–747 (2018).

107. Gusev, O. V *et al.* Reduction of ruthenium arenecyclopentadienyl complexes reactions induced by electron transfer. *J. Organomet. Chem.* **534**, 57–66 (1997).

108. Guo, S. *et al.* n-Doping of Organic Electronic Materials Using Air-Stable Organometallics: A Mechanistic Study of Reduction by Dimeric Sandwich Compounds. *Chem. – A Eur. J.* **18**, 14760–14772 (2012).

109. Mohapatra, S. K. *et al.* Dimers of Nineteen-Electron Sandwich Compounds: Crystal and Electronic Structures, and Comparison of Reducing Strengths. *Chem. – A Eur. J.* **20**, 15385–15394 (2014).

110. Calnan, S. & Tiwari, A. N. High mobility transparent conducting oxides for thin film solar cells. *Thin Solid Films* **518**, 1839–1849 (2010).

111. Walter, M. G. *et al.* Solar Water Splitting Cells. *Chem. Rev.* **110**, 6446–6473 (2010).

112. Benson, E. E., Kubiak, C. P., Sathrum, A. J. & Smieja, J. M. Electrocatalytic and homogeneous approaches to conversion of CO2 to liquid fuels. *Chem. Soc. Rev.* **38**, 89–99 (2009).

113. Zhou, H. *et al.* Polymer Homo-Tandem Solar Cells with Best Efficiency of 11.3%.

Adv. Mater. **27**, 1767–1773 (2015).

114. You, J. *et al.* 10.2% Power Conversion Efficiency Polymer Tandem Solar Cells Consisting of Two Identical Sub-Cells. *Adv. Mater.* **25**, 3973–3978 (2013).
115. Kang, H. *et al.* Simplified Tandem Polymer Solar Cells with an Ideal Self-Organized Recombination Layer. *Adv. Mater.* **27**, 1408–1413 (2015).
116. Lu, S., Lin, H., Zhang, S., Hou, J. & Choy, W. C. H. A Switchable Interconnecting Layer for High Performance Tandem Organic Solar Cell. *Adv. Energy Mater.* **7**, 1701164 (2017).
117. Lu, S. *et al.* A New Interconnecting Layer of Metal Oxide/Dipole Layer/Metal Oxide for Efficient Tandem Organic Solar Cells. *Adv. Energy Mater.* **5**, 1500631 (2015).
118. Di Carlo Rasi, D. & Janssen, R. A. J. Advances in Solution-Processed Multijunction Organic Solar Cells. *Adv. Mater.* **31**, 1806499 (2019).
119. Chen, B., Zheng, X., Bai, Y., Padture, N. P. & Huang, J. Progress in Tandem Solar Cells Based on Hybrid Organic-Inorganic Perovskites. *Adv. Energy Mater.* 1602400 (2017) doi:10.1002/aenm.201602400.
120. Jaysankar, M. *et al.* Minimizing Voltage Loss in Wide-Bandgap Perovskites for Tandem Solar Cells. *ACS Energy Lett.* **4**, 259–264 (2019).
121. World record for tandem perovskite-CIGS solar cell. https://www.helmholtz-berlin.de/pubbin/news_seite?nid=20769;sprache=en;seitenid=75469.
122. Lin, R. *et al.* Monolithic all-perovskite tandem solar cells with 24.8% efficiency exploiting comproportionation to suppress Sn(ii) oxidation in precursor ink. *Nat. Energy* **4**, 864–873 (2019).
123. Eperon, G. E. *et al.* Perovskite-perovskite tandem photovoltaics with optimized band gaps. *Science (80-.).* **354**, 861–865 (2016).
124. Zhao, D. *et al.* Low-bandgap mixed tin–lead iodide perovskite absorbers with long carrier lifetimes for all-perovskite tandem solar cells. *Nat. Energy* **2**, 17018 (2017).
125. McMeekin, D. P. *et al.* Solution-Processed All-Perovskite Multi-junction Solar Cells. *Joule* **3**, 387–401 (2019).
126. Hörantner, M. T. *et al.* The Potential of Multijunction Perovskite Solar Cells. *ACS Energy Lett.* **2**, 2506–2513 (2017).

127. Vos, A. De. Detailed balance limit of the efficiency of tandem solar cells. *J. Phys. D. Appl. Phys.* **13**, 839–846 (1980).

128. Jiang, F. *et al.* A two-terminal perovskite/perovskite tandem solar cell. *J. Mater. Chem. A* **4**, 1208–1213 (2016).

129. Anaya, M. *et al.* Optical Description of Mesostructured Organic–Inorganic Halide Perovskite Solar Cells. *J. Phys. Chem. Lett.* **6**, 48–53 (2015).

130. Anaya, M. *et al.* Optical analysis of CH3NH3SnxPb1−xI3 absorbers: a roadmap for perovskite-on-perovskite tandem solar cells. *J. Mater. Chem. A* **4**, 11214–11221 (2016).

131. Shen, P.-S., Chiang, Y.-H., Li, M.-H., Guo, T.-F. & Chen, P. Research Update: Hybrid organic-inorganic perovskite (HOIP) thin films and solar cells by vapor phase reaction. *APL Mater.* **4**, 91509 (2016).

132. Ono, L. K., Leyden, M. R., Wang, S. & Qi, Y. Organometal halide perovskite thin films and solar cells by vapor deposition. *J. Mater. Chem. A* **4**, 6693–6713 (2016).

133. Sessolo, M., Momblona, C., Gil-Escrig, L. & Bolink, H. J. Photovoltaic devices employing vacuum-deposited perovskite layers. *MRS Bull.* **40**, 660–666 (2015).

134. Forgács, D. *et al.* Efficient Monolithic Perovskite/Perovskite Tandem Solar Cells. *Adv. Energy Mater.* **7**, 1602121 (2017).

135. Rühle, S. Tabulated values of the Shockley–Queisser limit for single junction solar cells. *Sol. Energy* **130**, 139–147 (2016).

136. Tress, W. Perovskite Solar Cells on the Way to Their Radiative Efficiency Limit – Insights Into a Success Story of High Open-Circuit Voltage and Low Recombination. *Adv. Energy Mater.* **7**, 1602358 (2017).

137. Green, M. A. *et al.* Solar cell efficiency tables (Version 55). *Prog. Photovoltaics Res. Appl.* **28**, 3–15 (2020).

Abbreviations

BCP	2,9-dimethyl-4,7-diphenyl-1,10-phenanthroline
CRJ	Charge recombination junction
EQE	External quantum efficiency
ETL	Electron transport layer
ETM	Electron transport material
F$_6$-TCNNQ	2,2′-(perfluoronaphthalene-2,6-diylidene)di-malononitrile
FF	Fill factor
HOMO	Highest occupied molecular orbital
HTL	Hole transport layer
HTM	Hole transport material
ITO	Indium tin oxide
J_{SC}	Short circuit current density
J-V	Current density versus voltage
LUMO	Lowest unoccupied molecular orbital
MAI	Methylammonium iodide
MAPI	Methylammonium lead iodide perovskite
P3HT	Poly(3-hexylthiophene)
PCE	Power conversion efficiency
PhIm	N1,N4-bis(tri-p-tolylphosphoranylidene)-benzene-1,4-diamine
PTAA	poly(triarylamine)
PV	photovoltaic
QCM	quartz crystal microbalance
(RuCp*mes)$_2$	pentamethylcyclopentadienyl mesitylene ruthenium dimer
Spiro-OMeTAD	2,2′,7,7′-tetrakis(N,N-di-p-methoxyphenylamine)-9,9′-spirobifluorene
TaTm	(N4,N4,N4″,N4″-tetra([1,1′-biphenyl]-4-yl)-[1,1′:4′,1″-terphenyl]-4,4″-diamine)
TCO	Transparent conductive oxide
V_{OC}	Open circuit voltage

List of contributions of the author

- Igual-Muñoz, A. M., **Ávila, J.**, Boix, P. P., & Bolink, H. J. (2019). FAPb0.5Sn0.5I3: A Narrow Bandgap Perovskite Synthesized through Evaporation Methods for Solar Cell Applications. Solar RRL, 0(0). https://doi.org/10.1002/solr.201900283
- **Ávila, J.**, La Placa, M.G., Longui, E., Sessolo, M., Barlow, S., Marder, S. R., and Bolink, H. J. (2019). Ruthenium pentamethylcyclopentadienyl mesitylene dimer: a sublimable n-dopant and electron buffer layer for efficient n-i-p perovskite solar cells. Journal Of Materials Chemistry a, 7, 25796-25801. https://doi.org/10.1039/C9TA09838K
- Neukom, M. T., Schiller, A., Züfle, S., Knapp, E., **Ávila, J.**, Pérez-del-Rey, D., Ruhstaller, B. (2019). Consistent Device Simulation Model Describing Perovskite Solar Cells in Steady-State, Transient, and Frequency Domain. ACS Applied Materials & Interfaces, 11(26), 23320–23328. https://doi.org/10.1021/acsami.9b04991
- Levine, I., Gupta, S., Bera, A., Ceratti, D., Hodes, G., Cahen, D., Guo, D., Savenije, T. J., **Ávila, J.**, Bolink, H. J., Millo, O., Azulay, D., and Balberg, I. (2018). Can we use time-resolved measurements to get steady-state transport data for halide perovskites? Journal of Applied Physics, 124(10). https://doi.org/10.1063/1.5037637
- **Ávila, J.**, Gil-Escrig, L., Boix, P. P., Sessolo, M., Albrecht, S., & Bolink, H. J. (2018). Influence of doped charge transport layers on efficient perovskite solar cells. Sustainable Energy Fuels, 2(11), 2429–2434. https://doi.org/10.1039/C8SE00218E
- Ullbrich, S., Fischer, A., Tang, Z., **Ávila, J.**, Bolink, H. J., Reineke, S., & Vandewal, K. (2018). Electrothermal Feedback and Absorption-Induced Open-Circuit-Voltage Turnover in Solar Cells. Phys. Rev. Applied, 9(5), 51003. https://doi.org/10.1103/PhysRevApplied.9.051003
- Hierlinger, C., Trzop, E., Toupet, L., **Ávila, J.**, La-Placa, M.-G., Bolink, H. J., … Zysman-Colman, E. (2018). Impact of the use of sterically congested Ir(iii) complexes on the performance of light-emitting electrochemical cells. J. Mater. Chem. C, 6(24), 6385–6397. https://doi.org/10.1039/C8TC01130C

- **Ávila, J.**, Momblona, C., Boix, P., Sessolo, M., Anaya, M., Lozano, G., … Bolink, H. J. (2018). High voltage vacuum-deposited CH3NH3PbI3–CH3NH3PbI3 tandem solar cells. Energy & Environmental Science, 11(11), 3292–3297. https://doi.org/10.1039/C8EE01936C
- **Ávila, J.**, Momblona, C., Boix, P. P., Sessolo, M., & Bolink, H. J. (2017). Vapor-Deposited Perovskites: The Route to High-Performance Solar Cell Production? Joule, 1(3), 431–442. https://doi.org/https://doi.org/10.1016/j.joule.2017.07.014
- Matteucci, E., Baschieri, A., Mazzanti, A., Sambri, L., **Ávila, J.**, Pertegás, A., … Armaroli, N. (2017). Anionic Cyclometalated Iridium(III) Complexes with a Bis-Tetrazolate Ancillary Ligand for Light-Emitting Electrochemical Cells. Inorganic Chemistry, 56(17), 10584–10595. https://doi.org/10.1021/acs.inorgchem.7b01544
- Forgács, D., Pérez-del-Rey, D., **Ávila, J.**, Momblona, C., Gil-Escrig, L., Dänekamp, B., … Bolink, H. J. (2017). Efficient wide band gap double cation – double halide perovskite solar cells. J. Mater. Chem. A, 5(7), 3203–3207. https://doi.org/10.1039/C6TA10727C
- Sherkar, T. S., Momblona, C., Gil-Escrig, L., **Ávila, J.**, Sessolo, M., Bolink, H. J., & Koster, L. J. A. (2017). Recombination in Perovskite Solar Cells: Significance of Grain Boundaries, Interface Traps, and Defect Ions. ACS Energy Letters, 2(5), 1214–1222. https://doi.org/10.1021/acsenergylett.7b00236
- Bandiello, E., **Ávila, J.**, Gil-Escrig, L., Tekelenburg, E., Sessolo, M., & Bolink, H. J. (2016). Influence of mobile ions on the electroluminescence characteristics of methylammonium lead iodide perovskite diodes. J. Mater. Chem. A, 4(47), 18614–18620. https://doi.org/10.1039/C6TA06854E
- El-Hajje, G., Momblona, C., Gil-Escrig, L., **Ávila, J.**, Guillemot, T., Guillemoles, J.-F., … Lombez, L. (2016). Quantification of spatial inhomogeneity in perovskite solar cells by hyperspectral luminescence imaging. Energy Environ. Sci., 9(7), 2286–2294. https://doi.org/10.1039/C6EE00462H
- Wetzelaer, G. a H., Scheepers, M., Sempere, A. M., Momblona, C., **Ávila, J.**, & Bolink, H. J. (2015). Trap-Assisted Non-radiative Recombination in Organic – Inorganic Perovskite Solar Cells. 1–5. https://doi.org/10.1002/adma.201405372

Annexes

Annex A – Chapter 3 reference:

Influence of doped charge transport layers on efficient perovskite solar cells.

Sustainable
Energy & Fuels

PAPER

View Article Online
View Journal | View Issue

Check for updates

Cite this: *Sustainable Energy Fuels*, 2018, **2**, 2429

Influence of doped charge transport layers on efficient perovskite solar cells†

Jorge Avila,[a] Lidon Gil-Escrig,[b] Pablo P. Boix,[a] Michele Sessolo,[a] Steve Albrecht*[b] and Henk J. Bolink*[a]

Received 11th May 2018
Accepted 3rd July 2018

DOI: 10.1039/c8se00218e

rsc.li/sustainable-energy

Planar vacuum deposited p–i–n methyl ammonium lead tri-iodide perovskite solar cells are prepared with different electron and hole transporting layers, either doped or undoped. The effect of these layers on the solar cells performance (efficiency and stability) is studied. The main benefit of using doped layers lies in the formation of barrier free charge extraction contacts to the electrodes. However, this comes at the cost of increased residual absorption (reducing the current density and efficiency of the cells) and a decreased stability. A generic solar cell structure using undoped charge extraction layers is presented, containing a thin layer of a strong electron acceptor in between the transparent electrode and the hole transport layer, that leads to efficiencies of 18% and a significant (>5 times) improvement of the stability.

Published on 03 July 2018. Downloaded on 4/10/2020 2:56:41 PM.

Introduction

Metal halide perovskite solar cells have become the most promising renewable power source.[1–4] The potential of this technology is evidenced by the rapid improvement in efficiency, reaching record values of 22.7%.[5] In the majority of the reported perovskite solar cells the absorber layer is sandwiched in between charge selective transport layers.[6] These layers have to ensure rectification which is essential to achieve high open circuit voltages (V_{oc}'s).[7] Additionally, these layers have to transport and inject the selected carrier to the contact, thus their conductivity is frequently enhanced by "doping" them with additives that lead to excess charges in the layers.[8] Probably the most prominent example is the hole transport layer (HTL) based on partially oxidized (doped) spiro-OMeTAD.[9] The benefit of using doped layers is a reduced series resistance and the formation of ohmic contacts to the external electrodes, which enhances the solar cell fill factor. One drawback of the use of doped charge transport layers is their negative effect on the device lifetime.[10] The above mentioned generality is found in particular for solar cells employing perovskite layers that are solution processed.[11,12] Much less information is available for solar cells employing perovskite films prepared using a dry vapor based deposition process. In a recent report, it was demonstrated that the use of doped charge transport layers is also beneficial for the performance of vacuum deposited perovskite solar cells.[13] In that case, however, it was shown to be essential to prevent a direct contact between the perovskite absorber and the doped layers, which would otherwise results in substantial charge recombination. For this reason, a thin layer of the pure (undoped) organic charge transport molecules was inserted in between the doped charge transport layer and the perovskite absorber.[13] Similar effects are known from work with organic light-emitting diodes and photovoltaic devices were such non-doped layers prevent the quenching of excitons.[8] It is likely that for perovskite solar cells the elimination of the doped layers adjacent to the perovskite reduces charge recombination and enhances the device performance due to improved rectification, as was recently also mentioned in another study.[14] Besides this there are other drawbacks associated to the doping of the contacts. On the one hand, the stability of solar cells using doped layers is generally below that of those employing non-doped charge transport layers; on the other, doping generally enhances parasitic absorption. This is in particular the case when arylamine containing molecules (which are common hole transport materials) are partially oxidized by the dopants. The radical cation of arylamines has a characteristic optical absorption band in the visible region of the spectrum in the 500–600 nm range.[15] Hence, this reduces the light that reaches the perovskite layer and hence the achievable current density the cells can produce. This is of some importance in the n–i–p configuration (that is with the electron transporting layer, ETL, on the illuminated side of the cell and the hole transporting layer behind the perovskite layer) as the amount of reflected sunlight from the metal top electrode is reduced. However, this parasitic absorption is more prominent when the sunlight passes through the doped hole transport layer prior to reaching the perovskite absorber, in the so-called p–i–n

---

[a] *Instituto de Ciencia Molecular, Universidad de Valencia, C/J. Beltrán 2, 46980, Paterna, Spain. E-mail: henk.bolink@uv.es*

[b] *Helmholtz-Zentrum Berlin für Materialien und Energie GmbH, Young Investigator Group for Perovskite Tandem Solar Cells, Kekuléstraße 5, 12489 Berlin, Germany. E-mail: steve.albrecht@helmholtz-berlin.de*

† Electronic supplementary information (ESI) available: Experimental details, thin film analysis (X-ray, absorption and SEM), statistics of device performance and details of the performance over time. See DOI: 10.1039/c8se00218e

Published on 03 July 2018. Downloaded on 4/10/2020 2:56:41 PM.

configuration. It is therefore, of interest to prepare p–i–n type perovskite solar cells, that do not require doped hole transport layers (HTLs) yet do provide efficient charge extraction to the transparent front electrode as this is expected to increase the current density and hence the PCE of the devices. At the same time, it is also of interest to eliminate the doped electron transport layer (ETL) placed on top of the perovskite absorber layer as this may lead to improved stabilities.

Here, we study the influence of the doped and undoped transport layers on the performance and stability of thin film perovskite solar cells in the p–i–n configuration. The p–i–n configuration was selected as the parasitic absorption in doped p-type layers is higher than in doped n-type layers. Methyl ammonium lead tri-iodide ($MAPbI_3$) prepared *via* co-sublimation of its precursors was used as the perovskite absorber. An intrinsic advantage of vacuum deposition is the possibility to selectively remove and exchange any layer and study the effect on the overall device performance. It was found that the ITO- undoped-HTL interface is preventing efficient charge extraction which was overcome by the insertion of a thin layer of the molecule used to oxidize the hole transport molecule, 2,2′-(perfluoronaphthalene-2,6-diylidene)di-malononitrile (F_6-TCNNQ) (Fig. 1) in between the ITO and the HTL. The doped ETL is replaced by a bilayer of 2,9-dimethyl-4,7-diphenyl-1,10-phenanthroline (BCP) (Fig. 1) and Ag. Using this approach, the power conversion efficiency of the p–i–n solar cells is enhanced to more than 18%, whereas at the same time the stability is notably improved.

The $MAPbI_3$ perovskite thin films were prepared by co-evaporation of the two starting compounds, CH_3NH_3I and PbI_2. Details of the experimental conditions for the perovskite layer have been described previously and are presented in the ESI.†[16] Out of the two perovskite precursors, CH_3NH_3I and PbI_2, the first is somewhat complicated to sublime. However, once properly outgassed (using the high vacuum of the evaporation chamber) the material is sublimed similarly like small molecular weight organic molecules, that is, the rate of evaporation is stable as monitored by the microbalance crystal sensors that are positioned in the chamber. These films were characterized using grazing incidence X-ray diffraction (GIXRD) showing the typical diffraction pattern for this material which is independent on the type of organic under-layer employed (Fig. S1a in the ESI†). Scanning electron microscopy (SEM) images of the perovskite surface (Fig. S1c in the ESI†) show a dense packing of crystals, virtually without pinholes, that have an average domain size of approximately 100 nm. Note that the domain size here is not depending on the type of under-layer employed. The optical absorption spectra of these films show the expected $MAPbI_3$ band-to-band transition at 780 nm and high absorbance over the whole visible spectra (Fig. S1b in the ESI†). These perovskite layers were used to prepare planar diodes by sandwiching a 500 nm thick perovskite layer in between organic HTLs and ETLs, the first on top of a pre-patterned indium tin oxide (ITO) coated glass substrate and by thermally evaporating a metal top contact on the latter. A vacuum deposited $MAPbI_3$ layer with a thickness of 500 nm was selected as previous studies showed that almost all sun light with energy above the band-gap is absorbed and still all charge carriers can reach the respective interfaces without significant transport losses within the absorber layer.[17] Both the electron selective and hole selective organic charge transport layers were prepared by vacuum sublimation of the corresponding organic molecules to

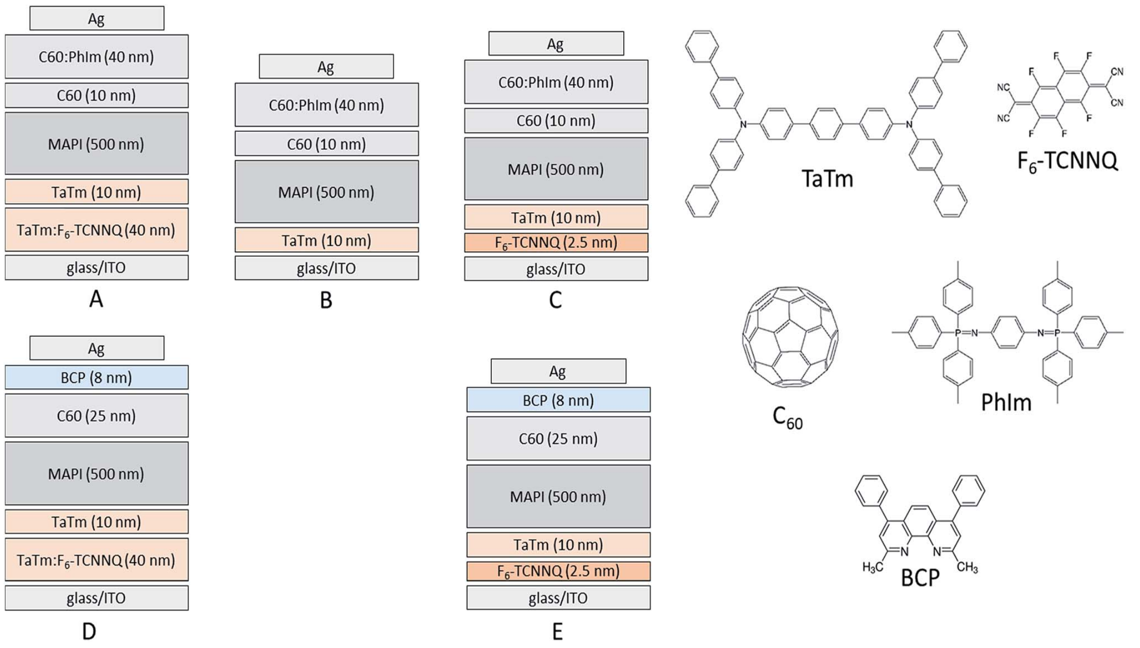

Fig. 1 Layout of the studied devices, A, B, C, D and E each one with a different combination of doped and undoped transport layers and chemical structures of the transport materials.

This journal is © The Royal Society of Chemistry 2018

Published on 03 July 2018. Downloaded on 4/10/2020 2:56:41 PM.

a layer thickness of 10 nm. We selected a derivative of an arylamine, *N*4,*N*4,*N*4″,*N*4″-tetra([1,1′-biphenyl]-4-yl)-[1,1′:4′,1″-terphenyl]-4,4″-diamine (TaTm) (Fig. 1) as the hole transport molecule due to its very stable sublimation conditions and tendency to form completely amorphous films. The fullerene C_{60} was selected as the electron transport molecule as it is also easy to sublime and has proven to be an efficient electron acceptor in perovskite solar cells.[18] To ensure sufficient statistics, for each device configuration mentioned in this report, at least 2 different substrates each containing 4 cells were evaluated, while for top performing configurations at least 5 different substrates with a total of 20 cells were characterized. The device area used, defined as the aperture of the shadow mask, was 1 mm^2, whereas the overlap area between front and back electrode was 4 mm^2. This configuration was used to make sure the performance of the cell is not overestimated although it leads to a slight underestimation of the V_{oc}.[19] Doping of the HTL was achieved by co-evaporating the molecule F_6-TCNNQ with the TaTm at a ratio TaTm : F_6-TCNNQ of 11% as determined by the microbalance crystal sensor evaporation rate monitors. Doping of the C_{60} layer was achieved by co-evaporating the molecule *N*1,*N*4-bis(tri-*p*-tolylphosphoranylidene)-benzene-1,4-diamine (PhIm) (Fig. 1) at a ratio C_{60} : PhIm of 30% as determined by the microbalance crystal sensor evaporation rate monitors. More details of the fabrication process can be found in the ESI.†

Five different types of devices were prepared and evaluated which are depicted in Fig. 1 and named A, B, C, D and E, respectively. Device A is the reference in which both a doped HTL and a doped ETL are used. In device B, the doped HTL is removed and the TaTm layer is in direct contact with the ITO front electrode. Device C is similar to device B, but a thin (2.5 nm) layer of the molecule F_6-TCNNQ is deposited on top of the ITO prior to depositing the HTL. In device D and E, the configuration on the p-contact side is copied from device A and C, whereas the doped C_{60} layer is substituted by a thin layer (8 nm) of BCP. Such an ETL approach (C_{60}/BCP/Ag) has been used in organic photovoltaics,[20] and was also adopted to perovskite solar cells.[21] All devices use an Ag top electrode of 100 nm.

As discussed before, the perovskite film properties are very similar for all type of devices, which is expected as in all cases it is formed directly on top of the TaTm HTL. Furthermore, the different device configurations were prepared in a single perovskite sublimation run, ensuring that the perovskite layer is identical for all these devices (the best performing device configurations were then also prepared separately to obtain more statistics). The dark current density–voltage (*J*–*V*) curves of the finished diodes are depicted in Fig. 2 and show low leakage current in all cases as well as a steep rise of the current density at ~0.5 V. This implies that the layer quality is good and even though thin charge selective layers are used this does not lead to shunts in the diode. For device B, however, this rise in current density is much less pronounced. As the only difference is the interface this result implies that there is a barrier for hole-injection in this device type. Additionally, device A, with doped HTL and doped ETL shows a higher leakage current, in line with the higher conductivity of these layers.

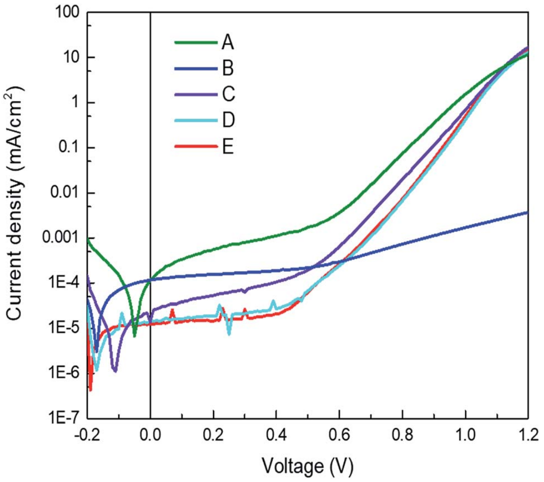

Fig. 2 Typical current density *versus* voltage characteristics for the series of devices in the dark.

Using AM 1.5G simulated sun illumination at an intensity of 100 mW cm^{-2} the *J*–*V* curves of the different cells were again determined. These *J*–*V* curves under illumination are depicted in Fig. 3a, both in forward and backward scan direction. For all type of devices there is very little hysteresis in the *J*–*V* curves and is therefore considered negligible here. The reference device, A, performs similar as reported previously,[13] reaching for the best cell; J_{sc} of 20.7 mA cm^{-2}, a V_{oc} of 1.08 V and a fill factor (FF) of 72%, leading to a PCE of 16.2%. When the doped HTL is removed, referred to as device B, the *J*–*V* curve under illumination shows a low fill factor with a pronounced S-shape, indicating issues with charge extraction and injection. This corroborates the conclusion drawn from the dark *J*–*V* curves. The only difference between device A and B is the removal of the doped layer at the ITO/HTL interface hence, the origin for the poor *J*–*V* curves must originate from that interface. This is not unexpected in view of the large energy offset between the work function of ITO (4.8 eV) and the highest occupied molecular orbital (HOMO) of TaTm (5.4 eV). This and the *J*–*V* results, clearly indicate that the contact between ITO and TaTm is not without a barrier. Hence, to alleviate this and ensure a barrier-free charge extraction, a thin layer (2.5 nm) of the F_6-TCNNQ was deposited on top of the ITO prior to the deposition of the TaTm (device C). As can be seen from Fig. 3, the *J*–*V* curve of this type of device (type C) is again approaching a rectangular shape (FF = 79%) indicating that the extraction barrier has been removed. Additionally, the J_{sc} of device C is substantially increased when compared with that of device A. This effect can be understood when comparing the EQE graphs of the different devices (Fig. 3b) where device C has an enhanced spectral response in the blue-green region of the solar spectrum. Even though it is probable that at the interface between the 2.5 nm of F_6-TCNNQ and TaTm a small fraction of TaTm molecules gets oxidized (ensuring a good electrical contact between them) this does not lead to a very pronounced increase in the absorption of the film. The spontaneous transfer of an electron from the

Published on 03 July 2018. Downloaded on 4/10/2020 2:56:41 PM.

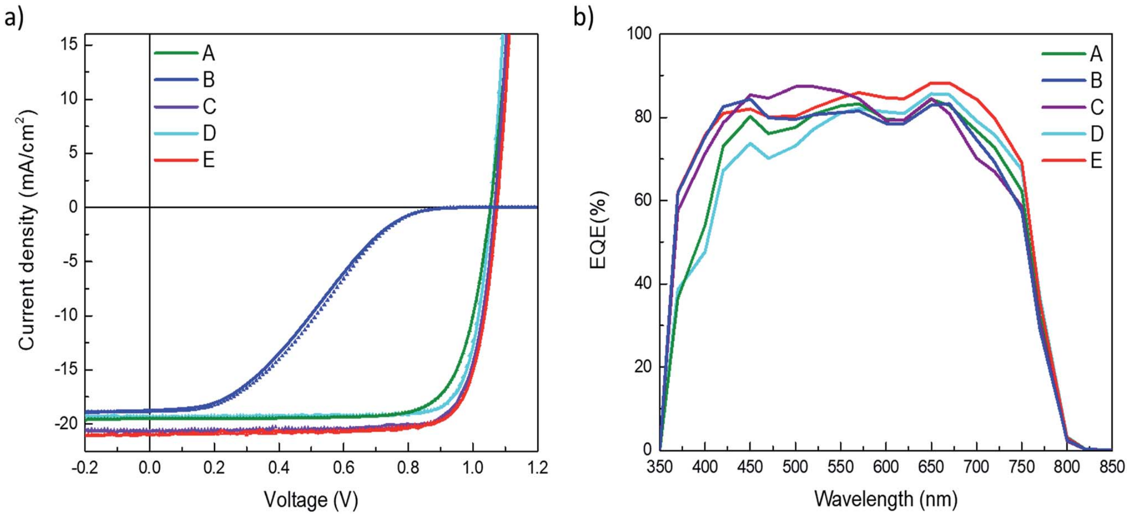

Fig. 3 (a) Representative *J–V* characteristics measured under simulated AM 1.5G-illumination in forward (dotted line) and reverse (straight line) scan direction for each studied device. (b) External quantum efficiency (EQE) spectra for the same device series.

TaTm to the F_6-TCNNQ layer upon contact between the two leads to excess electrons in the LUMO of the F_6-TCNNQ and holes in the HOMO of the TaTm. The excess electrons in the LUMO are responsible for the formation of the ohmic contact between the ITO electrode and F_6-TCNNQ layer. In Fig. 4 the absorption and transmission of the two types of HTL are depicted. These layers were prepared on glass substrates and consisted of TaTm : F_6-TCNNQ (40 nm)/TaTm (10 nm) and F_6-TCNNQ (2.5 nm)/TaTm (10 nm) resembling the stack in device A and C respectively. Indeed, there is a substantial decrease in the absorption spectrum for the HTL double layer of device C when compared to that of the reference device (A). The reduction in the visible part of the spectrum is primarily due to the absence of the absorption band around 500 nm. This reduction in the parasitic absorption leads to more light reaching the perovskite, which therefore explains the increase in J_{sc} for this configuration. Moreover, the bi-layer type HTL used in device C shows excellent transmittance up to 1300 nm, which makes it a valuable option for use in tandem applications with low bandgap absorbers such as silicon.

Device type D and E, have similar J_{sc} and V_{oc} as device A and C. The similar J_{sc}'s are expected as the front contacts are unvaried and the effect of the top charge transport layer on the optical absorption is small. This is due to the use of the thick perovskite layer which absorbs virtually all the sun-light in the first pass. There is a small improvement in the FF for device D when compared to device A. This may be due to an increased rectification and or charge extraction for the C_{60}/BCP/Ag stack.

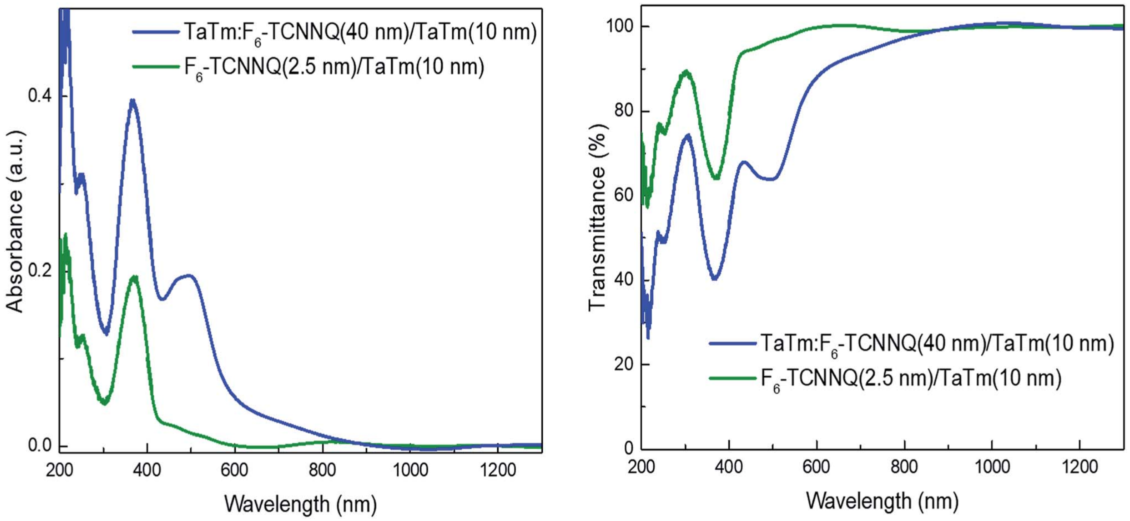

Fig. 4 Absorbance (left) and transmission (right) spectra of the hole transport layers for devices A, D and C, E, blue and green lines, respectively.

This journal is © The Royal Society of Chemistry 2018

Published on 03 July 2018. Downloaded on 4/10/2020 2:56:41 PM.

An overview of the key performance indicators for all type of devices is depicted in Table 1 (record values) and the statistics of each device type is shown in Fig. S2 in the ESI.† As device B, was not performing well, for this configuration only a few cells were prepared.

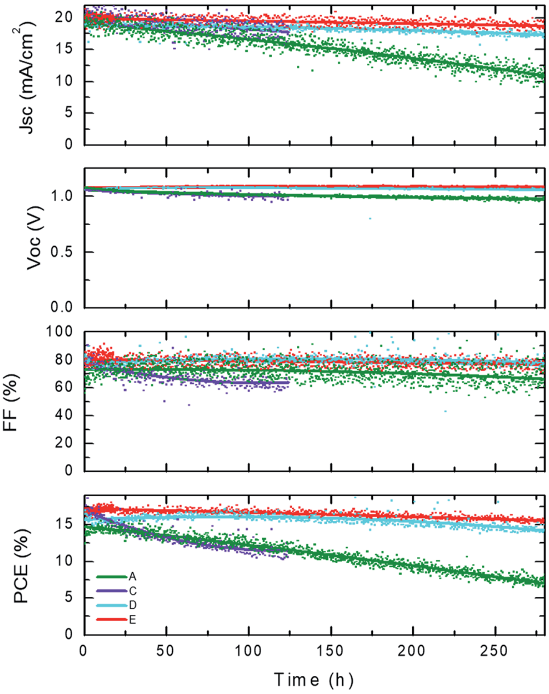

Fig. 5 *J–V* characteristic parameters *versus* time measured under continuous LED illumination in inert atmosphere. Device are maintained at short circuit conditions and each hour a *JV* scan is performed.

To obtain an indication of the stabilities of the different cell configurations they were analyzed during prolonged exposure to white LED light (spectra in Fig. S3 in the ESI†), except for the moderately performing device B. The light intensity was adjusted to mimic the J_{sc} value obtained under AM 1.5G illumination. The temperature of the cells during this test reached approximately 40 °C in the first 10 minutes and remained constant afterwards. The setup consisted of 8 test positions installed inside a nitrogen filled glovebox (with oxygen and H_2O levels below 1 ppm). All cells were continuously illuminated under short-circuit conditions without encapsulation and evaluated within a few days after preparation. At fixed time intervals (1 hour, initially) *J–V* scans were taken to deduce the evolution of the key performance indicators of the cells, including the PCE (Fig. S4 in the ESI†). This type of ageing experiment provides an indication of the stability. Maximum power point tracking is the preferred way of determining the stability of the cells as it most closely resembles real operation conditions. However, considering the negligible hysteresis of the analyzed devices, this type of measurement gives additional information. In particular, it allows to determine which parameter is causing the power efficiency decay allowing to postulate possible degradation mechanisms. Some examples of the *J–V* scans for each device configuration at set times of operation under constant illumination are depicted in Fig. S5.† The evolution of the performance parameters over time are depicted in Fig. 5 and the zoomed in version in Fig. S4.† We can distinguish two types of behavior for the different devices. The device types D and E, both having the C_{60}/BCP/Ag ETL stack, are stable over more than 280 hours under continuous illumination, with only a decrease of ~10% of the PCE. This reduction is mainly due to a drop in J_{sc}. Interestingly, the V_{oc} increases slightly over the first 100 hours, which we postulate is due to the passivation of trap states at the interface between the perovskite and the organic charge extraction layers. A very different behavior is observed for the devices of type A and C that employ the C_{60}/C_{60} : PhIm layer as the ETL stack. These two types of devices are less stable and after approximately 100 hours a reduction in the PCE to 80% has already taken place. The decay in these cases appears to be driven by all the parameters and especially by the J_{sc} and the FF which drop faster than in the devices with undoped electron transport layers. These results indicate that the deterioration of these cells is related to an increase in the series resistance which is likely to be related to the ETL as both devices have only this layer in common. It is possible that de-doping of the C_{60} layer occurs as this layer is only protected by a sublimed (not-pinhole free) metal electrode which would lead to an extraction barrier at the metal interface, decreasing the stability of the devices considerably. This degradation also leads to S-shaped *J–V* curves. It is important to note that in all these devices the perovskite layer is the same, a vacuum deposited $MAPbI_3$ layer, which implies that with the proper contacts these devices can be rather stable.

Table 1 *J–V* parameters of the best devices for each configuration, measured under standard AM 1.5G illumination, due to the very small hysteresis no difference in forward and reverse scan can be seen

	PCE (%)	J_{sc} (mA cm^{-2})	V_{oc} (mV)	FF (%)
A	16.2	20.8	1076	72.5
B	5.4	18.8	1032	27.9
C	17.9	21.3	1056	79.4
D	16.9	19.6	1052	81.7
E	18.2	21.3	1059	80.4

Conclusions

In conclusion the performance and stability of planar p–i–n perovskite solar cells is significantly enhanced when the doped charge transport layers are replaced by undoped alternatives. When substituting the doped hole transport layer with an undoped equivalent it was found that a charge injection/extraction barrier is present at the ITO-HTL interface. This was eliminated by inserting a very thin layer of the pure dopant molecule in between the ITO and the HTL. The main benefit of using undoped HTL in the p–i–n configuration is the strong reduction of the parasitic absorption. This leads to an enhancement of the spectral response in the blue part of the solar spectrum and hence to an increase in the current density. The elimination of reactive electron transport layers on top of

Published on 03 July 2018. Downloaded on 4/10/2020 2:56:41 PM.

the perovskite results in a significant increase in the solar cell stability. Interestingly, the bilayer C_{60}/BCP ETL lead to diodes with high rectifications comparable to the much more conductive C_{60}/C_{60}-PhIm layer, as evidenced by the high FF obtained. The generic architectures identified here can yield very efficient and rather stable solar cells, and might be used in a wide range of planar type perovskite solar cells and multi-junction architectures.

Conflicts of interest

There are no conflicts to declare.

Acknowledgements

We acknowledge financial support from the European Union H2020 project INFORM (grant 675867), the Spanish Ministry of Economy and Competitiveness (MINECO) *via* the Unidad de Excelencia María de Maeztu MDM-2015-0538, MAT2017-88821-R, PCIN-2015-255 and MAT2017-88905-P, and the Generalitat Valenciana (Prometeo/2016/135). H. B. acknowledges the support of ERA NET PCIN-2017-014. M. S. and P. P. B. thank the MINECO for their post-doctoral RyC contracts. P. P. B. acknowledges the financial support from the Conselleria d'Educació, Investigació, Cultura i Esport Valenciana (SEJI2017/2017/012). "J. Á. thanks the Spanish Ministry of Education, Culture and Sport for his pre-doctoral grant (FPU)." S. A. acknowledges the BMBF within the project "Materialforschung für die Energiewende" for funding of his Young Investigator Group (Grant No. 03SF0540); he acknowledges the German Federal Ministry for Economic Affairs and Energy (BMWi) for funding of the "PersiST" project (Grant No. 0324037C). L. G. E. is funded by the Helmholtz Innovation Lab HySPRINT, which is financially supported by the Helmholtz Association.

References

1 A. Kojima, K. Teshima, Y. Shirai and T. Miyasaka, *J. Am. Chem. Soc.*, 2009, **131**, 6050–6051.
2 H.-S. Kim, C.-R. Lee, J.-H. Im, K.-B. Lee, T. Moehl, A. Marchioro, S.-J. Moon, R. Humphry-Baker, J.-H. Yum, J. E. Moser, M. Gratzel and N.-G. Park, *Sci. Rep.*, 2012, **2**, 591.
3 M. M. Lee, J. Teuscher, T. Miyasaka, T. N. Murakami and H. J. Snaith, *Science*, 2012, **338**, 643–647.
4 H. J. Snaith, *J. Phys. Chem. Lett.*, 2013, **4**, 3623–3630.
5 W. S. Yang, B.-W. Park, E. H. Jung, N. J. Jeon, Y. C. Kim, D. U. Lee, S. S. Shin, J. Seo, E. K. Kim, J. H. Noh and S. Il Seok, *Science*, 2017, **356**, 1376–1379.
6 C. Zuo, H. J. Bolink, H. Han, J. Huang, D. Cahen and L. Ding, *Adv. Sci.*, 2016, **3**, 1500324.
7 C. M. Wolff, F. Zu, A. Paulke, L. P. Toro, N. Koch and D. Neher, *Adv. Mater.*, 2017, **29**, 1–8.
8 K. Walzer, B. Maennig, M. Pfeiffer and K. Leo, *Chem. Rev.*, 2007, **107**, 1233–1271.
9 A. Abate, T. Leijtens, S. Pathak, J. Teuscher, R. Avolio, M. E. Errico, J. Kirkpatrik, J. M. Ball, P. Docampo, I. McPherson and H. J. Snaith, *Phys. Chem. Chem. Phys.*, 2013, **15**, 2572–2579.
10 S. N. Habisreutinger, D. P. Mcmeekin, H. J. Snaith and J. Robin, *APL Mater.*, 2016, **4**, 1–32.
11 R. S. Sanchez and E. Mas-Marza, *Sol. Energy Mater. Sol. Cells*, 2016, **158**, 189–194.
12 S. Cacovich, G. Divitini, C. Ireland, F. Matteocci, A. Di Carlo and C. Ducati, *ChemSusChem*, 2016, **9**, 2673–2678.
13 C. Momblona, L. Gil-Escrig, E. Bandiello, E. M. Hutter, M. Sessolo, K. Lederer, J. Blochwitz-Nimoth and H. J. Bolink, *Energy Environ. Sci.*, 2016, **9**, 3456–3463.
14 J.-P. Correa-Baena, W. Tress, K. Domanski, E. H. Anaraki, S.-H. Turren-Cruz, B. Roose, P. P. Boix, M. Grätzel, M. Saliba, A. Abate and A. Hagfeldt, *Energy Environ. Sci.*, 2017, **10**, 1207–1212.
15 S. Dapperheld, E. Steckhan, K. G. Brinkhaus and T. Esch, *Chem. Ber.*, 1991, **124**, 2557–2567.
16 O. Malinkiewicz, A. Yella, Y. H. Lee, G. M. M. Espallargas, M. Graetzel, M. K. Nazeeruddin and H. J. Bolink, *Nat. Photonics*, 2014, **8**, 128–132.
17 C. Momblona, O. Malinkiewicz, C. Roldán-Carmona, a. Soriano, L. Gil-Escrig, E. Bandiello, M. Scheepers, E. Edri and H. J. Bolink, *APL Mater.*, 2014, **2**, 81504.
18 P.-W. Liang, C.-C. Chueh, S. T. Williams and A. K.-Y. Jen, *Adv. Energy Mater.*, 2015, **5**, 1402321.
19 X. Xu, J. Shi, H. Wu, Y. Yang, J. Xiao, Y. Luo, D. Li and Q. Meng, *J. Renewable Sustainable Energy*, 2015, **7**, 43104.
20 P. Peumans, V. Bulović and S. R. Forrest, *Appl. Phys. Lett.*, 2000, **76**, 2650–2652.
21 Z. Xiao, C. Bi, Y. Shao, Q. Dong, Q. Wang, Y. Yuan, C. Wang, Y. Gao and J. Huang, *Energy Environ. Sci.*, 2014, **7**, 2619.

This journal is © The Royal Society of Chemistry 2018

Electronic Supplementary Material (ESI) for Sustainable Energy & Fuels.
This journal is © The Royal Society of Chemistry 2018

Influence of doped charge transport layers on efficient perovskite solar cells.

Jorge Avila[1], Lidon Gil-Escrig[2], Pablo P. Boix[1], Michele Sessolo[1], Steve Albrecht[2] and Henk J. Bolink*[1]*

[1]Instituto de Ciencia Molecular, Universidad de Valencia, C/ J. Beltrán 2, 46980, Paterna, Spain
[2]Helmholtz-Zentrum Berlin für Materialien und Energie GmbH, Young Investigator Group for Perovskite Tandem Solar Cells, Kekuléstraße 5, 12489 Berlin, Germany

Supporting Information

Materials. Photolithographically patterned ITO coated glass substrates were purchased from Naranjo Substrates (www.naranjosubstrates.com). 2,2'-(Perfluoronaphthalene-2,6-diylidene) dimalononitrile (F_6-TCNNQ), N4,N4,N4",N4"-tetra([1,1'-biphenyl]-4-yl)-[1,1':4',1"-terphenyl]-4,4"-diamine (TaTm) and N1,N4-bis(tri-p-tolylphosphoranylidene)benzene-1,4-diamine (PhIm) were provided from Novaled GmbH. Fullerene (C_{60}) was purchased from sigma Aldrich and 2,9-Dimethyl-4,7-diphenyl-1,10-phenanthroline (BCP) from Lumtec. PbI_2 was purchased from Tokyo Chemical Industry CO (TCI), and CH_3NH_3I (MAI) from Lumtec**.**

Device preparation. ITO-coated glass substrates were subsequently cleaned with soap, water and isopropanol in an ultrasonic bath, followed by UV-ozone treatment. They were transferred to a vacuum chamber integrated into a nitrogen-filled glovebox (MBraun, H_2O and $O_2 < 0.1$ ppm) and evacuated to a pressure of $1 \cdot 10^{-6}$ mbar. The vacuum chamber uses a turbomolecular pump (Pfeiffer TMH 261P, DN 100 ISO-K, 3P) coupled to a scroll pump. The vacuum chamber is equipped with six temperature controlled evaporation sources (Creaphys) fitted with ceramic crucibles. The sources were directed upwards with an angle of approximately 90º with respect to the bottom of the evaporator. The substrate holder to evaporation sources distance is approximately 20 cm. Three quartz crystal microbalance (QCM) sensors are used, two monitoring the deposition rate of each evaporation source and a third one close to the substrate holder monitoring the total deposition rate. For thickness calibration, we first individually sublimed the charge transport materials and their dopants (TaTm and F_6-TCNNQ, C_{60} and PhIm). A calibration factor was obtained by comparing the thickness inferred from the QCM sensors with that measured with a mechanical profilometer (Ambios XP1). Then these materials were co-sublimed at temperatures ranging from 135-160 ºC for the dopants to 250 ºC for the pure charge transport molecules, and the evaporation rate was controlled by separate QCM sensors and adjusted to obtain the desired doping concentration. In general, the deposition rate for TaTm and C_{60} was kept constant at 0.8 Å s^{-1} while varying the deposition rate of the dopants during co-deposition. Pure TaTm, F_6-TCNNQ, BCP and C_{60} layers were deposited at a rate of 0.5 Å s^{-1}.

For devices A and D, 40 nm of the p-doped hole-transport layer (TaTm: F_6-TCNNQ) capped with 10 nm of the pure TaTm were deposited. For devices B, only 10 nm of TaTm was evaporated. For devices C and E, a thin (2.5 nm) layer of the molecule F_6-TCNNQ is deposited on top of the ITO prior to depositing the layer of TaTm. Once completed this deposition, the chamber was vented with dry N_2 to replace the HTL crucibles with those containing the starting materials for the perovskite deposition, PbI_2 and CH_3NH_3I. The vacuum chamber was evacuated again to a pressure of 10^{-6} mbar, and the perovskite films were then obtained by co-deposition of the two precursors. The use of clean QCM sensors for the perovskite evaporation is important to avoid false readings due to perovskite formation on the sensor. For a more accurate deposition the density of PbI_2 (6.16 g/cm^3) is set in the equipment. For CH_3NH_3I the density is assumed to be 1 g/cm^3. And the z-factor for both materials is set to 1. The calibration of the deposition rate for the CH_3NH_3I was found to be difficult due to non-uniform layers and the soft nature of the material which impeded accurate thickness measurements. Hence, the source temperature of the CH_3NH_3I was kept constant at 70 ºC and the CH_3NH_3I:PbI_2 ratio was controlled off line using grazing incident x-ray diffraction by adjusting the PbI_2 deposition temperature. The optimum deposition temperatures were found to be 250 ºC for the PbI_2 and 70 ºC for the CH_3NH_3I. After deposition of a 500 nm thick perovskite film, the chamber was vented, and the crucibles replaced with those containing the electron-transport materials and evacuated again to a pressure of 10^{-6} mbar. The devices were completed depositing a film of pure C_{60} (10 nm for devices A, B and C; 25 nm for devices D and E). In the case of devices A, B and C, 40 nm of the n-doped hole-transport layer (C_{60}: PhIm) was evaporated. On devices D and E, the doped C_{60} layer is substituted by a thin layer (8 nm) of BCP. Afterwards the metal top contact (Ag, 100 nm thick) was deposited.

Characterization. Grazing incident X-ray diffraction (GIXRD) pattern were collected at room temperature on an Empyrean PANanalytical powder diffractometer using the Cu Kα1 radiation. Typically, three consecutive measurements were collected and averaged into single spectra. Scanning Electron Microscopy (SEM) images were performed on a Hitachi S-4800 microscope operating at an accelerating voltage of 2 kV over Platinum - metallized samples. Absorption spectra were collected using a fiber optics based Avantes Avaspec2048 Spectrometer. Characterization of the solar cells was performed as follows. The external quantum efficiency (EQE) was estimated using the cell response at different wavelength (measured with a white light halogen lamp in combination with band-pass filters), where the solar spectrum mismatch is corrected using a calibrated Silicon reference cell (MiniSun simulator by ECN, the Netherlands). The current density-voltage (J-V) characteristics were obtained using a Keithley 2400 source measure unit and under white light illumination, and the short circuit current density was corrected considering the device EQE. The electrical characterization was validated using a solar simulator by Abet Technologies (model 10500 with an AM1.5G xenon lamp as the light source). Before each measurement, the exact light intensity was determined using a calibrated Si reference diode equipped with an infrared cut-off filter (KG-3, Schott). The J-V curves were recorded between -0.2 and 1.2 V with 0.01 V steps, integrating the signal for 20 ms after a 10 ms delay. This corresponds to a speed of about 0.3 V s^{-1}. The layout used to test the solar cells has four equal areas (0.04 cm^2, defined as the overlap between the ITO and the top metal contact) and measured through a shadow mask with 0.01 cm^2 aperture.

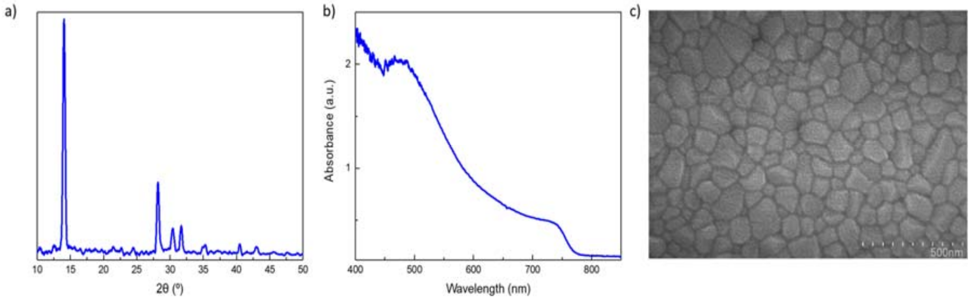

Fig S1 (a) GIXRD pattern, (b) optical absorbance and (c) surface SEM picture of the vacuum deposited $CH_3NH_3PbI_3$ thin films for devices preparation.

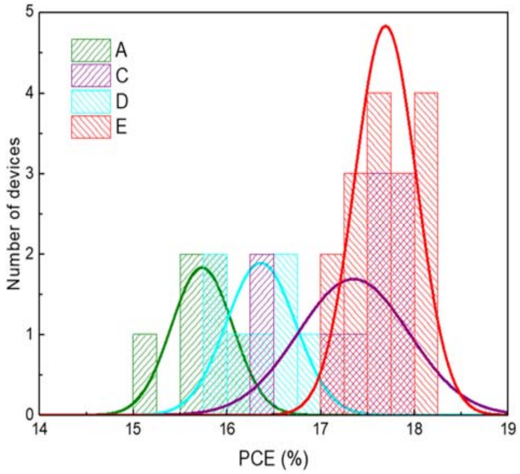

Fig S2 Statistic of the PCE measured for each type of devices. Solid lines represent the Gaussian distribution fitting for the PCE.

Table S1 Statistical distribution of J-V parameters of devices measured under standard AM1.5G illumination.

	PCE (%)	J_{sc} (mA/cm^2)	V_{oc} (mV)	FF (%)
A	15.7 ± 0.3	19.6 ± 1.1	1069 ± 8	75 ± 3
B	5.4	18.8	1032	27.9

C	17.4 ± 0.6	20.7 ± 0.5	1061 ± 13	79.1 ± 1.6
D	16.4 ± 0.4	19.2 ± 0.5	1058 ± 7	80.5 ± 1.7
E	17.7 ± 0.3	20.6 ± 0.4	1065 ± 5	80.7 ± 1.0

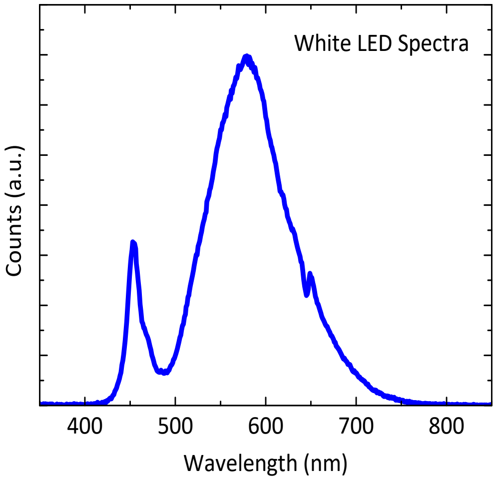

Fig S3 Optical emission spectrum of the white LED used to illuminate the solar cells during life time measurements.

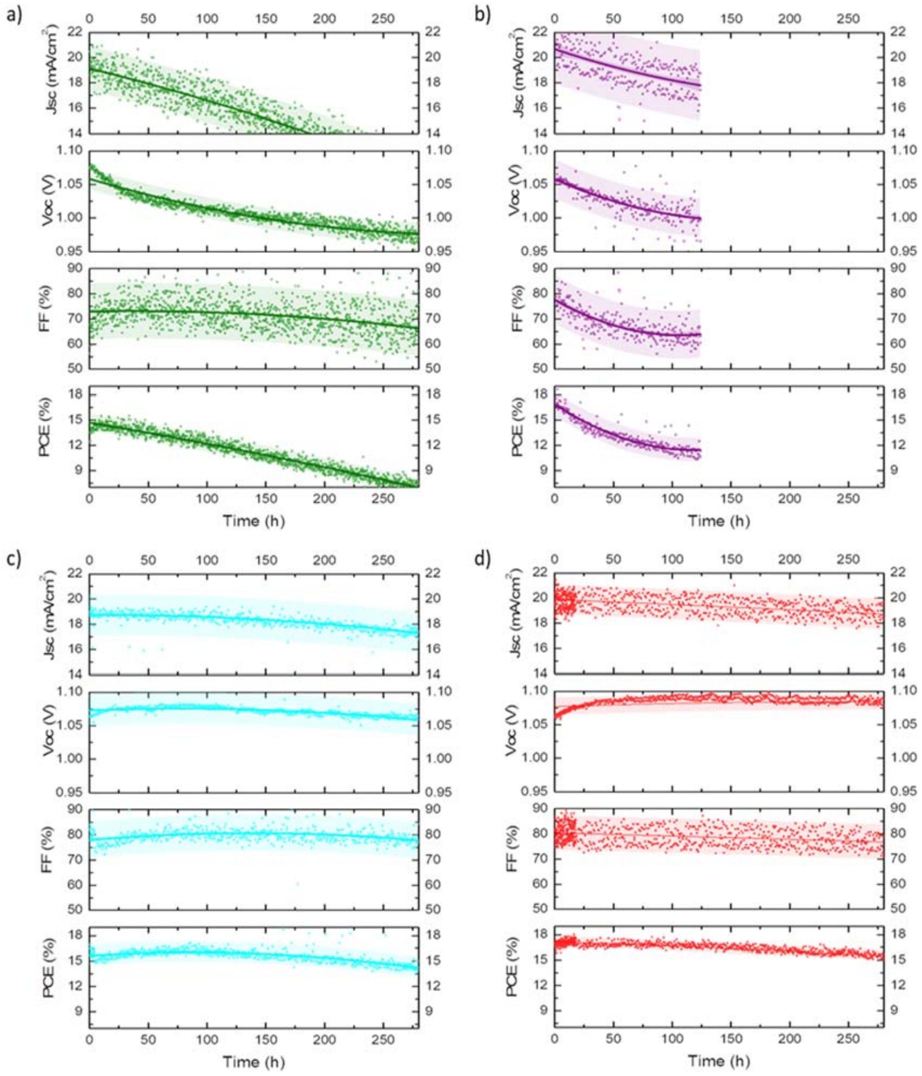

Figure S4 J-V characteristic parameters versus time measured under continuous illumination for devices A(a), C(b), D(c) and E(d).

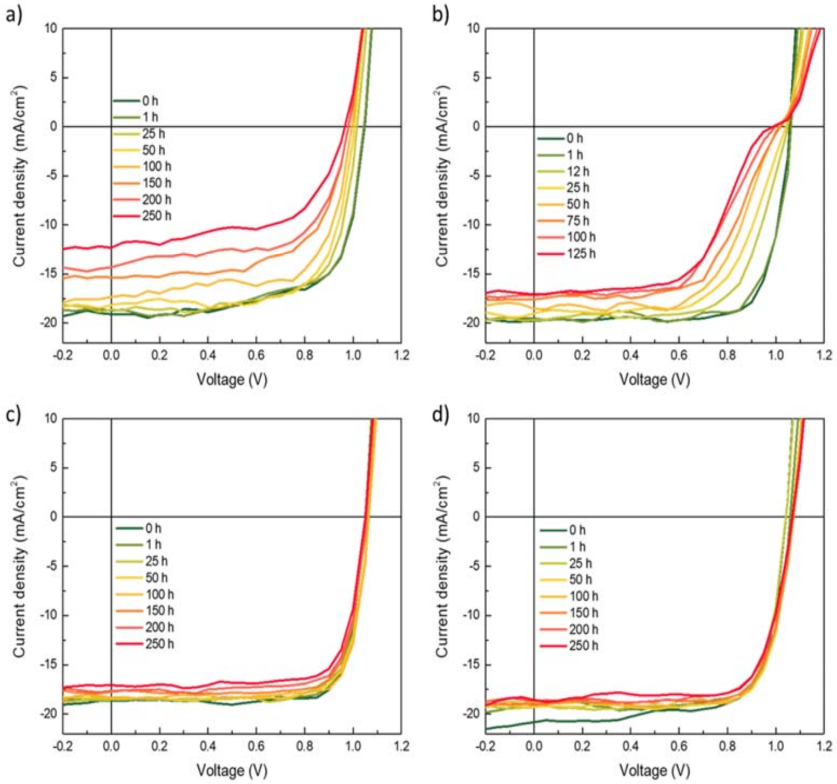

Figure S5 J-V curves measured at various times under continuous illumination for devices A(a), C(b), D(c) and E(d).

Annex B – Chapter 4 reference:

Ruthenium pentamethylcyclopentadienyl mesitylene dimer: a sublimable n-dopant and electron buffer layer for efficient n–i–p perovskite solar cells.

Journal of
Materials Chemistry A

COMMUNICATION

View Article Online
View Journal | View Issue

Cite this: *J. Mater. Chem. A*, 2019, **7**, 25796

Received 5th September 2019
Accepted 30th October 2019

DOI: 10.1039/c9ta09838k

rsc.li/materials-a

Published on 30 October 2019. Downloaded by Universitat de València on 4/10/2020 2:54:03 PM.

Ruthenium pentamethylcyclopentadienyl mesitylene dimer: a sublimable n-dopant and electron buffer layer for efficient n–i–p perovskite solar cells†

Jorge Avila,[a] Maria-Grazia La-Placa,[a] Elena Longhi,[b] Michele Sessolo,*[a] Stephen Barlow,[b] Seth R. Marder[b] and Henk J. Bolink[a]

Electron-transport materials such as fullerenes are widely used in perovskite solar cells to selectively transfer the photogenerated electrons to the electrodes. In order to minimize losses at the interface between the fullerene and the electrode, it is important to reduce the energy difference between the transport level of the two materials. A common approach to reduce such energy mismatch is to increase the charge carrier density in the semiconductor through doping. A variety of molecular dopants have been reported to reduce (n-dope) fullerenes. However, most of them are either difficult to process or extremely air sensitive, with most n-dopants leading to the formation of undesirable side products. Dimers formed by 19-electron organometallic sandwich compounds combine strong reducing ability, clean reactivity, and moderate air stability, while being processable both from solution and in vacuum. In this work, we have investigated the use of pentamethylcyclopentadienyl mesitylene ruthenium dimer, $(RuCp^*mes)_2$, as a dopant for C_{60} in fully vacuum-deposited n–i–p perovskite solar cells. The $(RuCp^*mes)_2$ was either co-evaporated with the fullerene or deposited as a pure thin film on top of the transparent electrode prior to the deposition of the fullerene. It was found that both the co-evaporated blends and the bilayers are effective electron-transport layers, leading to solar cells with efficiencies up to 18%.

Introduction

Lead-halide perovskite solar cells have emerged as a promising alternative thin-film photovoltaic (PV) technology.[1–5] The potential of perovskite PV is demonstrated by the constantly increasing record efficiencies, now exceeding 25%.[6,7] The most efficient perovskite solar cells reported so far have in common the use of TiO_2 as the electron-transport material (ETM).[8,9] These devices are built in an n–i–p architecture, where the ETM is deposited on top of the transparent conductive oxide (TCO) electrode. Some alternative ETMs have been explored, both inorganic – most notably SnO_2 – and organic.[10–14] Among organic semiconductors, fullerene derivatives are widely employed as the ETM in perovskite solar cells, as they provide an ohmic contact with common perovskite absorbers, reducing non-radiative recombination and hysteresis while maintaining a high fill factor (FF).[15–17] In particular, the simplest fullerene, C_{60}, is extensively used in efficient devices and has advantages over chemically modified fullerenes in terms of cost and vacuum processibility.[18–20]

In order to ensure efficient charge extraction from the ETM to the TCO, the alignment of their energy levels and hence a low energetic barrier at the interface is crucial. The large energy difference between the electron affinity of C_{60} and the work function of ITO results in a Schottky barrier height of about 0.8 eV, which leads to a non-ohmic interface, limiting the charge extraction. A common approach to reduce the energy mismatch between a semiconductor and an electrode, and thus reduce ohmic losses, is to increase the charge-carrier density in the organic semiconductor through doping. As a consequence, the Fermi level in the doped semiconductor will shift towards the filled states, reducing the barrier height and favoring charge transfer.[21] In particular, this can be achieved by depositing a thin layer of n-doped C_{60} in between the intrinsic C_{60} and the TCO.[20] In order to prevent intermixing of the doped and intrinsic C_{60} during processing, which would increase non-radiative recombination at the perovskite/doped ETL interface, sequential vacuum sublimation is the most suitable deposition method.[22]

A variety of molecular dopants have been reported to reduce (n-dope) C_{60} and other fullerenes. Examples of one-electron reducing agents are cobaltocene and $W_2(hpp)_4$;[23,24] however, the first is too volatile for standard high vacuum processing,[25] while the latter is extremely air sensitive. Alternative, more stable reductants include halide salts of organic aromatic cations, from which the corresponding organic radicals can be

---

[a] *Instituto de Ciencia Molecular, Universidad de Valencia, C/ J. Beltrán 2, 46980, Paterna, Spain. E-mail: michele.sessolo@uv.es*

[b] *School of Chemistry and Biochemistry and Center for Organic Photonics and Electronics, Georgia Institute of Technology, Atlanta, GA 30332, USA*

† Electronic supplementary information (ESI) available: Materials and methods, perovskite XRD, optical absorption and SEM. See DOI: 10.1039/c9ta09838k

This journal is © The Royal Society of Chemistry 2019

Published on 30 October 2019. Downloaded by Universitat de València on 4/10/2020 2:54:03 PM.

sublimed,[26,27] hydride-donating molecules,[28,29] alkylamine-containing compounds,[30,31] and tetrabutylammonium salts of halides and other simple anions.[32] Several of these molecules have been applied to fullerene doping in perovskite solar cells, increasing the efficiency as compared to that of devices using undoped C_{60} ETMs. The hydride donor 1,3-dimethyl-2(4-(diphenylamino)phenyl)-2,3-dihydro-1*H*-benzoimidazole has been used for the bulk doping of solution-processed C_{60} ETM films.[33] Sequential solution deposition of C_{60} and poly(allylamine) followed by annealing, leads to n-doping of the ETM as well as to the formation of N–C_{60} covalent bonds.[34] However, some of these dopants can lead to the formation of undesirable side products in addition to the fullerene radical anion,[35–37] while others can only be processed from solution.

Dimers formed by some 19-electron organometallic sandwich compounds (as well as those formed by some organic radicals)[38] combine strong reducing ability, clean reactivity (forming solely the corresponding monomeric cations upon doping), and moderate air stability, while being processable both from solution and in vacuum. In view of these favorable properties, they have been used to n-dope a wide variety of semiconductors, including fullerenes.[38–41] Of most relevance to the present work, a thin layer of one such organometallic dimer – pentamethylrhodocene dimer, $(RhCp^*Cp)_2$ – has been vacuum deposited between FTO and vacuum-deposited ETMs, pinning the Fermi level to the lowest unoccupied molecular orbital (LUMO) of the C_{60}.[42] In this work, we have investigated the use of a similar organometallic compound – pentamethylcyclopentadienyl mesitylene ruthenium dimer,[43] $(RuCp^*mes)_2$ – to dope C_{60} in fully vacuum deposited n–i–p perovskite solar cells. $(RuCp^*mes)_2$ has been shown to passivate traps in C_{60} at low concentration and to change the semiconductor work function and highest occupied molecular orbital (HOMO) position with respect to the Fermi level upon doping.[40] The cells were fabricated using a procedure that was described by some of us previously.[20]

In order to evaluate the potential of $(RuCp^*mes)_2$ as an n-dopant for C_{60} in perovskite solar cells, several devices with different architectures have been fabricated. An intrinsic advantage of vacuum deposition is the possibility of selectively modifying and/or exchanging any layer in the device stack, and of studying the consequences for the device performance. The $(RuCp^*mes)_2$ was either co-evaporated with the C_{60} or deposited as a pure thin film on top of the TCO (indium tin oxide, ITO) prior to the deposition of C_{60}. It was found that both the co-evaporated blend of C_{60}:$(RuCp^*mes)_2$ and the bilayer $(RuCp^*mes)_2$/C_{60} are effective electron transport layers (ETLs), leading to power conversion efficiencies in the range of 17–18%.

Results

The dimer $(RuCp^*mes)_2$ was synthesized following previously published protocols.[44] We initially examined whether $(RuCp^*mes)_2$ is an effective dopant for C_{60}, looking at the optical absorption spectra and conductivity (Fig. 2) of C_{60} and $(RuCp^*mes)_2$ in different layer configurations. For pure thin films of C_{60} and $(RuCp^*mes)_2$, the measured conductivities are on the order of 10^{-8} S cm^{-1}, as expected for intrinsic and highly pure organic semiconductors. To evaluate the reactivity among the two materials we followed two approaches. In one, both materials were co-sublimed at the same time leading to a homogeneous C_{60}:$(RuCp^*mes)_2$ layer (20 nm, dopant concentration 12.5 wt%). In the other approach we deposited a bilayer formed by a thin film of $(RuCp^*mes)_2$ (2.5 nm) covered by C_{60} (10 nm). In this case the contact and hence the eventual reaction between the materials presumably occurs mainly at the interface between them. In both cases we observed a large increase in conductivity (up to 0.5 S cm^{-1} for the co-deposited film, Fig. 2a), indicating that $(RuCp^*mes)_2$ can indeed efficiently dope C_{60}, even when the materials are in contact only at the interface. This is in agreement with the strong reducing character of $(RuCp^*mes)_2$, which is easily capable of n-doping a large variety of organic semiconductors.[39,45,46] We note, however, that the large conductivity in the latter case might indicate some interdiffusion between the two materials (as neutral molecules and/or ions), although of course the amount

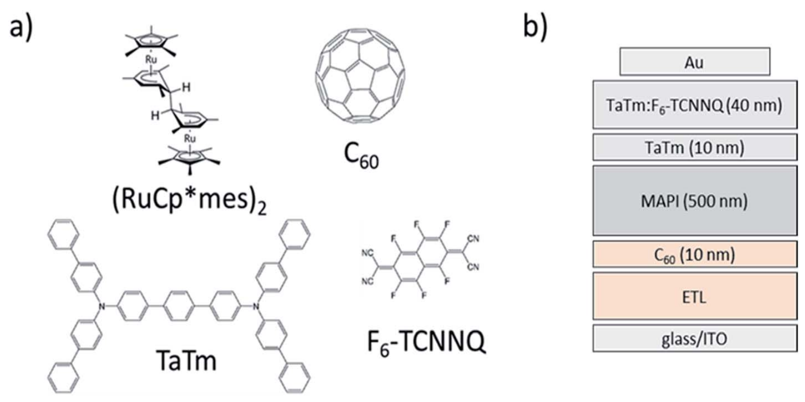

Fig. 1 (a) Chemical structures of transport materials used in the devices. C_{60} is the electron-transport material together with $(RuCp^*mes)_2$ as n-dopant. TaTm is the hole transport material and F_6-TCNNQ is the p-dopant. (b) Schematics of the vacuum-processed perovskite solar cells, where the ETL is either a thin $(RuCp^*mes)_2$ layer or a co-evaporated C_{60}:$(RuCp^*mes)_2$ film.

Published on 30 October 2019. Downloaded by Universitat de València on 4/10/2020 2:54:03 PM.

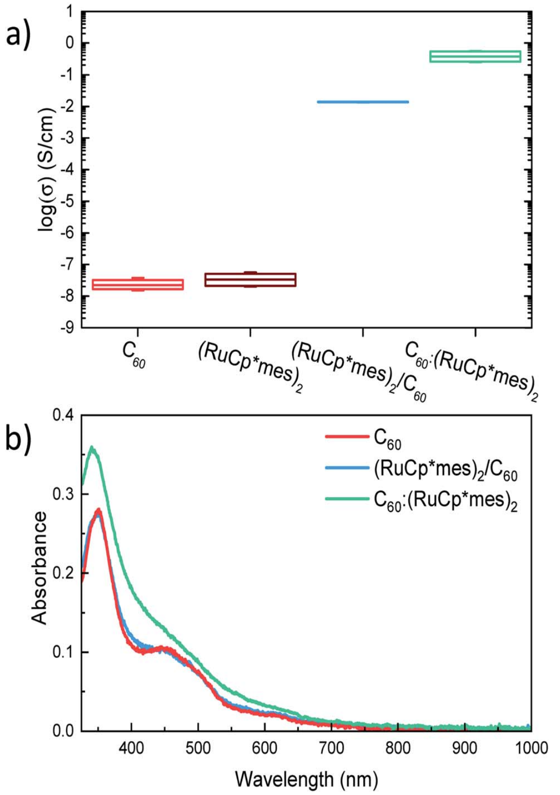

Fig. 2 (a) Conductivity and (b) absorption spectra of different electron transport layers. C_{60}, $(RuCp^*mes)_2$ and C_{60}:$(RuCp^*mes)_2$ films are 10 nm, 2.5 nm and 20 nm thick, respectively.

of the dimers that react and the extent to which dopants diffuse into the C_{60} is not known. From the absorption spectra of C_{60} and of the two doped layers (Fig. 2b) we can observe slightly higher absorbance for the n-doped C_{60} films, with only minor differences between the bi-layer and the co-deposited film. Also, the optical absorption profiles are similar to that of the pure fullerene, without the presence of any new relevant features, indicating that, at these $(RuCp^*mes)_2$ concentration and film thickness, a significant improvement in the conductivity can be obtained without introducing undesirable parasitic absorption.

Thereafter we investigated the performance of the same films in perovskite solar cells. As a first step, we studied devices with the co-sublimed C_{60}:$(RuCp^*mes)_2$ layer. The chosen device architecture was an n–i–p configuration where the ETL is directly deposited on top of the glass/ITO front contact. The layout of the devices is as follows: ITO/ETL/C_{60} (10 nm)/MAPI (500 nm)/TaTm (10 nm)/TaTm:F_6-TCNNQ (40 nm)/Au, where the ETL is a co-evaporated C_{60}:$(RuCp^*mes)_2$ (20 nm), MAPI is methylammonium lead iodide, TaTm is $N^4,N^4,N^{4''},N^{4''}$-tetra([1,1′-biphenyl]-4-yl)-[1,1′:4′,1″-terphenyl]-4,4″-diamine and its p-dopant F_6-TCNNQ is 2,2′-(perfluoronaphthalene-2,6-diylidene)di-malononitrile. The MAPI films were characterized by X-ray diffraction, optical absorption and electron microscopy to verify the material quality. The characterization of a MAPI film (Fig. S1†), together with a detailed description of the device fabrication, can be found in the ESI.†

The current density *vs.* voltage (*J*–*V*) curve for the solar cell employing C_{60} with 12.5 wt% dopant concentration as the ETM shows excellent carrier extraction (FF of approximately 80%) and an open circuit voltage (V_{oc}) of 1.07 V. Together with the short circuit current density (J_{sc}) of 19.8 mA cm^{-2}, these values result in a power conversion efficiency (PCE) of 16.9% (characteristic parameters are reported in Table 1). Decreasing the dopant concentration to 6.25 wt% does not significantly change the FF (81%) or the V_{oc} (only slightly lower at 1.06 V), while it results in a small increase of J_{sc} to 20.6 mA cm^{-2}. Hence the PCE of the cell is enhanced to 17.7%, notably with negligible hysteresis. However, when the dopant concentration is further diminished to 2.5 wt%, the corresponding *J*–*V* curve shows a pronounced s-shape with poor FF (63%), indicative of an inefficient charge collection at the front contact. At this dopant concentration, the C_{60}:$(RuCp^*mes)_2$ layer is no longer able to effectively reduce the interface energy barrier, increasing the recombination losses (V_{oc} is diminished to 1.02 V). The *J*–*V* curve shows also hysteresis between the forward (from short to open circuit) and reverse (from open to short circuit) scans, indicating charge accumulation at the non-ohmic ITO/ETL interface. The observed trend in the FF correlates with the electrical conductivity of the C_{60}:$(RuCp^*mes)_2$ ETL (Fig. 3b), which decreases from about 0.5 S cm^{-1} for a dopant concentration of 12.5 wt% to about 0.05–0.1 S cm^{-1} for the lowest concentration of 2.5 wt%. In comparison with a previous report,[20] the conductivity of the ETL with dopant concentration of 2.5 wt% should be sufficiently high to guarantee efficient charge collection. However, the low performance observed here indicates that this dopant concentration is unable to effectively

Table 1 *J*–*V* parameters of the best devices for each configuration measured under simulated solar illumination; no difference between forward and reverse scans was observed

ETL	Dopant concentration	PCE (%)	V_{oc} (V)	J_{sc} (mA cm^{-2})	FF (%)
C_{60}:$(RuCp^*mes)_2$ (20 nm)	12.5 wt%	16.9	1.07	19.8	80
	6.25 wt%	17.7	1.06	20.6	81
	2.5 wt%	12.5	1.02	19.5	63
Without ETL	—	2.6	0.82	13.6	23
$(RuCp^*mes)_2$ (1 nm)	—	17.1	1.09	20.1	78
$(RuCp^*mes)_2$ (2.5 nm)	—	3.1	0.96	13.5	24

This journal is © The Royal Society of Chemistry 2019

Published on 30 October 2019. Downloaded by Universitat de València on 4/10/2020 2:54:03 PM.

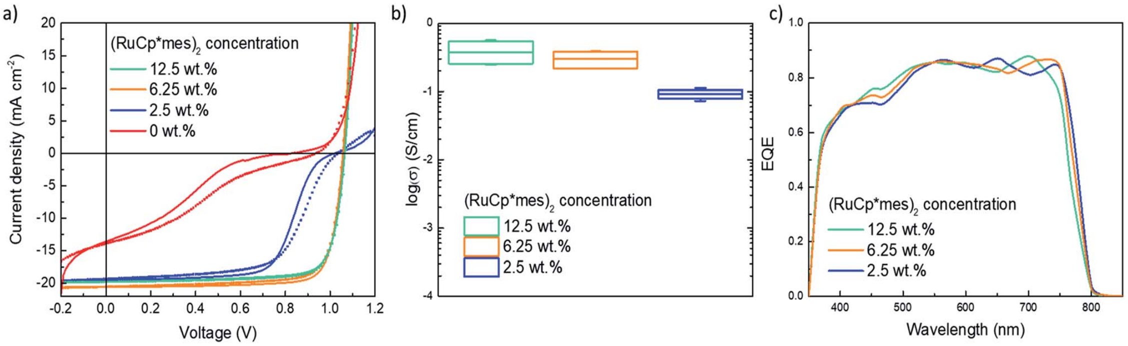

Fig. 3 (a) Representative *J*–*V* curves measured under simulated 1 sun illumination in forward (straight line) and reverse (dotted line) scan direction for each studied device. (b) Electrical conductivity of the electron-transport layers used in each device. (c) External quantum efficiency (EQE) spectra for the same device series.

reduce the energy mismatch between the ITO and C_{60}, leading to low FF and poorly working devices.

The differences in the current density observed with decreasing dopant concentrations are likely related with different degrees of parasitic absorption due to the doped fullerene. In the external quantum efficiency (EQE) spectra (Fig. 3c), the main feature is a decrease in charge generation around 450 nm when the concentration of dopant is reduced or, in other words, when the relative amount of C_{60} increases. We can correlate the loss in charge generation in the 400–500 nm range with the intense absorption of C_{60} in this spectral region (Fig. 2b). Overall, the EQE spectrum for the device with a dopant concentration of 6.25 wt% leads to the highest integrated current density, in line with the best performance among the device series (Table 1).

We then prepared devices to study the effect of a pure layer of $(RuCp^*mes)_2$ deposited in between the ITO electrode and the C_{60}. The architecture was an n–i–p configuration similar to that previously discussed (ITO/ETL/C_{60} (10 nm)/MAPI (500 nm)/TaTm (10 nm)/TaTm:F_6-TCNNQ (40 nm)/Au). We prepared additional diodes without the dopant interlayer as a reference, where C_{60} is directly in contact with ITO.

The representative *J*–*V* curves for this device series are represented in Fig. 4a. As expected, the solar cells with the bare ITO/C_{60} front contact shows a very low FF and a low V_{oc} (23% and 0.82 V, respectively). The energy barrier results in non-ohmic charge extraction, reducing the FF and causing non-radiative recombination losses limiting the maximum achievable V_{oc}. Interestingly, when a very thin layer of $(RuCp^*mes)_2$ (1 nm) is introduced between the ITO electrode and C_{60}, the device performance is recovered, with good rectification (FF = 78%) and V_{oc} as high as 1.09 V. Taking into account the photocurrent density ($J_{sc} = 20.1$ mA cm^{-2}), we obtained a PCE exceeding 17%. We observed performance similar to the cells with n-doped C_{60}, but with an increase in V_{oc} (30 mV) in the case of the pure dopant layer. This indicates that avoiding the use of doped layers can limit the recombination losses leading to enhanced photovoltage. Nevertheless, if the thickness of the thin $(RuCp^*mes)_2$ layer is slightly increased to 2.5 nm, the device shows again hindered charge extraction and low photovoltage, with FF and V_{oc} similar to those measured for the device with only the fullerene as ETM. This behavior suggests a very low electron mobility in the pure $(RuCp^*mes)_2$, which is now essentially blocking the carrier collection. This is somewhat

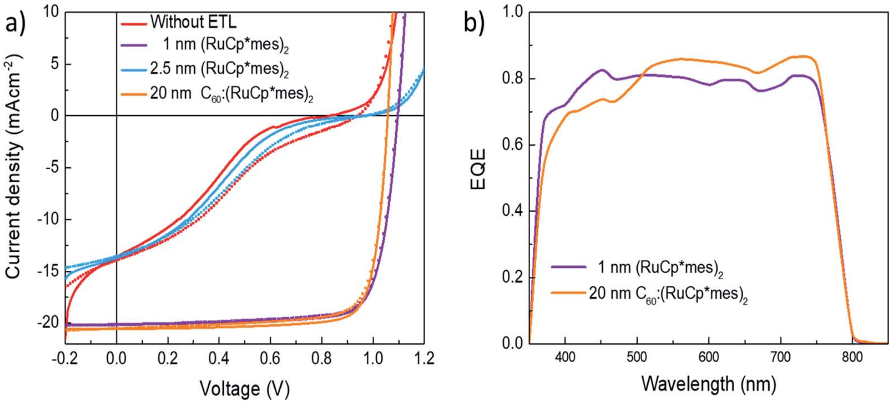

Fig. 4 (a) Representative *J*–*V* characteristics measured under simulated solar illumination in forward (straight line) and reverse (dotted line) scan direction for devices employing different ETL. (b) External quantum efficiency (EQE) spectra for the devices with $(RuCp^*mes)_2$ and C_{60}-:$(RuCp^*mes)_2$ as the ETL.

Published on 30 October 2019. Downloaded by Universitat de València on 4/10/2020 2:54:03 PM.

different to what was previously observed for $(RhCp^*Cp)_2/C_{60}$, where devices with a nominal interlayer thickness of 10 nm resulted in large V_{oc} and FF.[42] We believe that the differences may originate from different diffusivity of the two organometallic dopants into the C_{60}, as well as from the lower work function of FTO used in the previous work, which would favor electron extraction. In Fig. 4b we can observe similar EQE spectra for the devices using the two types of ETL architectures, the co-evaporated C_{60}:$(RuCp^*mes)_2$ and the bilayer $(RuCp^*mes)_2/C_{60}$, with EQE values of about 0.8 over the whole spectral range, indicating that the small parasitic absorptions (Fig. 1b) have negligible impact on carrier generation. Nevertheless, the device with doped C_{60} exhibits a slightly lower EQE in the blue region of the spectrum. This difference correlates with the ETL thicknesses, as the devices with doped C_{60} have a total ETL thickness of 30 nm resulting in larger parasitic absorption.

Conclusions

In conclusion, we have successfully demonstrated the use of $(RuCp^*mes)_2$ as a n-dopant for C_{60} in vacuum-deposited perovskite solar cells. It was found that both co-evaporated C_{60}:$(RuCp^*mes)_2$ films and $(RuCp^*mes)_2/C_{60}$ bilayers can perform as effective electron-transport layers (ETLs). The simultaneous sublimation of both materials allows to obtain homogeneous layers that form ohmic contact between ITO and the intrinsic fullerene, resulting in efficient and selective charge extraction. Optimization of the dopant concentration allowed the fabrication of solar cells with power conversion efficiency approaching 18%. The thickness of the $(RuCp^*mes)_2$ in the bilayer $(RuCp^*mes)_2/C_{60}$ ETL architecture was found to be critical for the device performance. Very thin dopant layers, around 1 nm, were needed to guarantee efficient charge collection, and resulted in efficiencies exceeding 17%. We observed a higher V_{oc} for solar cells using the bilayer $(RuCp^*mes)_2/C_{60}$ ETL, which is a consequence of the diminished charge recombination compared to doped layers.

Conflicts of interest

There are no conflicts to declare.

Acknowledgements

The research leading to these results has received funding from the European Union's Horizon 2020 research and innovation programme under grant agreement No. 763977 of the PerTPV project. We acknowledge financial support from the the Spanish Ministry of Economy and Competitiveness (MINECO) *via* the Unidad de Excelencia María de Maeztu MDM-2015-0538, MAT2017-88821-R, PCIN-2015-255 and MAT2017-88905-P, the Generalitat Valenciana (Prometeo/2016/135), the U. S. National Science Foundation (DMR-1305247 and DMR-1807797), and the U. S. Air Force Office of Scientific Research (FA9550-18-1-0499). H. B. acknowledges the support of ERA NET PCIN-2017-014. M.S. thanks the MINECO for his RyC contract. J. Á. thanks the Spanish Ministry of Education, Culture and Sport for his pre-doctoral grant (FPU14/04466).

References

1 A. Kojima, K. Teshima, Y. Shirai and T. Miyasaka, *J. Am. Chem. Soc.*, 2009, **131**, 6050–6051.
2 H.-S. Kim, C.-R. Lee, J.-H. Im, K.-B. Lee, T. Moehl, A. Marchioro, S.-J. Moon, R. Humphry-Baker, J.-H. Yum, J. E. Moser, M. Grätzel and N.-G. Park, *Sci. Rep.*, 2012, **2**, 1–7.
3 M. M. Lee, J. Teuscher, T. Miyasaka, T. N. Murakami and H. J. Snaith, *Science*, 2012, **338**, 643–647.
4 T. Leijtens, K. A. Bush, R. Prasanna and M. D. McGehee, *Nat. Energy*, 2018, **3**, 828–838.
5 Z. Li, T. R. Klein, D. H. Kim, M. Yang, J. J. Berry, M. F. A. M. van Hest and K. Zhu, *Nat. Rev. Mater.*, 2018, **3**, 18017.
6 Natl. Renew. Energy Lab., 2019, https://www.nrel.gov/pv/cell-efficiency.html.
7 M. A. Green, Y. Hishikawa, E. D. Dunlop, D. H. Levi, J. Hohl-Ebinger, M. Yoshita and A. W. Y. Ho-Baillie, *Prog. Photovolt: Res. Appl.*, 2019, **27**, 3–12.
8 W. S. Yang, B.-W. Park, E. H. Jung, N. J. Jeon, Y. C. Kim, D. U. Lee, S. S. Shin, J. Seo, E. K. Kim, J. H. Noh and S. Il Seok, *Science*, 2017, **356**, 1376–1379.
9 E. H. Jung, N. J. Jeon, E. Y. Park, C. S. Moon, T. J. Shin, T.-Y. Yang, J. H. Noh and J. Seo, *Nature*, 2019, **567**, 511–515.
10 Z. Zhu, J. Q. Xu, C. C. Chueh, H. Liu, Z. Li, X. Li, H. Chen and A. K. Y. Jen, *Adv. Mater.*, 2016, **28**, 10786–10793.
11 C. Sun, Z. Wu, H. L. Yip, H. Zhang, X. F. Jiang, Q. Xue, Z. Hu, Z. Hu, Y. Shen, M. Wang, F. Huang and Y. Cao, *Adv. Energy Mater.*, 2016, **6**, 1–10.
12 D. Zhao, Z. Zhu, M. Y. Kuo, C. C. Chueh and A. K. Y. Jen, *Angew. Chem., Int. Ed.*, 2016, **55**, 8999–9003.
13 K. Mahmood, S. Sarwar and M. T. Mehran, *RSC Adv.*, 2017, **7**, 17044–17062.
14 S.-H. Turren-Cruz, A. Hagfeldt and M. Saliba, *Science*, 2018, **362**, 449–453.
15 K. Wojciechowski, I. Ramirez, T. Gorisse, O. Dautel, R. Dasari, N. Sakai, J. M. Hardigree, S. Song, S. Marder, M. Riede, G. Wantz and H. J. Snaith, *ACS Energy Lett.*, 2016, **1**, 648–653.
16 D. P. McMeekin, Z. Wang, W. Rehman, F. Pulvirenti, J. B. Patel, N. K. Noel, M. B. Johnston, S. R. Marder, L. M. Herz and H. J. Snaith, *Adv. Mater.*, 2017, **29**, 1607039.
17 J. B. Patel, J. Wong-Leung, S. Van Reenen, N. Sakai, J. T. W. Wang, E. S. Parrott, M. Liu, H. J. Snaith, L. M. Herz and M. B. Johnston, *Adv. Electron. Mater.*, 2016, 1600470.
18 V. O. Eze, Y. Seike and T. Mori, *Org. Electron.*, 2017, **46**, 253–262.
19 D. Liu, Q. Wang, C. J. Traverse, C. Yang, M. Young, P. S. Kuttipillai, S. Y. Lunt, T. W. Hamann and R. R. Lunt, *ACS Nano*, 2018, **12**, 876–883.
20 C. Momblona, L. Gil-Escrig, E. Bandiello, E. M. Hutter, M. Sessolo, K. Lederer, J. Blochwitz-Nimoth and H. J. Bolink, *Energy Environ. Sci.*, 2016, **9**, 3456–3463.

This journal is © The Royal Society of Chemistry 2019

Published on 30 October 2019. Downloaded by Universitat de València on 4/10/2020 2:54:03 PM.

21 K. Walzer, B. Maennig, M. Pfeiffer and K. Leo, *Chem. Rev.*, 2007, **107**, 1233–1271.

22 M. Schwarze, C. Gaul, R. Scholz, F. Bussolotti, A. Hofacker, K. S. Schellhammer, B. Nell, B. D. Naab, Z. Bao, D. Spoltore, K. Vandewal, J. Widmer, S. Kera, N. Ueno, F. Ortmann and K. Leo, *Nat. Mater.*, 2019, **18**, 242–248.

23 F. J. Rizzuto, D. M. Wood, T. K. Ronson and J. R. Nitschke, *J. Am. Chem. Soc.*, 2017, **139**, 11008–11011.

24 T. Menke, D. Ray, J. Meiss, K. Leo and M. Riede, *Appl. Phys. Lett.*, 2012, **100**, 093304.

25 C. K. Chan, F. Amy, Q. Zhang, S. Barlow, S. Marder and A. Kahn, *Chem. Phys. Lett.*, 2006, **431**, 67–71.

26 A. G. Werner, F. Li, K. Harada, M. Pfeiffer, T. Fritz and K. Leo, *Appl. Phys. Lett.*, 2003, **82**, 4495–4497.

27 P. Wei, T. Menke, B. D. Naab, K. Leo, M. Riede and Z. Bao, *J. Am. Chem. Soc.*, 2012, **134**, 3999–4002.

28 F. Li, A. Werner, M. Pfeiffer, K. Leo and X. Liu, *J. Phys. Chem. B*, 2004, **108**, 17076–17082.

29 P. Wei, J. H. Oh, G. Dong and Z. Bao, *J. Am. Chem. Soc.*, 2010, **132**, 8852–8853.

30 S. Fabiano, S. Braun, X. Liu, E. Weverberghs, P. Gerbaux, M. Fahlman, M. Berggren and X. Crispin, *Adv. Mater.*, 2014, **26**, 6000–6006.

31 B. Russ, M. J. Robb, B. C. Popere, E. E. Perry, C. Mai, S. L. Fronk, S. N. Patel, T. E. Mates, G. C. Bazan, J. J. Urban, M. L. Chabinyc, C. J. Hawker and R. A. Segalman, *Chem. Sci.*, 2016, **7**, 1914–1919.

32 C.-Z. Li, C.-C. Chueh, F. Ding, H.-L. Yip, P.-W. Liang, X. Li and A. K.-Y. Jen, *Adv. Mater.*, 2013, **25**, 4425–4430.

33 Z. Wang, D. P. McMeekin, N. Sakai, S. van Reenen, K. Wojciechowski, J. B. Patel, M. B. Johnston and H. J. Snaith, *Adv. Mater.*, 2017, **29**, 1604186.

34 S. Song, R. Hill, K. Choi, K. Wojciechowski, S. Barlow, J. Leisen, H. J. Snaith, S. R. Marder and T. Park, *Nano Energy*, 2018, **49**, 324–332.

35 M. Schwarze, B. D. Naab, M. L. Tietze, R. Scholz, P. Pahner, F. Bussolotti, S. Kera, D. Kasemann, Z. Bao and K. Leo, *ACS Appl. Mater. Interfaces*, 2018, **10**, 1340–1346.

36 B. D. Naab, S. Guo, S. Olthof, E. G. B. Evans, P. Wei, G. L. Millhauser, A. Kahn, S. Barlow, S. R. Marder and Z. Bao, *J. Am. Chem. Soc.*, 2013, **135**, 15018–15025.

37 C. D. Weber, C. Bradley and M. C. Lonergan, *J. Mater. Chem. A*, 2014, **2**, 303–307.

38 B. D. Naab, S. Zhang, K. Vandewal, A. Salleo, S. Barlow, S. R. Marder and Z. Bao, *Adv. Mater.*, 2014, **26**, 4268–4272.

39 S. Guo, S. B. Kim, S. K. Mohapatra, Y. Qi, T. Sajoto, A. Kahn, S. R. Marder and S. Barlow, *Adv. Mater.*, 2012, **24**, 699–703.

40 S. Olthof, S. Mehraeen, S. K. Mohapatra, S. Barlow, V. Coropceanu, J.-L. Brédas, S. R. Marder and A. Kahn, *Phys. Rev. Lett.*, 2012, **109**, 176601.

41 P. J. Smith and C. K. Mann, *J. Org. Chem.*, 1969, **34**, 1821–1826.

42 F. Pulvirenti, B. Wegner, N. K. Noel, G. Mazzotta, R. Hill, J. B. Patel, L. M. Herz, M. B. Johnston, M. K. Riede, H. J. Snaith, N. Koch, S. Barlow and S. R. Marder, *Mol. Syst. Des. Eng.*, 2018, **3**, 741–747.

43 O. V Gusev, M. A. Ievlev, M. G. Peterleitner, S. M. Peregudova, L. I. Denisovich, P. V Petrovskii and N. A. Ustynyuk, *J. Organomet. Chem.*, 1997, **534**, 57–66.

44 H.-I. Un, S. A. Gregory, S. K. Mohapatra, M. Xiong, E. Longhi, Y. Lu, S. Rigin, S. Jhulki, C.-Y. Yang, T. V Timofeeva, J.-Y. Wang, S. K. Yee, S. Barlow, S. R. Marder and J. Pei, *Adv. Energy Mater.*, 2019, **9**, 1900817.

45 S. Guo, S. K. Mohapatra, A. Romanov, T. V Timofeeva, K. I. Hardcastle, K. Yesudas, C. Risko, J.-L. Brédas, S. R. Marder and S. Barlow, *Chem.–Eur. J.*, 2012, **18**, 14760–14772.

46 S. K. Mohapatra, A. Fonari, C. Risko, K. Yesudas, K. Moudgil, J. H. Delcamp, T. V Timofeeva, J.-L. Brédas, S. R. Marder and S. Barlow, *Chem.–Eur. J.*, 2014, **20**, 15385–15394.

This journal is © The Royal Society of Chemistry 2019

Electronic Supplementary Material (ESI) for Journal of Materials Chemistry A.
This journal is © The Royal Society of Chemistry 2019

Supporting Information

Ruthenium pentamethylcyclopentadienyl mesitylene dimer: a sublimable n-dopant and electron buffer layer for efficient n-i-p perovskite solar cells

Jorge Avila[1], Maria-Grazia La-Placa[1], Michele Sessolo[1], Elena Longhi[2], Stephen Barlow[2], Seth R. Marder[2], and Henk J. Bolink*[1]

[1]*Instituto de Ciencia Molecular, Universidad de Valencia, C/ J. Beltrán 2, 46980, Paterna, Spain. E/mail: michele.sessolo@uv.es*

[2]*School of Chemistry and Biochemistry and Center for Organic Photonics and Electronics, Georgia Institute of Technology, Atlanta, GA 30332, United States*

Supporting Information

Materials. Photolithographically patterned ITO coated glass substrates were purchased from Naranjo Substrates (www.naranjosubstrates.com). 2,2'-(Perfluoronaphthalene-2,6-diylidene) dimalononitrile (F_6-TCNNQ) and N4,N4,N4",N4"-tetra([1,1'-biphenyl]-4-yl)-[1,1':4',1"-terphenyl]-4,4"-diamine (TaTm) were provided from Novaled GmbH. Fullerene (C_{60}) was purchased from sigma Aldrich. PbI_2 was purchased from Tokyo Chemical Industry CO (TCI), and CH_3NH_3I (MAI) from Lumtec**.** RuCp*mes$)_2$ was synthesized as recently reported.[1–3]

Device preparation. ITO-coated glass substrates were subsequently cleaned with soap, water and isopropanol in an ultrasonic bath, followed by UV-ozone treatment. They were transferred to a vacuum chamber integrated into a nitrogen-filled glovebox (MBraun, H_2O and O_2 < 0.1 ppm) and evacuated to a pressure of 10^{-6} mbar. The vacuum chamber uses a turbomolecular pump (Pfeiffer TMH 261P, DN 100 ISO-K, 3P) coupled to a scroll pump. The vacuum chamber is equipped with six temperature controlled evaporation sources (Creaphys) fitted with ceramic crucibles. The sources were directed upwards with an angle of approximately 90º with respect to the bottom of the evaporator. The substrate holder to evaporation sources distance is approximately 20 cm. Three quartz crystal microbalance (QCM) sensors are used, two monitoring the deposition rate of each evaporation source and a third one close to the substrate holder monitoring the total deposition rate. For thickness calibration, we first individually sublimed the charge transport materials and their dopants (TaTm and F_6-TCNNQ, C_{60} and $(RuCp^*mes)_2$). A calibration factor was obtained by comparing the thickness inferred from the QCM sensors with that measured with a mechanical profilometer (Ambios XP1). Then these materials were co-sublimed at temperatures ranging from 135-160 ºC for the dopants to 250 ºC for the pure charge transport molecules, and the evaporation rate was controlled by separate QCM sensors and adjusted to obtain the desired doping concentration. In general, the deposition rate for TaTm and C_{60} was kept constant at 0.8 Å s^{-1} while varying the deposition rate of the dopants during co-deposition. Pure TaTm, C_{60}, and $(RuCp^*mes)_2$ layers were deposited at a rate of 0.5 Å s^{-1}.

The samples for conductivity measurements were deposited on interdigitated ITO and for absorbance measurements on glass substrate. The materials and thicknesses for each sample are: One sample with 10 nm of C_{60}, one sample with 2.5 nm of $(RuCp^*mes)_2$, one sample with the bilayer $(RuCp^*mes)_2/C_{60}$ (2.5 nm/10 nm), and one sample with co-sublimed $C_{60}:(RuCp^*mes)_2$ (10 nm 12.5wt%).

For devices with different concentration of dopant (12.5wt%, 6.26wt% and 2.5wt%), 20 nm of the n-doped electron-transport layer (C_{60}: $(RuCp^*mes)_2$) capped with 10 nm of the pure C_{60} were deposited. For devices with a thin layer of dopant between ITO and C_{60}, a thin (1 nm or 2.5 nm) layer of the molecule $(RuCp^*mes)_2$ is deposited on top of the ITO prior to depositing the layer of C_{60} (10 nm). For the device with C_{60} directly on top of ITO, only 10 nm of pure C_{60} was evaporated. Once completed this deposition, the chamber was vented with dry N_2 to replace the ETL crucibles with those containing the starting materials for the perovskite deposition, PbI_2, and CH_3NH_3I. The vacuum chamber was evacuated again to a pressure of 10^{-6} mbar, and the perovskite films were then obtained by co-deposition of the two precursors. The use of clean QCM sensors for the perovskite evaporation is important to avoid false readings due to perovskite formation on the sensor. For a more accurate deposition the density of PbI_2 (6.16 g/cm^3) is set in the equipment. For CH_3NH_3I the density is assumed to be 1 g/cm^3. And the z-factor for both materials is set to 1. The calibration of the deposition rate for the CH_3NH_3I was found to be difficult due to non-uniform layers and the soft nature of the material, which impeded accurate thickness measurements. Hence, the source temperature of the CH_3NH_3I was kept constant at 70 ºC and the $CH_3NH_3I:PbI_2$ ratio was controlled off line using grazing incident x-ray diffraction by adjusting the PbI_2 deposition temperature. The optimum deposition temperatures were found to be 250 ºC for the PbI_2 and 70 ºC for the CH_3NH_3I. After deposition of a 500 nm thick perovskite film, the chamber was vented, and the crucibles replaced with those containing the hole-transport materials and evacuated again to a pressure of 10^{-6} mbar. The devices were completed depositing a film of pure TaTm (10 nm for devices) and 40 nm of the p-doped electron-transport layer (TaTm: F_6-TCNNQ). Afterwards the metal top contact (Au, 100 nm thick) was deposited.

Characterization. X-ray diffraction (XRD) pattern were collected at room temperature on an Empyrean PANanalytical powder diffractometer in Bragg-Brentano configuration using the Cu Kα1 radiation. Typically, three consecutive measurements were collected and averaged into single spectra. Scanning Electron Microscopy (SEM) images were performed on a Hitachi S-4800 microscope operating at an accelerating voltage of 2 kV over Platinum - metallized samples. Absorption spectra were collected using a fiber optics based Avantes Avaspec2048 Spectrometer. Characterization of the solar cells was performed as follows. The external quantum efficiency (EQE) was estimated using the cell response at different wavelength (measured with a white light halogen lamp in combination with band-pass filters), where the solar spectrum mismatch is corrected using a calibrated Silicon reference cell (MiniSun simulator by ECN, the Netherlands). The current density-voltage (J-V) characteristics were obtained using a Keithley 2400 source measure unit and under white light illumination, and the short circuit current density was corrected considering the device EQE. The electrical characterization was validated using a solar simulator by Abet Technologies (model 10500 with an AM1.5G xenon lamp as the light source). Before each measurement, the exact light intensity was determined using a calibrated Si reference diode equipped with an infrared cut-off filter (KG-3, Schott). The J-V curves were recorded between -0.2 and 1.2 V with 0.01 V steps, integrating the signal for 20 ms after a 10 ms delay. This corresponds to a speed of about 0.3 V s^{-1}. The layout used to test the solar cells has four equal areas (6.53 mm^2, defined as the overlap between the ITO and the top metal contact) and measured through a shadow mask with 2.64 mm^2 aperture.

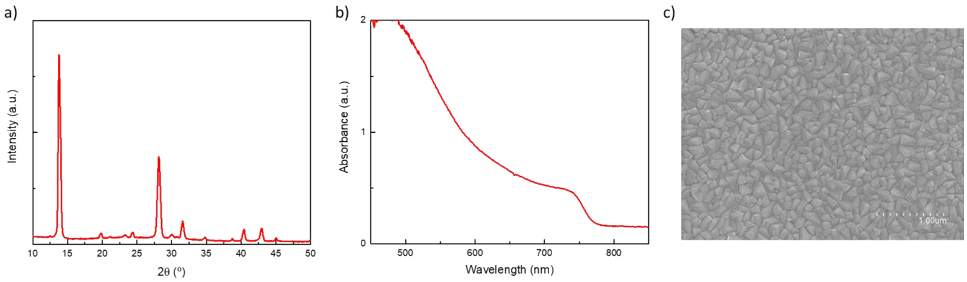

Fig S1 (a) XRD pattern, (b) optical absorbance and (c) surface SEM picture of the vacuum-deposited $CH_3NH_3PbI_3$ thin films for devices preparation.

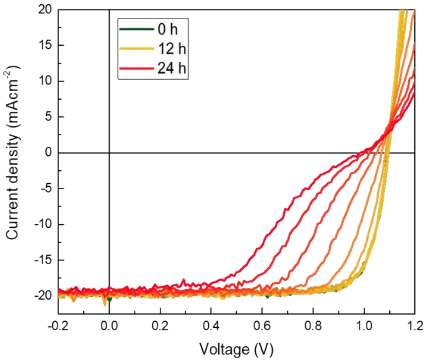

Figure S2. J-V curves under illumination for a perovskite solar cell employing a C60:$(RuCp^*mes)_2$ film (20 nm) as the ETL. The device was kept under continuous simulated solar illumination without encapsulation.

References

1 O. V Gusev, M. A. Ievlev, M. G. Peterleitner, S. M. Peregudova, L. I. Denisovich, P. V Petrovskii and N. A. Ustynyuk, *J. Organomet. Chem.*, 1997, **534**, 57–66.

2 S. Guo, S. B. Kim, S. K. Mohapatra, Y. Qi, T. Sajoto, A. Kahn, S. R. Marder and S. Barlow, *Adv. Mater.*, 2012, **24**, 699–703.

3 H.-I. Un, S. A. Gregory, S. K. Mohapatra, M. Xiong, E. Longhi, Y. Lu, S. Rigin, S. Jhulki, C.-Y. Yang, T. V Timofeeva, J.-Y. Wang, S. K. Yee, S. Barlow, S. R. Marder and J. Pei, *Adv. Energy Mater.*, 2019, **9**, 1900817.

Annex C – Chapter 5 Reference:

High voltage vacuum-deposited

$CH_3NH_3PbI_3$–$CH_3NH_3PbI_3$ tandem solar cells.

Energy & Environmental Science

PAPER

View Article Online
View Journal | View Issue

Published on 27 September 2018. Downloaded by Universitat de València on 4/10/2020 2:55:39 PM.

Check for updates

Cite this: *Energy Environ. Sci.*, 2018, **11**, 3292

High voltage vacuum-deposited $CH_3NH_3PbI_3$–$CH_3NH_3PbI_3$ tandem solar cells†

Jorge Ávila, [a] Cristina Momblona,[a] Pablo Boix, [a] Michele Sessolo, [a] Miguel Anaya, [b] Gabriel Lozano, [b] Koen Vandewal, [c] Hernán Míguez *[b] and Henk J. Bolink *[a]

The recent success of perovskite solar cells is based on two solid pillars: the rapid progress of their power conversion efficiency and their flexibility in terms of optoelectrical properties and processing methods. That versatility makes these devices ideal candidates for multi-junction photovoltaics. We report an optically optimized double junction $CH_3NH_3PbI_3$–$CH_3NH_3PbI_3$ tandem solar cell where the matched short-circuit current is maximized while parasitic absorption is minimized. The use of an additive vacuum-deposition protocol allows us to reproduce calculated stack designs, which comprise several charge selective materials that ensure appropriate band alignment and charge recombination. This rationalized configuration yields an unprecedented open circuit voltage of 2.30 V. Furthermore, this tandem solar cell features efficiencies larger than 18%, higher than those of the individual sub-cells. Low photo-current values allow reducing the losses associated to the series resistance of transparent contacts, which opens the door to the realization of efficient large area modules.

Received 3rd July 2018,
Accepted 21st September 2018

DOI: 10.1039/c8ee01936c

rsc.li/ees

Broader context

Metal halide perovskite based solar cells have rapidly evolved to reach power conversion efficiencies around 23% and operational lifetimes in excess of several thousand hours. Significantly higher efficiencies are predicted for solar cells integrating two different bandgap perovskite absorbers. This has however not been achieved to date, due to insufficient increase of photo-voltages when employing wider bandgap perovskite absorbers and due to the difficulty to form perovskite multi-layer stacks from solution processes. Using optically flat and well controlled vapor phase deposited layers, the optical constants of all layers in a tandem solar cell were determined. These results were employed to calculate the ideal configuration for a tandem cell based on two sub-cells with the same perovskite absorber. The tandem stack design is crucial requiring that both sub-cells generate the same current. The targeted film thicknesses were experimentally reproduced using industrial scale compatible vapor phase deposition methods. As a result, solar cells exhibiting an open-circuit voltage of 2.3 volts were obtained. Besides their application in photovoltaic conversion, such high voltages enable their use as photovoltaic-driven electrochemical cells, including direct power conversion from solar to chemical fuels (water splitting hydrogen production) and carbon dioxide reduction.

Introduction

The use of multiple absorbers in multi-junction solar cells has been demonstrated as a successful strategy to push the power conversion efficiencies (PCE)[1] in several photovoltaic technologies further. Such a device architecture is based on the combination of two or more light absorbers that allow harvesting a broad region of the solar spectrum with lower thermalization losses than a single junction device.[2] Among the different architectures, monolithic (or two-terminal) tandem solar cells lead to an easier management of the generated power and a considerable cost reduction since a lower amount of transparent conductive materials is required. In this monolithic configuration, where all the sub-cells are connected in series, the current through the different sub-cells is ideally the same, while their voltages are added. As a result devices showing high PCE with lower current densities can be demonstrated, which reduces the losses related to series resistance at the contacts and, thus, enabling larger area solar cells.[3] In addition, the intrinsic high voltage in such systems is interesting *per se* for other applications such as photovoltaic-driven electrochemical cells, including direct power

---

[a] *Instituto de Ciencia Molecular, Universidad de Valencia, C/J. Beltrán 2, 46980, Paterna, Spain. E-mail: henk.bolink@uv.es*
[b] *Institute of Materials Science of Seville, Spanish National Research Council-University of Seville, C/Américo Vespucio 49, 41092, Seville, Spain. E-mail: h.miguez@csic.es*
[c] *Institute for Materials Research (IMO-IMOMEC), Universiteit Hasselt, Wetenschapspark 1, 3590 Diepenbeek, Belgium*

† Electronic supplementary information (ESI) available: Materials, experimental data, optics and optical parameters. See DOI: 10.1039/c8ee01936c

This journal is © The Royal Society of Chemistry 2018

Published on 27 September 2018. Downloaded by Universitat de València on 4/10/2020 2:55:39 PM.

conversion from solar to chemical fuels (water splitting hydrogen production) and carbon dioxide reduction.[4,5]

In organic photovoltaics, the combination of the same absorber for each junction was used to circumvent low mobilities of the used materials. In this case, a thick-film solar cell is split into two thin sub-cells, which shortens the distance that charges must travel to be collected and facilitates an efficient light harvesting.[6–12] Due to their easily tunable optoelectronic properties and processability,[13] perovskites are excellent candidates for tandem devices. Perovskite solar cells have been used in combination with silicon based solar cells leading to PCE's of 25%[14–16] for four-terminal and two-terminal configurations, respectively. Also, the combination with CIGS in a four terminal approach has led to tandem cells with a PCE exceeding 20%.[17,18] Aiming at providing a true candidate for the widespread use of an emerging PV technology, recently, perovskite–perovskite tandems have been demonstrated, reaching PCE's above 20% for four-terminal and 18% for two-terminal tandem configurations.[19–25] In general, reports use different perovskites for each sub-cell, with an optimized combination of band-gaps according to the detailed balance model.[26] The currently main limitation of these tandem cells is the limited open circuit voltage (V_{oc}) generated by the wider bandgap perovskite absorber. In all above-mentioned reports, the V_{oc} of the wide bandgap perovskite sub-cell is limited to 1.2 V, except when pure-bromide perovskites are used. Their bandgap is however larger than 2.2 eV which does not lead to sufficient high currents for their use in two terminal tandem cells.[2,24,27] Therefore, it is of interest to examine the potential of double junction solar cells using the same $CH_3NH_3PbI_3$ absorber in both sub-cells. Although this configuration will not benefit from reduced thermalization losses, it still has the previously mentioned multi-junction advantages of high voltages and reduced currents. Furthermore, charge recombination layers developed for homo-tandems can be directly applied on hetero-tandems, as previously reported.[28] Nevertheless, perovskite tandems using the same absorber in both sub-cells have not been optimized so far. To this end, it becomes necessary to develop optical optimization tools accounting for the light absorption in the different materials comprising the device, as has been previously demonstrated for single junction perovskite solar cells.[29,30] However, the complex nature of the multilayered tandem device would require a technique capable of accurately reproducing the layer thicknesses extracted from the optical modelling. In this regard, vacuum processing has been extensively used for perovskite deposition with control over the film thickness at the nanometer scale. Not only for perovskite layers, but also for fully evaporated single junction devices.[31–33] Vacuum processing is an additive technique by nature, which makes it extremely suitable for tandem applications.[34] The deposition is realized at room temperature and complex layer structures can be sublimed to secure low ohmic losses and high transparency.[35]

Here we report an optical model that, combined with a genetic algorithm, allows the optimization of the monolithic tandem layout. Using this optical model, efficient $CH_3NH_3PbI_3$/$CH_3NH_3PbI_3$ vacuum-deposited tandem solar cells with open circuit voltages close to the theoretical limits are developed. The spectral behavior of the external quantum efficiency of the tandem solar cells matches with that predicted by the calculations. The proposed tandem design reaches an efficiency higher than the respective sub-cells, with a V_{oc} of 2.3 V, the highest obtained to-date for any monolithic perovskite-based solar cell. In addition, lower current densities avoid transparent conductive oxide's high resistance losses[3] and enable a perfect recombination layer based on a combination of doped electron and hole transporting layers. This allows the preparation of devices with larger active area without losses in the fill factor (FF).

Results and discussion

The development of an efficient $CH_3NH_3PbI_3$/$CH_3NH_3PbI_3$ tandem photovoltaic device requires the optimization of the light absorption in every sub-cell to avoid current mismatch. The materials of choice derive from previous work in which we demonstrate fully evaporated single junction devices where organic charge selective contacts are employed to attain appropriate band alignment.[35] In order to calculate the fraction of the incident light absorbed by each layer in the stack, the optical constants of the different materials comprising the device were determined for individual thin films with a high optical quality fabricated using a sublimation based deposition protocol. Fig. 1a and b depict SEM images of a cross section of films of $CH_3NH_3PbI_3$ and C_{60}, respectively (see also Fig. S1, ESI†). The films exhibit plane-parallel interfaces over large distances, which results in high optical quality materials with negligible light scattering, suitable

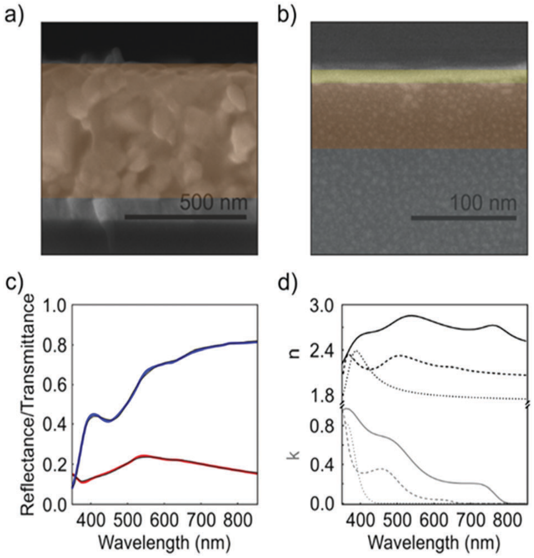

Fig. 1 Scanning electron microscopy image of a cross section of an evaporated $CH_3NH_3PbI_3$ perovskite film (a) and a C_{60} film (b). (c) Experimental and calculated (black lines) reflectance (red line) and transmittance (blue line) spectra of a co-evaporated 65 nm-thick C_{60} film on glass. The incident of the light beam is 30° and it is p-polarized. (d) Spectral dependence of the real (*n*, black lines) and imaginary (*k*, grey lines) parts of the complex refractive index of co-evaporated $CH_3NH_3PbI_3$ (solid), and evaporated C_{60} (dashed) and TaTm (dotted).

Published on 27 September 2018. Downloaded by Universitat de València on 4/10/2020 2:55:39 PM.

for an in-depth spectroscopic characterization. The spectral dependence of light transmitted and reflected at different angles and polarizations of the incident beam (see ESI†) was measured. Based on both the structural and optical characterization, the real (*n*) and imaginary (*k*) parts of the complex refractive index of the films of interest were extracted (see ESI†).[29] To illustrate this, Fig. 1c displays the comparison between measured and calculated specular reflectance and ballistic transmittance of a 65 nm-thick C_{60} film demonstrating excellent agreement (see also Fig. S2, ESI†). Fig. 1d shows the complex refractive indices of TaTm, C_{60} and $CH_3NH_3PbI_3$. Note that the full set of optical constants of vacuum-deposited intrinsic and doped organic layers along with that of methylammonium lead iodine perovskite are provided, to our knowledge for the first time (see Fig. S3, ESI†). Similar optical constants for vacuum deposited $CH_3NH_3PbI_3$ as obtained by us were reported by Meredith *et al.*[36] Having determined the optical constants of the individual films, this now allows for the optical modeling of a $CH_3NH_3PbI_3/CH_3NH_3PbI_3$ tandem solar cell. The proposed configuration comprises a monolithic combination of two vacuum-deposited $CH_3NH_3PbI_3$ sub-cells. The front sub-cell is formed by a fully evaporated stack on a solution-processed titanium dioxide (TiO_2) electron selective layer (ESL), which is deposited on a transparent contact. This configuration was selected as it yields the highest open circuit voltages among pure $CH_3NH_3PbI_3$ solar cells in a single junction configuration (1.17 V).[37] The back sub-cell employs instead of the TiO_2/C_{60} a doped C_{60}/intrinsic C_{60} as ESL.[35] The fully evaporated recombination layer consists of a combination of organic materials, intrinsic (TaTm) and doped (TaTm:F_6-TCNNQ), which allows the extraction of the photogenerated holes of the front cell, along with doped (C_{60}:PhIm) and intrinsic (C_{60}) layers to extract the electrons of the back cell (details in Experimental section). The combined intrinsic and doped layers are referred to hole and electron selective layers (HSL and ESL, respectively). The direct connection of both doped materials assures a proper electrical contact in the recombination layer with low optical losses,[24] whereas the intrinsic layers enhance the charge selectivity and reduce surface recombination. The device is completed with a thicker layer of the $CH_3NH_3PbI_3$ absorber and the TaTm/TaTm:F_6-TCNNQ hole extraction layers with the Au contact, as depicted in Fig. 2a. Fabrication details are available in the ESI.†

We combine our optical model with a generic algorithm to find the device configuration that results in optimum light harvesting. In order to do that, the spatial and spectral variation of the electric field intensity throughout the complete stack of the evaluated tandem cell architecture are calculated (Fig. 2b). Then, the J_{sc} for each sub-cell is extracted by estimating the actual amount of light absorbed in each perovskite layer (productive absorption displayed in Fig. 2c). Light penetration in the device depends strongly on the incident wavelength. Calculations indicate that most of the high-energy photons are absorbed within the first few nanometers of the front $CH_3NH_3PbI_3$ layer. At the same time, this layer is thin enough as to allow low-energy photons to be harvested by the back perovskite layer (see blue and red lines in Fig. 2c). Our optimization model maximizes the short circuit photocurrent (J_{sc}) of both front and back sub-cells while the photocurrent mismatch is minimized. This method allows us to attain an optimum configuration by evaluating a few thousands of architectures in which the thicknesses of the different layers present in the system are varied at the same time. Table 1 summarizes the result of the optimization, indicating the thickness of each layer in the best-performing device. The thickness of front and back $CH_3NH_3PbI_3$ layers are rather dissimilar (95 nm *vs.* 420 nm) and yield J_{sc} values of front and back cells of 10.35 mA cm^{-2} and 10.21 mA cm^{-2}, respectively, which give rise to an effectively minimized photocurrent mismatch (0.14 mA cm^{-2}). At the same time, these results indicate that the thickness of both ESL and HSL materials should

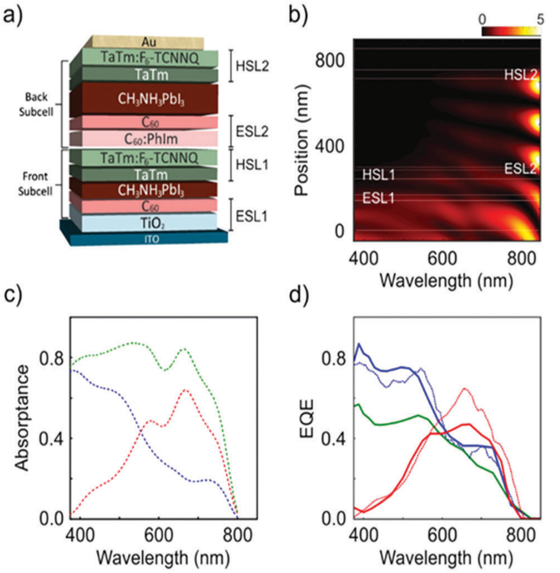

Fig. 2 (a) Scheme of the $CH_3NH_3PbI_3/CH_3NH_3PbI_3$ tandem solar cell. (b) Spectral dependence of the calculated electric field intensity across the section of the simulated tandem device. (c) Spectral dependence of the calculated fraction of the incident light absorbed in the front (blue line) and back $CH_3NH_3PbI_3$ layer (red line) of the tandem device. Green line shows the productive absorbance of the complete device. (d) Spectral dependence of the experimental (solid line) and calculated (dashed line) external quantum efficiency (EQE) associated to the front (blue line) and back (red line) sub-cells. Green line shows the measured EQE for the complete tandem device.

Table 1 Optimized thickness of each layer in the best performing devices

Layer	Sim. thickness (nm)	Exp. thickness (nm)
Air	Semi-infinite	
Glass	1.1×10^6	1.1×10^6
ITO	140	140
TiO_2	25	30
C_{60}	10	10
Front perovs	95	90
TaTm	40	10
Doped TaTm	35	25
Doped C_{60}	38	25
C_{60}	10	10
Back perovs	420	400
TaTm	26	10
Doped TaTm	29	40
Gold	100	100

This journal is © The Royal Society of Chemistry 2018

Published on 27 September 2018. Downloaded by Universitat de València on 4/10/2020 2:55:39 PM.

be kept below 40 nm to minimize the impact of parasitic absorption, which is more critical for those organic layers that are at the front side of the cell.

Based on this design, $CH_3NH_3PbI_3/CH_3NH_3PbI_3$ tandem solar cells were prepared with the layout depicted in Fig. 2b and with layer thicknesses close to the optimized ones from the calculations, which are listed in Table 1. Small deviations between the calculated optimum values and the experimental ones are due to the need of maintaining the thickness of intrinsic charge transport layers as low as possible, to compensate for their low charge mobility. As for the perovskite absorbers, the deviations between calculated and experimental values are due to small experimental variations (plus or minus 25 nm). Table 1 shows average experimental values.

An initial study of the individual sub-cells is useful to understand the working conditions of the tandem. Therefore, single-junction $CH_3NH_3PbI_3$ solar cells were prepared with a structure equivalent to that of each of the sub-cells, in the 2T tandem structure. Specifically, the structure of the analyzed devices was ITO/TiO_2/C_{60}/$CH_3NH_3PbI_3$/TaTm/TaTm:F_6-TCNNQ/Au with an absorber thickness of 90 nm as a reference for the front cell; and ITO/C_{60}:PhIm/C_{60}/$CH_3NH_3PbI_3$/TaTm/TaTm:F_6-TCNNQ/Au with a perovskite thickness of 400 nm as a reference for the back cell. We have calculated EQE of individual sub-cells assuming that all light absorbed by the $CH_3NH_3PbI_3$ layers is converted into photocurrent. Using the 2T tandem and both single junction cells the EQE of these cells were also experimentally determined (details in the ESI†). Fig. 2d displays the comparison between experimental and calculated values. The current density calculated from the single junction devices is reported in the ESI† (Fig. S7). Our model reproduces the optical features observed for both individual front and back cells fairly well.

The current–voltage (*J–V*) curves under 100 mW cm^{-2} illumination of the tandem and single junction reference cells are depicted in Fig. 3. The front single junction reference cell shows a very high fill factor (FF) over 80%, which is indicative of the optimum charge transport and low extraction barrier at the contacts. The former can be attributed to the thickness of the perovskite, thinner than in standard perovskite solar cells, whereas the excellent extraction by the employed contacts had been previously reported.[35,37] Similarly, the achieved V_{oc}, 1.19 V and 1.13 V for the front and back single junction cells respectively, indicate low recombination rates dominating the devices' performance. The value obtained for the thinnest device, 1.19 V, is to the best of our knowledge the highest one obtained for pure $CH_3NH_3PbI_3$ based solar cell. It exhibits only 410 mV deficit with respect to the bandgap value calculated from the absorption, very close to the theoretical limit.[38,39] This is a clear sign of reduced non-radiative losses, with minimized bulk recombination (in line with the thin absorber layer), and optimized interfaces.[37] In contrast, the relatively low short circuit current (J_{sc}) of the devices, 12.5 and 18.7 mA cm^{-2} for front and back cells respectively, limits the power conversion efficiency to ∼12% and ∼17%, as predicted with our optical model for thin absorbers layers. To mirror the conditions of the back single junction sub-cell in the tandem configuration, it was also measured under filtered illumination. The filter consists of a glass/$CH_3NH_3PbI_3$ sample with perovskite thickness similar to that of the front cell. Consequently, the V_{oc} was marginally reduced and the J_{sc} is reduced by approximately 50%: the FF however increased slightly, probably related to the reduced influence of the series resistance when a smaller current density is extracted. Table 2 summarizes the results.

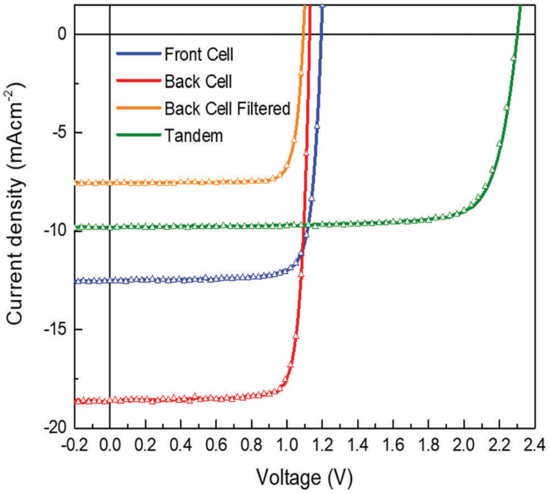

Fig. 3 *J–V* characteristics under 1 sun illumination for the single junction cell with the thin perovskite layer (mimicking the front cell in the tandem configuration), blue curve, the single junction cell with the 400 nm perovskite layer (red curve), that cell but illuminated through a filter consisting of glass/$CH_3NH_3PbI_3$ film of 90 nm (mimicking the back cell in the tandem configuration), orange curve and the 2T tandem cell (green curve). Symbols indicate the reverse scans, from positive to negative.

Fig. 3 also shows the *J–V* curve of the monolithic tandem cell. The forward (from J_{sc} to V_{oc}) and reverse (from V_{oc} to J_{sc}) *J–V* curves are depicted and show an almost negligible hysteresis. The FF remains high (>80%), which highlights the quality of the charge recombination layer (CRL). Notably, a V_{oc} as high as 2305 mV is observed, very close to the sum of the photovoltages of each reference cell (front cell plus filtered back cell). The J_{sc} of the tandem is 9.84 mA cm^{-2}, slightly lower than the one calculated from the simulations (10.16 mA cm^{-2}) that consider the same layer thicknesses as the ones experimentally achieved. This value, however, is higher than that observed for the filtered reference back cell, which had a J_{sc} of 7.52 mA cm^{-2}. This value would be expected to be the limiting value for the tandem cell performance as the front and back cells are in series in the 2T configuration. In order to confirm the measured current, the tandem's external quantum efficiency was determined by pulsed light controlled by a monochromator and a lock-in amplifier,

Table 2 *J–V* parameters of reference cells and tandem device measured under standard AM1.5G illumination

	V_{oc} (V)	J_{sc} (mA cm^{-2})	FF (%)	PCE (%)
Reference front cell	1.19	12.53	81.54	12.16
Reference back cell	1.13	18.66	83.31	17.55
Ref. back cell filtered	1.09	7.52	83.83	6.88
Tandem	2.30	9.84	79.58	18.02

Published on 27 September 2018. Downloaded by Universitat de València on 4/10/2020 2:55:39 PM.

while a background white light ensured the proper extraction of the charges (Fig. 2d). Comparing the integrated J_{sc}, we observe that the one of the tandem is 1.8 mA cm^{-2} higher than the J_{sc} of the reference back cell filtered (Table 2), which confirms that the back sub-cell limitation in current is much lower than deducted from the standalone reference back cell J_{sc}. The origin of the mismatch between the filtered back cell and tandem back subcell is related to the optical losses in the glass/perovskite sample used as filter (Fig. S8, ESI†). As a result, the tandem achieves a power conversion efficiency of 18.02%, which exceeds the PCEs of both reference cells.

Conclusions

We have demonstrated operational $CH_3NH_3PbI_3$–$CH_3NH_3PbI_3$ tandem solar cells with PCEs similar to single junction devices (>18%), yet with a strongly reduced current density and a very high open circuit voltage (2.3 volts). Using carefully determined optical constants of all the layers in the stack and an optical model the ideal configuration of the tandem was accurately predicted. This was verified by comparing the simulated and the measured external quantum efficiency curves, which show a good resemblance. The use of molecular based charge recombination layers leads to very low voltage losses and allows for the very high open circuit voltage of the tandem stack. These results validate the use of vapor process for the development of complex perovskite device architectures such as tandems. This approach opens the path to the preparation of devices with larger active area without losses in the fill factor.

Conflicts of interest

There are no conflicts to declare.

Acknowledgements

We acknowledge financial support from the European Union H2020 project INFORM (grant 675867), the Spanish Ministry of Economy and Competitiveness (MINECO) *via* the Unidad de Excelencia María de Maeztu MDM-2015-0538, MAT2017-88905-P, MAT2017-88821-R, MAT2017-88584-R, PCIN-2015-255 and PCIN-2017-014 and the Generalitat Valenciana (Prometeo/2016/135). M. S. and P. P. B. thank the MINECO for their post-doctoral RyC contracts. P. P. B. acknowledges the financial support from the Conselleria d'Educació, Investigació, Cultura i Esport Valenciana (SEJI2017/2017/012). J. A. thanks the Spanish Ministry of Education, Culture and Sport for his pre-doctoral grant. M. A. is grateful to "La Caixa" Foundation for its financial support.

Notes and references

1 NREL efficiency chart, https://www.nrel.gov/pv/assets/images/efficiency-chart.png.
2 M. Anaya, G. Lozano, M. E. Calvo and H. Míguez, *Joule*, 2017, **1**, 769–793.
3 S. Calnan and A. N. Tiwari, *Thin Solid Films*, 2010, **518**, 1839–1849.
4 S. Esiner, G. W. P. van Pruissen, M. M. Wienk and R. A. J. Janssen, *J. Mater. Chem. A*, 2016, **4**, 5107–5114.
5 G. Yangqin, V. M. Le Corre, G. Alexandre, N. Marios, H. M. Abdul, T. Kazuhiro and P. M. Beaujuge, *Adv. Mater.*, 2016, **28**, 3366–3373.
6 H. Zhou, Y. Zhang, C.-K. Mai, S. D. Collins, G. C. Bazan, T.-Q. Nguyen and A. J. Heeger, *Adv. Mater.*, 2015, **27**, 1767–1773.
7 J. You, C.-C. Chen, Z. Hong, K. Yoshimura, K. Ohya, R. Xu, S. Ye, J. Gao, G. Li and Y. Yang, *Adv. Mater.*, 2013, **25**, 3973–3978.
8 A. Puetz, F. Steiner, J. Mescher, M. Reinhard, N. Christ, D. Kutsarov, H. Kalt, U. Lemmer and A. Colsmann, *Org. Electron.*, 2012, **13**, 2696–2701.
9 H. Kang, S. Kee, K. Yu, J. Lee, G. Kim, J. Kim, J.-R. Kim, J. Kong and K. Lee, *Adv. Mater.*, 2015, **27**, 1408–1413.
10 Y. Liu, C.-C. Chen, Z. Hong, J. Gao, Y. Yang, H. Zhou, L. Dou, G. Li and Y. Yang, *Sci. Rep.*, 2013, **3**, 3356.
11 S. Lu, H. Lin, S. Zhang, J. Hou and W. C. H. Choy, *Adv. Energy Mater.*, 2017, **7**, 1701164.
12 S. Lu, X. Guan, X. Li, W. E. I. Sha, F. Xie, H. Liu, J. Wang, F. Huang and W. C. H. Choy, *Adv. Energy Mater.*, 2015, **5**, 1500631.
13 B. Chen, X. Zheng, Y. Bai, N. P. Padture and J. Huang, *Adv. Energy Mater.*, 2017, **7**, 1602400.
14 J. R. M. Werner, L. Barraud, A. Walter, M. Bräuninger, F. Sahli, D. Sacchetto, N. Tétreault, B. Paviet-Salomon, S.-J. Moon, C. Allebe, M. Despeisse, S. Nicolay, S. D. Wolf, B. Niesen and C. Ballif, *ACS Energy Lett.*, 2016, **1**, 474–480.
15 F. Sahli, J. Werner, B. A. Kamino, M. Bräuninger, R. Monnard, B. Paviet-Salomon, L. Barraud, L. Ding, J. J. Diaz Leon, D. Sacchetto, G. Cattaneo, M. Despeisse, M. Boccard, S. Nicolay, Q. Jeangros, B. Niesen and C. Ballif, *Nat. Mater.*, 2018, **17**, 820–826.
16 K. Jäger, L. Korte, B. Rech and S. Albrecht, *Opt. Express*, 2017, **25**, A473–A482.
17 A. Guchhait, H. A. Dewi, S. W. Leow, H. Wang, G. Han, F. B. Suhaimi, S. Mhaisalkar, L. H. Wong and N. Mathews, *ACS Energy Lett.*, 2017, **2**, 807–812.
18 F. Fu, T. Feurer, T. Jäger, E. Avancini, B. Bissig, S. Yoon, S. Buecheler and A. N. Tiwari, *Nat. Commun.*, 2015, **6**, 8932.
19 M. T. Hörantner, T. Leijtens, M. E. Ziffer, G. E. Eperon, M. G. Christoforo, M. D. McGehee and H. J. Snaith, *ACS Energy Lett.*, 2017, **2**, 2506–2513.
20 R. Adharsh, Y. Zhibin, J. S. Byeok, I. L. Braly, L. Po-Wei, H. W. Hillhouse and A. K.-Y. Jen, *Adv. Mater.*, 2017, **29**, 1702140.
21 R. Sheng, M. T. Hörantner, Z. Wang, Y. Jiang, W. Zhang, A. Agosti, S. Huang, X. Hao, A. Ho-Baillie, M. Green and H. J. Snaith, *J. Phys. Chem. C*, 2017, **121**, 27256–27262.
22 G. E. Eperon, M. T. Hörantner and H. J. Snaith, *Nat. Rev. Chem.*, 2017, **1**, 0095.
23 G. E. Eperon, T. Leijtens, K. A. Bush, R. Prasanna, T. Green, J. T.-W. Wang, D. P. McMeekin, G. Volonakis, R. L. Milot, R. May, A. Palmstrom, D. J. Slotcavage, R. A. Belisle,

This journal is © The Royal Society of Chemistry 2018

Published on 27 September 2018. Downloaded by Universitat de València on 4/10/2020 2:55:39 PM.

J. B. Patel, E. S. Parrott, R. J. Sutton, W. Ma, F. Moghadam, B. Conings, A. Babayigit, H.-G. Boyen, S. Bent, F. Giustino, L. M. Herz, M. B. Johnston, M. D. McGehee and H. J. Snaith, *Science*, 2016, **354**, 861–865.

24 D. Forgcs, L. Gil-Escrig, D. Prez-Del-Rey, C. Momblona, J. Werner, B. Niesen, C. Ballif, M. Sessolo and H. J. Bolink, *Adv. Energy Mater.*, 2016, 1602121.

25 D. Zhao, Y. Yu, C. Wang, W. Liao, N. Shrestha, C. R. Grice, A. J. Cimaroli, L. Guan, R. J. Ellingson, K. Zhu, X. Zhao, R.-G. Xiong and Y. Yan, *Nat. Energy*, 2017, **2**, 17018.

26 A. D. Vos, *J. Phys. D: Appl. Phys.*, 1980, **13**, 839.

27 C. Bo, Z. Xiaopeng, B. Yang, N. P. Padture and H. Jinsong, *Adv. Energy Mater.*, 2017, **7**, 1602400.

28 F. Jiang, T. Liu, B. Luo, J. Tong, F. Qin, S. Xiong, Z. Li and Y. Zhou, *J. Mater. Chem. A*, 2016, **4**, 1208–1213.

29 M. Anaya, J. P. Correa-Baena, G. Lozano, M. Saliba, P. Anguita, B. Roose, A. Abate, U. Steiner, M. Gratzel, M. E. Calvo, A. Hagfeldt and H. Miguez, *J. Mater. Chem. A*, 2016, **4**, 11214–11221.

30 M. Anaya, G. Lozano, M. E. Calvo, W. Zhang, M. B. Johnston, H. J. Snaith and H. Míguez, *J. Phys. Chem. Lett.*, 2015, **6**, 48–53.

31 M. Sessolo, C. Momblona, L. Gil-Escrig and H. J. Bolink, *MRS Bull.*, 2015, **40**, 660–666.

32 L. K. Ono, M. R. Leyden, S. Wang and Y. Qi, *J. Mater. Chem. A*, 2016, **4**, 6693–6713.

33 P.-S. Shen, Y.-H. Chiang, M.-H. Li, T.-F. Guo and P. Chen, *APL Mater.*, 2016, **4**, 091509.

34 J. Ávila, C. Momblona, P. P. Boix, M. Sessolo and H. J. Bolink, *Joule*, 2017, **1**, 431–442.

35 C. Momblona, L. Gil-Escrig, E. Bandiello, E. M. Hutter, M. Sessolo, K. Lederer, J. Blochwitz-Nimoth and H. J. Bolink, *Energy Environ. Sci.*, 2016, **9**, 3456–3463.

36 Q. Lin, A. Armin, R. C. R. Nagiri, P. L. Burn and P. Meredith, *Nat. Photonics*, 2014, **9**, 106–112.

37 D. Pérez-del-Rey, P. P. Boix, M. Sessolo, A. Hadipour and H. J. Bolink, *J. Phys. Chem. Lett.*, 2018, **9**, 1041–1046.

38 S. Rühle, *Sol. Energy*, 2016, **130**, 139–147.

39 W. Tress, *Adv. Energy Mater.*, 2017, **7**, 1602358.

Electronic Supplementary Material (ESI) for Energy & Environmental Science.
This journal is © The Royal Society of Chemistry 2018

High voltage vacuum-deposited $CH_3NH_3PbI_3$-$CH_3NH_3PbI_3$ tandem solar cells

Jorge Avila,[a] Cristina Momblona,[a] Pablo Boix, [a] Michele Sessolo,[a] Miguel Anaya,[b] Gabriel Lozano, [b] Koen Vandewal,[c] Hernán Míguez[b] and Henk J. Bolink*[a]

[a] Instituto de Ciencia Molecular, Universidad de Valencia, C/ J. Beltrán 2, 46980, Paterna, Spain

[b] Institute of Materials Science of Seville, Spanish National Research Council-University of Seville, C/Américo Vespucio 49, 41092, Seville, Spain.

[c] Institute for Materials Research (IMO-IMOMEC), Universiteit Hasselt, Wetenschapspark 1, 3590 Diepenbeek, Belgium

Supporting Information

Materials. Photolithographically patterned ITO coated glass substrates were purchased from Naranjo Substrates (www.naranjosubstrates.com). 2,2'-(Perfluoronaphthalene-2,6-diylidene) dimalononitrile (F_6-TCNNQ), N4,N4,N4",N4"-tetra([1,1'-biphenyl]-4-yl)-[1,1':4',1"-terphenyl]-4,4"-diamine (TaTm) and N1,N4-bis(tri-p-tolylphosphoranylidene)benzene-1,4-diamine (PhIm) were provided from Novaled GmbH. Fullerene (C_{60}) was purchased from sigma Aldrich. PbI_2 was purchased from Tokyo Chemical Industry CO (TCI), and CH_3NH_3I (MAI) from Lumtec**.** TiO_2 nanoparticle suspensions were prepared in IMEC and deposited through a low temperature process compatible with ITO substrates. Non-aqueous sol-gel route is used,[1] in which the oxygen required for the nanoparticle formation is provided by benzyl alcohol. In detail, 2 mL anhydrous ethanol is mixed with 0.5 mL titanium (IV) chloride ($TiCl_4$ from Sigma Aldrich) inside a nitrogen field glove box. After stirring for 10 minutes at room temperature, 10 mL benzyl alcohol (Sigma Aldrich) is added to the mixture leading to a light yellow and clear solution. This solution is stirred for at least 18 hours at 80 ºC leading to colourless hazy suspension. The haziness of the suspension is caused by creation of white titanium oxide nanoparticles. To separate them, 1 mL of the resulting milky suspension was precipitated in 10 mL of diethyl ether (from Sigma Aldrich) and centrifuged at 5000 rpm for two minutes to isolate the nanoparticles from the solvent and the unreacted precursor. After centrifuge, the solvent was drained out and solid white nanoparticles were dispersed into 3 mL pure ethanol leading to milky (white and hazy) solution. To stabilize this final dispersion, 45 μL Diisopropoxytitaan-bis-(acetylacetonaat) (TiAcac purchased from Sigma Aldrich) is added to the solution. After less than one hour, a light green and clear solution is created.[2] This is the final product containing of TiO_2 nanoparticles in pure ethanol.

Device preparation. ITO-coated glass substrates were subsequently cleaned with soap, water and isopropanol in an ultrasonic bath, followed by UV-ozone treatment. The TiO_2 dispersion was deposited in air by spin-coating at 3000 rpm for 30 s and annealed at 100 ºC for 30 min, leading to a 20-40 nm thick compact layer. Them, they were transferred to a vacuum chamber integrated into a nitrogen-filled glovebox (MBraun, H_2O and $O_2 < 0.1$ ppm) and evacuated to a pressure of $1 \cdot 10^{-6}$ mbar. The vacuum chamber uses a turbomolecular pump (Pfeiffer TMH 261P, DN 100 ISO-K, 3P) coupled to a scroll pump. The vacuum chamber is equipped with six temperature controlled evaporation sources (Creaphys) fitted with ceramic crucibles. The sources were directed upwards with an angle of approximately 90º with respect to the bottom of the evaporator. The substrate holder to evaporation sources distance is approximately 20 cm. Three quartz crystal microbalance (QCM) sensors are used, two monitoring the deposition rate of each evaporation source and a third one close to the substrate holder monitoring the total deposition rate. For thickness calibration, we first individually sublimed the charge transport materials and their dopants (TaTm and F_6-TCNNQ, C_{60} and PhIm). A calibration factor was obtained by comparing the thickness inferred from the QCM sensors with that measured with a mechanical profilometer (Ambios XP1). Then these materials were co-sublimed at temperatures ranging from 135-160 ºC for the dopants to 250 ºC for the pure charge transport molecules, and the evaporation rate was controlled by separate QCM sensors and adjusted to obtain the desired doping concentration. In general, the deposition rate for TaTm and C_{60} was kept constant at 0.8 Å s^{-1} while varying the deposition rate of the dopants during co-deposition. Pure TaTm, F_6-TCNNQ, BCP and C_{60} layers were deposited at a rate of 0.5 Å s^{-1}.

After deposition of the TiO_2, 10 nm thick C_{60} is vacuum-deposited. Once completed this deposition, the chamber was vented with dry N_2 to replace the ETL crucible with those containing the starting materials for the perovskite deposition, PbI_2 and CH_3NH_3I. The vacuum chamber was evacuated again to a pressure of 10^{-6} mbar, and the perovskite films were then obtained by co-deposition of the two precursors. The calibration of the deposition rate for the CH_3NH_3I was found to be difficult due to non-uniform layers and the soft nature of the material which impeded accurate thickness measurements. Hence, the source temperature of the CH_3NH_3I was kept constant at 70 ºC and the $CH_3NH_3I:PbI_2$ ratio was controlled off line using grazing incident x-ray diffraction by adjusting the PbI_2 deposition temperature. The optimum deposition temperatures were found to be 250 ºC for the PbI_2 and 70 ºC for the CH_3NH_3I. After deposition of the desired thickness perovskite film, the chamber was vented, and the crucibles replaced with those containing the hole-transport materials and evacuated again to a pressure of 10^{-6} mbar. Then, a film of pure TaTm (10 nm) follows by 25 nm of the p-doped hole-transport layer (TaTm: F_6-TCNNQ) was evaporated. For the reference Front Cell device, the metal top contact (Au, 100 nm thick) was deposited. In the case of tandem devices, 25 nm of the n-doped electron-transport layer (C_{60}: PhIm) capped with 10 nm of the pure C_{60} were deposited to complete the charge recombination layers. Once completed this deposition, the chamber was vented with dry N_2 to replace the ETL crucibles with those containing the starting materials for the perovskite deposition, PbI_2 and CH_3NH_3I. Following the previous described protocol, the back subcell perovskite layer was deposited. After deposition of the desired thickness perovskite film, the chamber was vented, and the crucibles replaced with those containing the hole-transport materials and evacuated again to a pressure of 10^{-6} mbar. Then, a film of pure TaTm (10 nm) follows by 40 nm of the p-doped hole-transport layer (TaTm: F_6-TCNNQ) was evaporated. Afterwards the metal top contact (Au, 100 nm thick) was deposited.

Characterization. Absorption spectra were collected using a fiber optics based Avantes Avaspec2048 Spectrometer. Characterization of the solar cells was performed as follows. The external quantum efficiency (EQE) was estimated using the cell response at different wavelength (measured with a white light halogen lamp in combination with band-pass filters), where the solar spectrum mismatch is corrected using a calibrated Silicon reference cell (MiniSun simulator by ECN, the Netherlands). The current density-voltage (J-V) characteristics were obtained using a Keithley 2400 source measure unit and under white light illumination, and the short circuit current density was corrected considering the device EQE. The electrical characterization was validated using a solar simulator by

Abet Technologies (model 10500 with an AM1.5G xenon lamp as the light source). Before each measurement, the exact light intensity was determined using a calibrated Si reference diode equipped with an infrared cut-off filter (KG-3, Schott). The J-V curves were recorded between -0.2 and 2.4 V with 0.01 V steps, integrating the signal for 20 ms after a 10 ms delay. This corresponds to a speed of about 0.3 V s^{-1}. The layout used to test the solar cells has four equal areas (0.04 cm^2, defined as the overlap between the ITO and the top metal contact) and measured through a shadow mask with 0.01 cm^2 aperture.

Optics

We have performed a spectroscopic analysis of the light reflected and transmitted by the samples. In particular, specular reflectance and ballistic transmittance at three different angles of the incident light beam, i.e. 6°, 30°, and 50°, for s and p polarized light, were experimentally obtained.

Based on this characterization we extract the real (n) and imaginary (k) parts of the complex refractive index of the films. We have developed a homemade code based on the transfer matrix method to model the evaporated film considering air as the incoming and outgoing media and two layers: i) a perovskite (or ESL, or HTL) film, and ii) a 1mm-thick (0.74 mm for ESL, HTL) glass substrate. The high optical quality of the analysed samples indicates that the different interfaces can be considered as plane-parallel. We use a Forouhi-Bloomer model to extract the complex refractive index of the materials.[3] This model considers a nanocrystalline semiconductor, which is ideal for the materials that we have studied. In particular, we have used the Jobin Yvon (new amorphous) parametrization[4]

$$n(E) = n_\infty \sum_{j=1}^{N} \frac{B_j\left(E - E_j\right) + C_j}{(E - E_j)^2 + \Gamma_j^2}, \tag{1}$$

$$k(E) = \begin{cases} \displaystyle\sum_{j=1}^{N} \frac{f_j (E - E_g)^2}{(E - E_j)^2 + \Gamma_j^2}; \text{for } E > E_g \\ 0; \text{for } E < E_g \end{cases} \tag{2}$$

with

$$B_j = \frac{f_j}{\Gamma_j}\left(\Gamma_j^2 - \left(E - E_j\right)^2\right) \text{ and } C_j = 2 f_j \Gamma_j \left(E - E_j\right)$$

Where E is the energy, E_g is the bandgap, and E_j, f_j, and Γ_j are the position, strength, and width of one oscillator. In our case, we have employed 3 oscillators (N=3). Please note that this formalism is fully consistent with Kramers-Kronig relations

$$n(\omega) = n_0 + \frac{2}{\pi} \mathrm{P} \int_0^{\infty} \frac{\Omega k(\Omega)}{\Omega^2 - \omega^2} d\Omega, \tag{3}$$

where $\omega = 2\pi c/\lambda$ is the angular frequency and c is the speed of light in vacuum.

Then, we employ a genetic algorithm to simultaneously fit the p and s polarizations of the angular dependence of specular reflectance and ballistic transmittance spectra for the different films provided. Full details on the model can be found elsewhere.[5, 6]

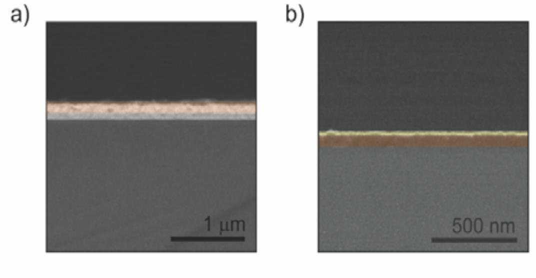

Figure S1. Zoom out of a scanning electron microscopy image of a cross section of an evaporated $CH_3NH_3PbI_3$ perovskite film (a) and a C_{60} film (b).

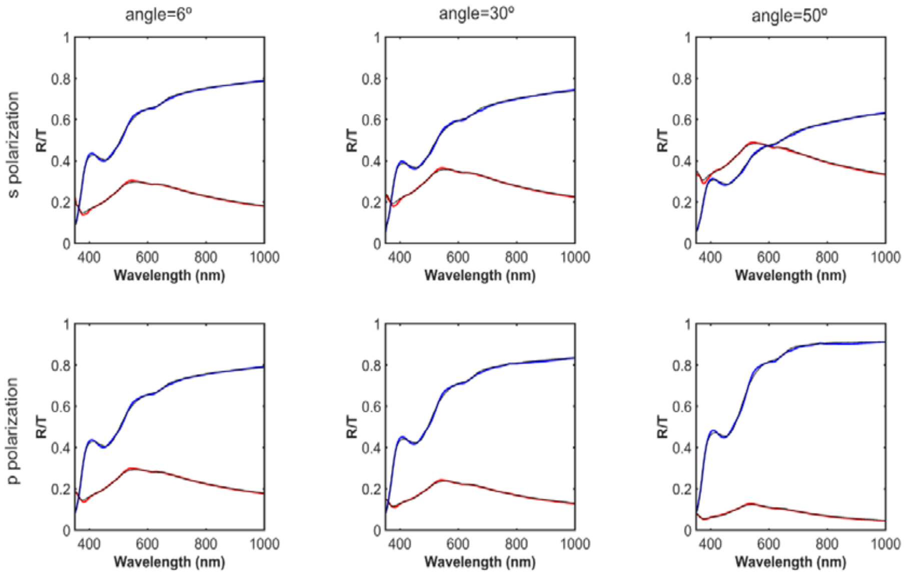

Figure S2. Experimental (colour lines) and calculated (black lines) reflectance and transmittance spectra of an evaporated 65 nm-thick C_{60} film on glass. S and p polarization are shown in the top and bottom panels, respectively. The angle of the incident light beam is set at 6°, 30°, and 50°.

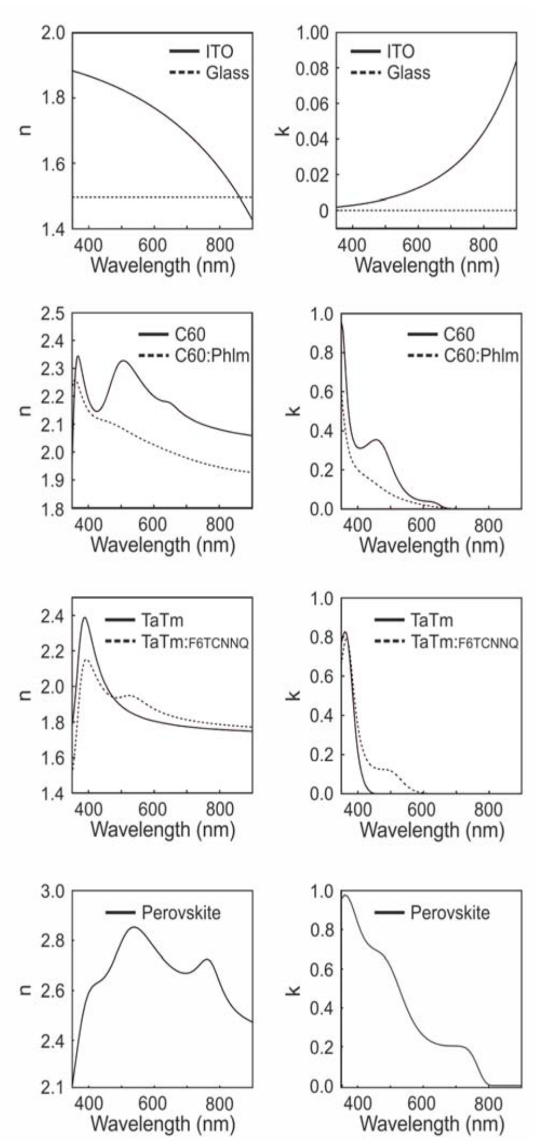

Figure S3. Refractive indices for the different materials comprising the tandem device. We have taken the n and k values from the literature for gold[7] and TiO_2.[8]

C60

Table S1. Optical model parameters attained for the intrinsic and doped C_{60} films.

Parameter	C_{60}	C_{60}: PhIm (60 wt%)
Eg (eV)	1.78	1.68
n_∞	1.91	1.83
f_1	0.011	0.042
f_2	0.055	0.024
f_3	0.009	0.010
E_1 (eV)	1.91	1.80
E_2 (eV)	2.55	2.73
E_3 (eV)	3.52	3.65
Γ_1 (eV)	0.100	0.584
Γ_2 (eV)	0.347	0.581
Γ_3 (eV)	0.181	0.246
d (nm)	67	33

Please notice the reliability of our method since profilometer measurements give a thickness of 65 nm (35 nm) for the intrinsic (doped) C_{60}, while calculations yield 67 nm (33 nm).

TaTm

Table S2. Optical model parameters attained for the intrinsic and doped TaTm films.

Parameter	TaTm	TaTm: F_6-TCNNQ (11 wt%)
Eg (eV)	2.69	1.92
n	1.66	1.65
f_1	0.146	0.028
f_2	0.014	0.027
E_1 (eV)	3.30	3.34
E_2 (eV)	2.89	2.37
Γ_1 (eV)	0.280	0.282
Γ_2 (eV)	0.340	0.260
d (nm)	47	34

Profilometer measurements give a thickness of 40 nm (40 nm) for the intrinsic (doped) TaTm while calculations yield 47 nm (34 nm).

$CH_3NH_3PbI_3$

In the case of perovskite films, first we have confirmed the high optical quality of the films as it is a recurrent problem in the literature. In order to do that, we have measured total reflectance, diffuse reflectance, total transmittance and diffuse transmittance with an integrating sphere. These measurements allow us to determine the fraction of incident light absorbed by the films as shown in Figure S4a. Besides, the diffuse reflectance spectra reveal the high optical quality of the thin films due to the negligible fraction of diffusely scattered light (see Figure S4b).

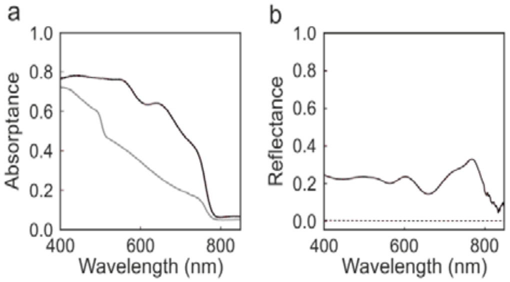

Figure S4. (a) Experimental absorptance spectra of co-evaporated perovskite films with thicknesses of 490 nm (black) and 120 nm (grey). A=1-R-T. (b) Experimental total (solid black) and diffuse (dashed black) reflectance spectra of a co-evaporated perovskite film of 490 nm of thickness.

Table S3. Optical model parameters attained for the perovskite films.

Parameter	**Thick film $CH_3NH_3PbI_3$**
Eg (eV)	1.53
n	2.16
f_1	0.1285
f_2	0.089
f_3	0.051
E_1 (eV)	1.60
E_2 (eV)	2.40
E_3 (eV)	3.30
G_1 (eV)	0.100
G_2 (eV)	0.432
G_3 (eV)	0.548
d (nm)	91

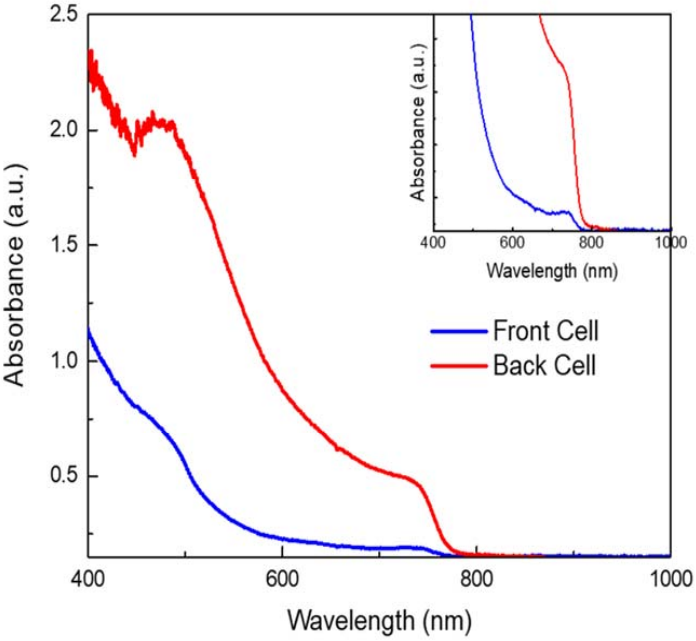

Figure S5. Perovskite absorbance spectra of front cell (90 nm) and back cell (400 nm). The inset is a zoom of the absorption onset.

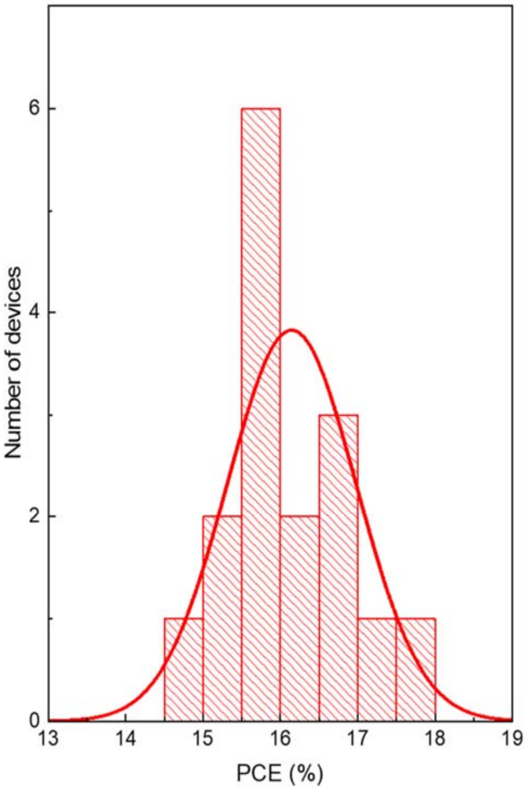

Figure S6. PCE statistical distribution of tandem devices. Solid line represents the Gaussian distribution fitting for the PCE.

Table S4. Statistical distribution of J-V parameters of devices measured under standard AM1.5G illumination.

V_{oc} (V)	**J_{sc} (mAcm^{-2})**	**FF (%)**	**PCE (%)**
2.25 ± 0.04	8.6 ± 0.4	83 ± 1	16.1 ± 0.8

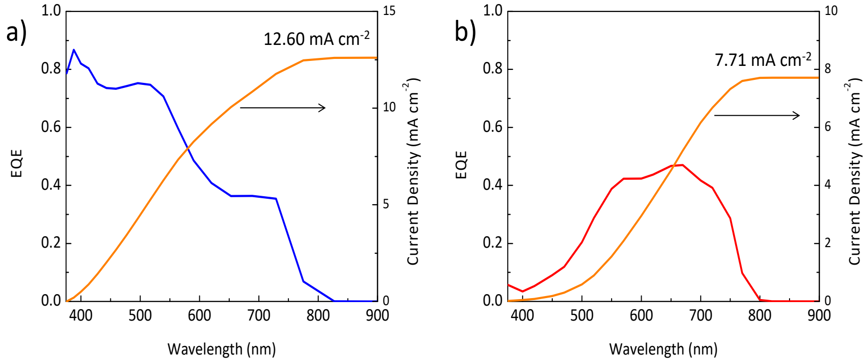

Figure S7. EQE spectra for the single junction (a) front cell and (b) back cell filtered with the front perovskite film.

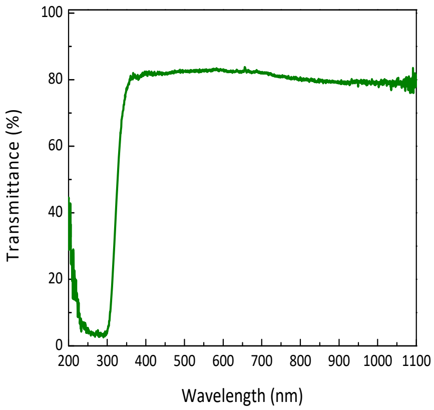

Figure S8. Transmittance spectrum of the glass substrate for the perovskite film used to filter the back cell (see Fig. S7).

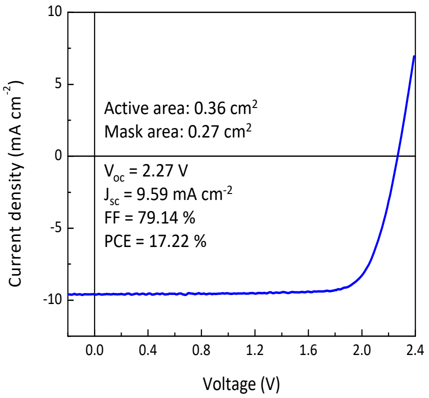

Figure S9. J-V characteristics under 100 mW/cm^2 illumination for a homojunction tandem solar cell with an active area of 0.36 cm2 and a mask area of 0.27 cm^2.

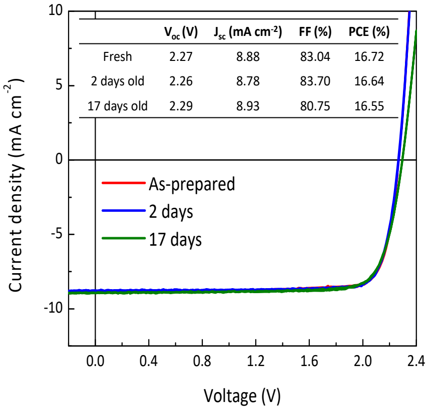

	V_{oc} (V)	J_{sc} (mA cm^{-2})	FF (%)	PCE (%)
Fresh	2.27	8.88	83.04	16.72
2 days old	2.26	8.78	83.70	16.64
17 days old	2.29	8.93	80.75	16.55

Figure S10. J-V characteristics under 100 mW/cm^2 illumination for a homojunction tandem solar cell over time. The device was kept in nitrogen in between measurements.

References

1. M. Niederberger, *Accounts of Chemical Research*, 2007, **40**, 793-800.
2. A. Hadipour, Doped titanate. WO 2017/108710 A1, June 29th 2017.
3. A. R. Forouhi and I. Bloomer, *Physical Review B*, 1986, **34**, 7018-7026.

4. J. Yvon, New Amorphous Dispersion Formula, http://www.horiba.com/fileadmin/uploads/Scientific/Downloads/OpticalSchool_CN/TN/ellipsometer/New_Amorphous_Dispersion_Formula.pdf.
5. M. Anaya, J. P. Correa-Baena, G. Lozano, M. Saliba, P. Anguita, B. Roose, A. Abate, U. Steiner, M. Gratzel, M. E. Calvo, A. Hagfeldt and H. Miguez, *Journal of Materials Chemistry A*, 2016, **4**, 11214-11221.
6. Forouhi-Bloomer alias Amorphous Dispersion Formula, http://www.horiba.com/fileadmin/uploads/Scientific/Downloads/OpticalSchool_CN/TN/ellipsometer/Forouhi-Bloomer_alias_Amorphous_Dispersion_Formula.pdf.
7. S. Babar and J. H. Weaver, *Appl. Opt.*, 2015, **54**, 477-481.
8. J. S. Alberto, A. Miguel, C. M. E., A. C. Mercedes, A. Carlos, G. Elena, M. Noelia, G. Manuel, P. Thomas, E. G. Ramón and M. Hernán, *Advanced Optical Materials*, 2017, **5**, 1600833.